Ultrafast electron dynamics in Mott materials

Gabriel Lantz

UNIVERSITÉ PARIS SUD

Comprendre le monde, construire l'avenir®

LPS ORSAY

Université Paris-Sud

Ecole Doctorale Physique en Ile de France
Laboratoire de Physique des Solides

Discipline : Physique

Thèse de doctorat

Soutenue le 09/02/2015 par

Gabriel Lantz

Ultrafast electron dynamics in Mott materials

Directeur de thèse :	Marino Marsi
Co-directeur de thèse :	Davide Boschetto

Composition du jury :

Président du jury :	Marc Gabay
Rapporteurs :	Michael Bauer
	Eric Beaurepaire
Examinateurs :	Laurent Cario
	Marcelo Rozenberg
	Daniele Fausti

Acknowledgments

I would first like to thank my adviser Marino Marsi, who took me in knowing that I knew little about condensed matter physics. He really taught me how to get to the bottom of things and never give up. I would also like to thank my co-adviser Davide Boschetto who made me discover solid state physics in 2008 and helped me develop my love for science. Without him I would never have discovered this fascinating world. I also acknowledge my jury who spent time reading and discussing my thesis. The discussion during my defense were interesting and pleasant. The FemtoARPES group was a great help to me, it includes Evangelos Papalazarou, Luca Perfetti, Julien Mauchain, Christian Piovera, and Mahdi Hajlaoui. I thank my group at LPS, Nicolas Moisan, Antonio Tejeda, Vincent Jacques, David Le Bolloc'h. Veronique Brouet for her help with ARPES. I am also grateful to the STEM group, especially Laura Bochet who helped me prepare samples. At Synchrotron Soleil, I would like to thank Claire Laulhé, Sylvain Ravy, Jean-Pascal Rueff, François Bertran, Patrick Le Fevre, Julien Rault, and Amina Taleb-Ibrahimi. David Santos-Cottin , Yannick Klein, Andrea Gauzzi, and Michele Casula were part of a fruitful collaboration. I acknowledge the collaboration with Radboud University Nijmegen, Alexey Kimel, Rostislav Mikhaylovskiy, Thomas Huisman. The help from Ernie Glover and Mark Hertlein during the ALS experiment. I also thank Fabio Novelli and Daniele Fausti to have given me a warm welcome when I came to Trieste and to have shown me all the possibility available using pump-probe experiments. I would also like to acknowledge the theoretical help from Michele Fabrizio and Daniel Grieger.

I would like to thank my family for their support and interest in my research. My friends were always there to help me relax during periods of stress. I thank Jean-Christophe Orain and Jon Gorchon for all the lunches and coffee breaks. I would like to finish by thanking Marina who stood by me during my dissertation writing and was always there for me.

Contents

Acknowledgments **3**

Introduction **1**

1 Physics of Mott materials **5**
1.1 The Mott transition 5
1.1.1 Metal to insulator transitions 5
1.1.2 The Hubbard Model 7
1.1.3 Theoretical methods 8
1.2 V_20_3 : a Mott-Hubbard prototype 10
1.2.1 Crystal structure 13
1.2.2 Electronic structure 15
1.3 $BaCo_{1-x}Ni_xS_2$: a moderately ionic Mott insulator 17
1.3.1 Crystal Structure 17
1.3.2 Electronic Structure 19

2 Physics of ultrafast phenomena **25**
2.1 Introduction 25
2.2 Ultrafast experiments 26
2.2.1 Light matter interaction 26
2.2.2 Non correlated materials 31
2.2.3 Correlated materials 34
2.3 Out-of-equilibrium theoretical models 42
2.3.1 Steady state approach 42
2.3.2 Full dynamical approach 43

3 Experimental methods **49**
3.1 Introduction 49

3.2 Time-resolved optical spectroscopy 50
3.2.1 Single color reflectivity 51
3.2.2 White light reflectivity 54
3.2.3 THz spectroscopy 56
3.3 Time-resolved X-ray diffraction 59
3.3.1 X-ray diffraction 59
3.3.2 Synchrotron radiation 62
3.3.3 Time-resolved X-ray diffraction 63
3.4 Angle resolved photoelectron spectroscopy 65
3.4.1 Fundamental principle 66
3.4.2 Photoemission intensity 68
3.4.3 Probing depth 70
3.5 Time-resolved ARPES 71
3.5.1 Fundamental principle 71
3.5.2 FemtoARPES setup 72

4 Tracking the Lattice **75**
4.1 Time-resolved optical reflectivity study of V_2O_3 75
4.2 Time-resolved X-ray diffraction study of V_2O_3 78

5 Tracking the electrons **87**
5.1 Time-resolved THz spectroscopy study of V_2O_3 87
5.2 Time-resolved ARPES study of V_2O_3 92
5.3 Time-resolved ARPES study of $BaCo_{1-x}Ni_xS_2$ 104

6 Discussion **109**

Conclusions and outlook **115**

Bibliography **118**

List of Figures

1.1 Band structure of a metal, semiconductor, and insulator. The gap of the metal is 0, for the semiconductor less than 3 eV and for the insulator more than 3 eV. 6
1.2 Band structure of a Mott insulator. The gap is created because of the Coulomb repulsion U. 6
1.3 Different paths to cross the Mott transition (from [90]) 7
1.4 Density of states for different U/W values in the case of the Hubbard model at half filling (from [105]) 9
1.5 Phase diagram of the Metal-Insulator transition computed using a) DMFT, here D is equivalent to the bandwidth W (from [164]) and b) Gutzwiller approximation (from [198]) 11
1.6 a) Phase diagram of V_2O_3, three phases are present PM, PI, and AFI b) resistivity measurements, the abrupt changes are the phase transitions (from [120]) 12
1.7 a) Crystal lattice unit cell in the hexagonal representation, b) usual numbering of the atoms (from [167]) 13
1.8 Temperature evolution of the lattice parameters through the Mott transition. The variation of c/a during the phase transition show the complex interplay between the lattice and the electronic structure. 14
1.9 a) a_{1g} and e_g^π orbital representations (from [167]), b) V_2O_3 electronic structure, each vanadium atom brings 2 electrons to the bond, that lye in the e_g^π and a_{1g} orbitals. 15
1.10 Photemission spectra for a) V_2O_3 with temperature dependence, the QP peak increases with decreasing temperature b) $(V_{0.972}Cr_{0.028})_2O_3$ with LDA+DMFT calculations, in the PI phase the a_{1g} orbital is almost empty (from [150]) 16
1.11 Phase diagram of $BaCo_{1-x}Ni_xS_2$, three phases are present: PI, PM, and AFI. 18

1.12 a) Unit cell of $BaNiS_2$ b)First Brillouin zone 18
1.13 Band dispersion in $BaNiS_2$ measured by ARPES along ΓM (ZA) and ΓX (ZR) direction for p polarization (a), (b) and s polarizations (c), (d) 20
1.14 Band structure calculations for $BaNiS_2$ using DFT+U (U=3 eV). . 21
1.15 K_z dispersion along ΓM direction for $BaNiS_2$, at E_F and at E-E_F= -150 meV. No dispersion is seen therefore the material is mostly 2D. 21
1.16 Fermi surface for $BaNiS_2$ and isoenergy surface at E-E_F=-0.7 eV for $BaCoS_2$ 22
1.17 Band dispersion in $BaCoS_2$ measured by ARPES along ΓM and ΓX. The band structure shows reminiscence of the metallic compound dispersion but the bands are shifted to lower energies and are broader due to correlation effects. 23

2.1 a)Direct interband transition b) Indirect interband transition c) Intraband transition 28
2.2 Characteristic timescales for relaxation processes 30
2.3 a)$\Delta R/R$ for gold (from [186]), b) Effective temperature for the electrons and the lattice after a short laser pulse excitation. 32
2.4 Build-up of Coulomb screening and plasmon scattering. a) and b) are the imaginary and real part of the inverse dielectric function of GaAs. A Drude peak appears which implies that the material has become a metal after 175 fs, which is the time needed for the Coulomb screening to build-up (from [89]) 34
2.5 $\Delta R/R$ for V_2O_3, the first peak is a purely electronic excitation and the oscillation are coherent phonons (from [115]) 35
2.6 a) 1T-TaS_2 Time-resolved photoemission spectra for a delay of 100 fs, 550 fs and -200 fs. b) Spectral function calculated with DMFT for electrons heated at 1320 K, 1100 K, and 60 K (from [146]) . . . 37
2.7 Schematic view of a photoinduced phase transition in VO_2. S_L and S_e are the lattice and the electronic state. The two paths 1 and 2 represent respectively the scenario where the electrons trigger the phase transition or the lattice. 39
2.8 a) Fermi surface of optimally doped $Bi_2Sr_2Y_{0.08}Ca_{0.92}Cu_2O_{8+\delta}$ at 100 K (T>T_c), N is referred to as the nodal region and AN as the antinodal region b) Time-resolved reflectivity and time-resolved ARPES intensity taken at the different points in a) (from [43]) . . 40

2.9 a-d) Time-resolved ARPES spectra differences between positive and negative time delay; e-h) maxima of the momentum distribution curve extracted from a-d in red, the black line is before excitation. There is a clear renormalization of the elecron mass and a shift of Fermi wave vector, which indicate a similar behavior than a hole doping (from [152]). 41
2.10 a) Calculated variation of the orbital occupancy in V_2O_3 for the a_{1g} and the e_g orbitals versus relative ratio c/a; b) calculated phonon frequency versus relative ratio c/a. These results show that a lattice modification has an effect on the orbital occupancy. (from [117]) . 43
2.11 a) Double occupation versus time after a quenching from U=0 to U calculated with nonequilibrium DMFT (from [53])b) Average double occupation in the metastable state after a U quenching calculated using time dependent Gutzwiller approximation. The blue curve is starting with U=0 and the black starting at U=0.5 (from [173]). Both calculations show the apparition of a metastable state that depends on the initial conditions. 45
2.12 Photoemission spectra calculated using nonequilibrium DMFT, red is more intensity and white is less. a-c) Upper Hubbard band evolution after an electric pulse excitation for different electron-phonon coupling g, the pulse is taken as shown in inset of a). d) Lower and upper Hubbard band for the metastable state arising from a DC electric field. (from [202]) 46

3.1 Pump-probe scheme. The pump excites the material and the probe observes the material after a controllable delay. 50
3.2 Scheme of the different pumps and probes used in this work. The pump is always a 1.5 eV laser pulse. The probes are optical reflectivity, THz spectroscopy, X-ray diffraction, and photoemission spectroscopy. 51
3.3 Typical time-resolved reflectivity trace(from [116]) 52
3.4 Time-resolved single color reflectivity experimental setup 53
3.5 a) Density Of States (DOS) for a correlated metal and a Mott insulator b) Optical conductivity for the DOS from a). The metallic and the insulating state can be clearly identified with their optical conductivity probed by spectroscopic techniques (from [163] 55
3.6 White light setup 56
3.7 Step to calculate the loss function. 57
3.8 THz time domain spectroscopy setup 58
3.9 Vector version of Bragg's law. 60
3.10 Ewald's sphere 61

3.11 a) Synchrotron laboratory b) Synchrotron radiation 63
3.12 a) Diagram of the synchrotron with a synchronized laser system b) Time structure of the synchrotron hybrid filling mode, an isolated electron bunch can be gated using a boxcar c) acquisition scheme, one out of two X-ray pulse is pumped in order to have an unpumped reference. 64
3.13 a) Geometry of the emission of the photoelectron. b) representation of the photoelectron detector (from [46]) 66
3.14 Conservation laws for the photoelectron process (from [46]). 67
3.15 Polarization dependence of ARPES intensity. The mirror plane contains the surface's normal, the incident beam, and the emitted electron. The polarization s and p are respectively in plane and out of plane (from [46]). 69
3.16 Mean Free Path of excited electrons in solids versus their kinetic energy (from [177]). 70
3.17 Experimental chamber of the FemtoARPES setup. 73
3.18 FemtoARPES laser setup to produce the fourth harmonic 73

4.1 A_{1g} optical phonon mode (from [117]) 76
4.2 Time-resolved reflectivity in the PI phase. The oscillation represent the coherent optical phonon (from [117]) 76
4.3 Coherent A_{1g} optical phonon frequency for different fluences, dopings, and crystal directions. The photoinduced frequencies are all blue shifted compared to Raman frequency. (from [117]) 77
4.4 Time-resolved X-ray diffraction geometry. The X-rays are grazing to match the penetration depth of the laser. 78
4.5 Position of the Bragg peak on the 2D detector with and without the pump laser. The shift of the Bragg reflection corresponds to a dilatation of the lattice parameters because of a heat increase of 50 K due to laser heat accumulation. 79
4.6 Kϕ Rocking curve wih and without pump laser. The laser heat accumulation makes the the crystal turn, which related to a peak shift. 80
4.7 Kω rocking curve of the (113) Bragg reflection for various delays and incidence angles. The difference at 60 ps is asymmetric whereas at 2 ns is symmetric. 81
4.8 Kω rocking curve differences for the (113) Bragg reflection versus delay. Red is positive and blue is negative. 82

4.9 Integral of the peak and center of mass of the peak in Kω for different incidence angles and Bragg reflection. The increase in intensity during the first 300 ps is not compatible with heat nor with a modification of the structure factor. At 2 ns, the change is equivalent to an increase of temperature of 30 K. 84
4.10 Delay of the maximum intensity change versus penetration depth. The speed of the deformation is the same as the speed of sound in the material. 85
4.11 Intensity of Bragg (113), (116), and (024) versus relative Wyckoff position. 85

5.1 The loss function derived from THz transmission spectroscopy for $(V_{1-x}Cr_x)_2O_3$ (x=0.011) at 300 K (PI phase) and 200 K (PM phase) and for $(V_{1-x}Cr_x)_2O_3$ (x=0.028) at 200 K (PI phase). Positions of the different measurements points on the phase diagram. The flat loss function is a good signature of the gap since there are no resonances in this THz range. The loss function is low in the PI phase because the THz pulse is well transmitted and high in the metallic phase. 88
5.2 The equilibrium THz transmission in the hysteresis cycle of $(V_{1-x}Cr_x)_2O_3$ (x=0.011), red being the heating and blue the cooling. 89
5.3 Negative time delay transmission of $(V_{1-x}Cr_x)_2O_3$ (x=0.011) with a pump laser. The black triangles show the initial transmission before pumping the sample. The green circles are the transmission at negative delays. The arrows indicate the effect of the optical pump. The phase transition is triggered by the accumulation of heat of the 1 kHz pump pulse. The fluence threshold is linear with the distance from the starting point to the heated line of the phase transition. 91
5.4 Time-resolved variation of the transmission in $(V_{1-x}Cr_x)_2O_3$ (x=0.011) at 300 K (PI phase). The negative sign means that there are more free carriers due to heat or a metallization. The first relaxation time could be related to the phonon hardening seen with optical reflectivity. 92
5.5 Phase diagram of V_2O_3. The different markers represent where the measurements were done. 93
5.6 Photoemission spectra for different dopings in the PI and PM phase. The dashed lines represent en estimation of the gap. PI phase spectra have clear gaps whereas the PM spectra have some weight near the Fermi level. 94

5.7 Photoemission spectra for different temperature in the PI and PM phase. The black curve is the difference between the high temperature and the low temperature. In the PI phase, there is a filling of the gap with temperature and in the PM phase the QP increases with lowering temperature. 95

5.8 Photoemission spectra for different delays in the PI and PM phase. In the PI phase some spectral weight can be seen in the gap at 50 fs. The QP melts in the PM phase. 95

5.9 Photoemission spectra differences versus delay in the PI phase. The arrows represent the center of mass of the spectrum. In-gap states appear that are different from an equilibrium temperature increase. 97

5.10 Photoemission spectra differences for 2.8% Cr and 5.6% Cr doped at 200 K. The comparison with an equilibrium heated difference show that for both the 2.8% Cr and the 5.6% Cr non thermal in-gap states appear around -0.1 eV. 98

5.11 Photoemission spectra differences versus delay in the PM phase. The dynamics are the same as in the PI phase. The QP melts faster than the time resolution. The hot electrons thermalize in 200 fs. 98

5.12 Photoemission spectra differences for different dopings in the PI phase for a delay of 50 fs and 400 fs. The photoinduced difference are very similar to the difference during the phase transition for the 1.1% Cr doping. 99

5.13 Photoemission spectra differences for different dopings in the PM phase for a delay of 50 fs and 400 fs. The hot electron differences are very similar for all doping and temperature but the loss of QP is different, which can be explained by the fact that the QP is different for all the different temperature and doping. 100

5.14 Fluence dependence of the photoemission spectrum difference for 50 fs and 400 fs delay. The differences are perfectly linear with fluence in the PI phase. 101

5.15 Fluence dependence of the integrated photoemission difference in the PI and PM phase. The intensity was integrated in the estimated gap in the PI phase and above the Fermi level for the PM phase. All the fluence dependences of the hot electrons are linear with fluence. 101

5.16 Fluence dependence of the integrated photoemission difference under the Fermi level for the PM phase. The effect on the QP is not linear with fluence at 200 K. 102

5.17 Photoemission spectra differences for different delays for a 2.8% Cr doped sample. Time scan integrated near -0.1 eV. The two relaxation times correspond respectively to the relaxation of the hot electrons and to the relaxation of the non-thermal state. 103
5.18 Photoemission spectra differences for different delays for a 5.6% Cr doped sample. Time scan integrated near -0.1 eV. The two relaxation are similar to the 2.8% Cr doped sample 103
5.19 Equilibrium ARPES measurements on $BaNiS_2$ using the 6 eV laser pulse near the Γ point. Time-resolved ARPES measurements, blue meaning less electrons and red more electrons. The regions of interest are taken on either side of the Fermi energy: V1 is the intensity under the Fermi energy and C1 is the one above. 105
5.20 Time evolution for the electrons on either side of the Fermi level. Both dynamics are similar and are typical of a heated metal, first heated and then cooled down. 105
5.21 Photoemission spectra near Γ for $BaCoS_2$ using laser and synchrotron. Spectra for different delay times. The laser spectra are similar to the Synchrotron spectra. The photoexcited spectra show in-gap states. 106
5.22 Time-resolved ARPES measurements on $BaCoS_2$. The spectra differences at 50 fs and 500 fs show in-gap states different from an equilibrium temperature increase. The time scans show that the dynamics are fast above the Fermi level and much lower under. . . . 107

6.1 Experimental observations in V_2O_3 using different pump-probe techniques. 110
6.2 Scheme of the proposed mechanisms happening after a photoexcitation. The pump laser excites electrons from the e_g orbitals to the bonding a_{1g} orbital. At short time delay the filling of the orbitals changes inducing a closure of the gap. On longer timescales, the electrons in the bonding a_{1g} orbital induce a phonon hardening that increases the bandwidth of the system, thus inducing a non-thermal state. 112

Introduction

Condensed matter physics consists in the study of matter in its solid form. When atoms are arranged in ordered patterns, new physical properties arise for phenomena such as electric conductivity, or magnetism. Theoretical models using statistical and quantum mechanics as well as electromagnetism are able to account for these emerging properties, which are very diverse. When increasing the interactions among the electrons, atoms, and spins, the emerging properties become even more exotic. Numerous phases arise such as superconductivity, charge density waves, multiferroics, and Metal-to-Insulator transitions. These emerging properties have extensively been studied near equilibrium, but what happens when the material is strongly excited and is far from equilibrium? This highly excited material evolves in time with characteristic timescales, related to the different interactions among the various degrees of freedom. In order to view this time evolution of the excited material, the observation has to be faster than these characteristic timescales, which is in the order of tens of femtoseconds for the electron-lattice interaction. Therefore observing materials faster than the time needed to reach thermodynamic equilibrium can lead to the discovery of new out-of-equilibrium phases, which emerge from pure particle interactions.

The exotic phases at equilibrium occur in a class of materials called strongly correlated materials, which are materials that can not be described with non interacting particles. One of the most striking consequences of these interactions are Metal-to-Insulator transitions, especially the Mott transition where each electron localizes alone on an atomic site because of on site Coulomb repulsion. This Mott insulating phase is a corner stone for strongly correlated materials and is present in many materials including high temperature superconductors. Although this transition is viewed as purely electronic, the interaction between the lattice and the electrons is still an open question. The electron-phonon coupling is a fairly hard value to estimate with standard near equilibrium experiments and is crucial for the superconductivity theory. In this thesis, I performed ultrafast time-

resolved experiments that observe the different degrees of freedom faster than their relaxation time between each other. The materials are highly excited and in an out-of-equilibrium state. They are then observed on an ultrafast timescale. These ultrafast experiments have been for the last 30 years a very successful way to estimate the electron-phonon coupling. Femtosecond laser pulse excites the electrons, which are decoupled from the lattice for a few tens of femtoseconds. The relaxation rate provides a way to estimate experimentally the electron-phonon coupling. The coupling between different degrees of freedom can also be disentangled since the electrons, phonons, and spins have different characteristic timescales.

Originally photoexcitation of materials was done to study the relaxation channels to recover the initial state. More recently, it has been demonstrated that light can act as an equivalent thermodynamic variable. The laser pulse can photodope or act as an intense field that transforms the material. The photons act as an ultrafast control parameter for the properties of the material, laying the path for ultrafast electronic devices such as switches. Different phase transitions have been observed with intense laser pulses but the driving force has not yet been clearly identified. The question is: are the electrons or the lattice responsible for the phase transition?

In order to try to answer these questions, I have studied a very well known material, V_2O_3, which is a Mott-Hubbard insulator prototype. It has been extensively studied near equilibrium and existing theories can explain most of its properties. To disentangle the effects of temperature, the phase specificity, and the universal behavior, the whole phase diagram was explored in out-of-equilibrium conditions. The time-resolved experimental techniques used to probe the material were optical reflectivity, X-ray diffraction, THz spectroscopy, and Angle Resolved Photoelectron Spectroscopy (ARPES). Although none of these experimental techniques are newly developed, the use of many different probes to study a same phenomenon in out-of-equilibrium is rarely done. Comparing the different results is crucial since X-ray diffraction views mostly the lattice while ARPES observes mostly the electrons. The electron-lattice interplay could therefore be precisely mapped. Another Mott insulator, $BaCo_{1-x}Ni_xS_2$, has also been studied with time-resolved ARPES in this thesis in order to identify the general trends of out-of-equilibrium Mott insulators.

This thesis is separated into 6 chapters, the first three introduce general concepts about the physics of the material and the experimental methods used. The last three present the results obtained on V_2O_3 and $BaCo_{1-x}Ni_xS_2$ during the course of my Ph.D.

The first chapter introduces the equilibrium view of Mott insulators, starting with the Mott transition and then presenting the properties of the materials V_2O_3 and $BaCo_{1-x}Ni_xS_2$. The second chapter evokes the prior work done in out-of-

equilibrium physics, looking at the experimental and theoretical progresses done in the recent years. No presentation of ultrafast phenomenon in magnetic materials will be presented since magnetic effects have not been explored in this thesis. In the next chapter the time-resolved experimental methods are presented. The experimental results are shown in two separate chapters: the former looks at the lattice evolution after photoexcitation using optical reflectivity and X-ray diffraction; the latter shows the electronic behavior using THz spectroscopy and ARPES. The last chapter summarizes all the experimental results and compares the lattice and electronic evolution. Finally, I will summarize the main findings and look at the perspectives they open.

Chapter 1

Physics of Mott materials

1.1 The Mott transition

One of the fundamental properties of solids is the electric resistivity, which is as high as 10^{22} Ω/cm for good insulators and as low as 10^{-10} Ω/cm for metals or even 0 Ω/cm for superconductors. The total range is one of the largest ones for an everyday physical property. It is fairly easy to measure experimentally but much harder to predict theoretically. A first approximation is to neglect the interaction among electrons: this approximation is the free electron model, which describes electronic crystal structures in terms of electronic bands. These bands can be constructed using Bloch wave functions introduced by Felix Bloch in 1928 [19]. Felix Bloch received the Nobel prize in 1952. Looking at the occupancy of the electronic band, one can determine if the material is going to be metallic or insulating [102]. The last occupied band is called the valence band and the first empty one is the conduction band. Fig.1.1 shows the different cases: if the valence and the conduction bands overlap, the material will be metallic; on the contrary if there is a gap between them the system will be insulating. Insulators with a gap smaller than 3 eV are commonly called semiconductors. The free electron model was very successful but failed in certain cases to predict the correct properties.

1.1.1 Metal to insulator transitions

In 1937, De Boer and Verwey pointed out that the transition metal oxides with partially filled 3d and 4d orbitals had a very low electronic conductivity and they suggested that the free electron model could not explain their properties [48]. These observations led N.F. Mott to introduce an electrostatic interaction between electrons in order to understand these compounds [135, 132]. The Coulomb repulsion introduced can explain the discrepancy between experiments and the free

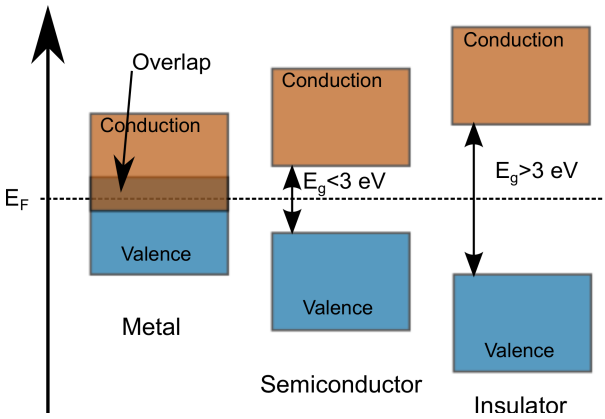

Fig. 1.1: Band structure of a metal, semiconductor, and insulator. The gap of the metal is 0, for the semiconductor less than 3 eV and for the insulator more than 3 eV.

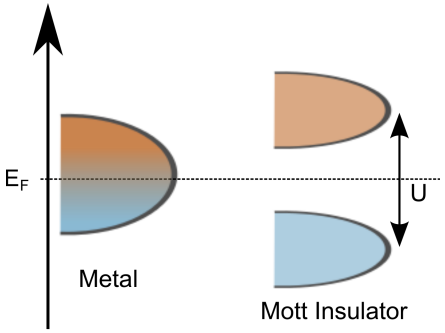

Fig. 1.2: Band structure of a Mott insulator. The gap is created because of the Coulomb repulsion U.

electron model predictions. In a Mott insulator, the majority of the electrons are localized near the atoms and the moving electrons find the atoms occupied therefore the conductivity is significantly lowered. This can be viewed as a competition between the kinetic energy of the electrons and the Coulomb repulsion. If the Coulomb repulsion is higher, the material becomes insulator. Fig.1.2 shows the splitting of the bands because of Coulomb repulsion resulting in a full lower band and a empty upper band called lower and upper Hubbard band.

Since the competition is between two energies, one can cross the metal-to-insulator transition (MIT) by varying the kinetic energy or the Coulomb repulsion. Numerous transition metal oxides exhibit this kind of transition, for example titanium oxides, vanadium oxides, or even the copper oxides [130, 133, 90]. Fig.1.3 shows the two ways to cross the transition either by changing the filling (FC-MIT), which changes the number of occupied sites hence the Coulomb repulsion, or by

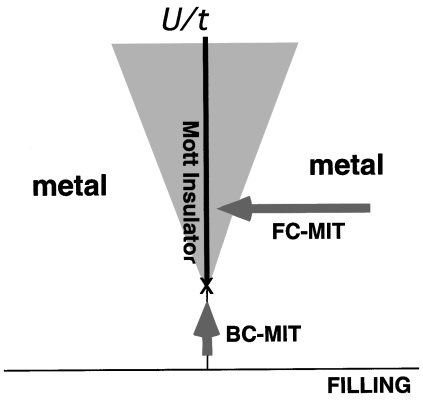

Fig. 1.3: Different paths to cross the Mott transition (from [90])

varying the bandwidth (BC-MIT), which changes the kinetic energy. Since the number of free carriers is discontinuous through the transition, it is therefore a first order transition without any symmetry breaking. This leads to a latent heat and phase coexistence near the transition [151].

Correlated materials refer to all the systems where the interactions between different degrees of freedom have to be taken into account to reflect their properties. These interactions lead to interesting phases such as superconductivity, charge density waves, and Mott insulators. The orbitals involved in these compounds are usually d and f orbitals. The d electrons have a small radius of the wave function compared to the crystal lattice parameter. Therefore the smaller overlap of the orbitals decreases the bandwidth and diminishes the kinetic energy. The ligands with p orbitals help increase the cohesive energy for the formation of the solid. Their overlap with the d orbitals creates the transfer between the different d orbitals. This overlap can increase or diminish the energies of the different d and p orbitals. When the band gap is between two d orbitals the material is viewed as a Mott insulator, like V_2O_3. If the band gap is between p and d orbitals the material is a charge transfer insulator [212], such as NiS_2 [67]. The overlap between the d orbitals is extremely sensitive to the crystal field that can induce MITs [90]. We will see that the crystal field is essential for the MIT in V_2O_3 but we will first discuss the theoretical models to describe general Mott insulators.

1.1.2 The Hubbard Model

The most widely used model to represent the interaction among particles in solids was developed by Hubbard in 1963 [88]. The Hamiltonian consists of two terms, one is the kinetic energy defined by the hopping t and the other is the

Coulomb repulsion U. The tight binding Hamiltonian for a single band is :

$$H_{Hub} = -t \sum_{<i,j>,\sigma} (c^{\dagger}_{i,\sigma} c_{j,\sigma} + c^{\dagger}_{j,\sigma} c_{i,\sigma}) + U \sum_{i=1}^{N} n_{i\uparrow} n_{i\downarrow} \tag{1.1}$$

where $< i, j >$ is the nearest neighbor interaction, $n_{i\sigma}$ is the number of electrons at site i and with spin σ. This model corresponds to the free electron model if $U = 0$ which is metallic, and if $U \to \infty$ and band is half filled, it renders the atomic limit. This simple model is able to predict many properties and especially Mott insulators. The main defect of the Hubbard model is the lack of long range order, that can be added using the extend Hubbard model, which considers the interaction with neighbors. The other problem is the lack of coupling to the lattice which is added in the Hubbard-Holstein model [86, 50].

Although simple, solving the problem with the Hubbard Hamiltonian can be challenging. For small U/t or t/U, one can use perturbation approximations and solve the problem with Hartree-Fock methods. But for intermediate interactions, the Hubbard model can not be solved analytically and numerical method have to be used. Dynamical Mean Field Theory (DMFT) [70, 71, 105] is a well know method to solve the Hubbard model. Another approach is being investigated, which is the Gutzwiller approximation [77, 198, 168], that is numerically cheaper. I will briefly examine these two approaches in the next section.

1.1.3 Theoretical methods

DMFT provides an excellent description of Mott compounds. Standard mean field theory maps a many body problem onto a single site problem. The average effect of the environment should be the average effect of the single site problem, where the average effect is taken self consistently. DMFT does the same: it maps the Hubbard Hamiltonian onto a single site problem which is the Anderson Impurity model [70]:

$$H_{AIM} = \underbrace{U n_{\uparrow} n_{\downarrow} - \mu(n_{\uparrow} + n_{\downarrow})}_{H_{atom}} + \underbrace{\sum_{i} \epsilon_i a^{\dagger}_{i\sigma} a_{i\sigma}}_{H_{bath}} + \underbrace{\sum_{i\sigma} (V^{\sigma}_{i} c^{\dagger}_{\sigma} a_{i\sigma} + h.c)}_{H_{mix}} \tag{1.2}$$

where H_{atom} is the atomic Hamiltonian containing the on site Coulomb repulsion U, H_{bath} is the electron bath with energies ϵ_i, V^{σ}_{i} the hybridization between the atom and the bath electrons. ϵ_i and V^{σ}_{i} have to fulfill the self-consistency conditions. The Anderson impurity model is the interaction between a single site and a bath of electrons. The atom has its own energies where the double occupancy costs U, and the bath has energy levels ϵ_i. They interact through H_{mix} where V^{σ}_{i}

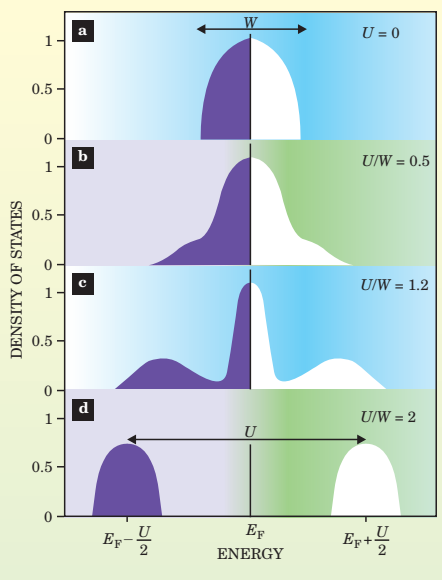

Fig. 1.4: Density of states for different U/W values in the case of the Hubbard model at half filling (from [105])

is the probability that an electron from the bath goes to the single atom. If V_i^σ is large the material is metallic and respectively if it is small the material is insulating. In DMFT, the self-consistency condition varies with time and the hybridization parameters ϵ_i and V_i^σ have to define the same Green's function for the lattice problem and the single site problem. Since the Green function is frequency dependent, the theory is dynamic.

Once the Anderson impurity model is set, one has to solve it. Several ways exist to find the solution and many introduce approximations [71]. The numerical solutions are numerical renormalization group, Quantum Monte Carlo method, and exact diagonalization. The analytic methods rely on perturbation theory. Rozenberg et al. were able to solve the Hubbard model for half filling using DMFT [166, 165]. Fig.1.4 shows the density of state for different U/W values. At $U/W = 0$ the system is metallic. For $U/W = 1.2$ a quasiparticle peak appears near the Fermi energy. The quasiparticle peak is a narrow band that lies near the Fermi level and which is the coherent part of the spectrum. The rest of the spectral weight is transferred to lower and higher energies forming the Lower and Upper Hubbard band (LHB and UHB). When $U/W = 2$ the entire spectral weight is in the LHB, and UHB is empty, the system is insulating. The qualitative agreement with experiments on Mott insulators is a great success of DMFT.

Nevertheless, the main approximation in DMFT is supposing that each atomic site has infinite coordination [124]. Therefore it neglects spatial fluctuation and

is not able to predict the surface effects in V_2O_3 [21, 157]. The other successful theoretical approach is done by Gutzwiller approximation.

The Gutzwiller approximation was developed by Gutzwiller in the sixties [78, 77] and first applied to the Hubbard problem in 1970 by Brinkman and Rice [30]. Gutzwiller constructs a test wave function using the uncorrelated ground state $|\psi_0\rangle$ and minimizes the number of double occupied sites. The test wave function is [193]:

$$|\psi\rangle = \prod_i [1 - (1-g)n_{i\uparrow}n_{i\downarrow}]|\psi_0\rangle = g^D|\psi_0\rangle \tag{1.3}$$

where $n_{i\uparrow}n_{i\downarrow}$ is the double occupancy of site i, g is the variational parameter, and D is the average number of double occupied sites. If $g = 1$ the wave function is the non interacting state and if $g = 0$ $|\psi\rangle \neq 0$ only if $D = 0$, thus one electron per site. The parameter g is given by minimizing the ground state energy :

$$E = \frac{\langle\psi|H_{Hub}|\psi\rangle}{\langle\psi|\psi\rangle} \tag{1.4}$$

This model computes a fairly good approximation for the ground state (T=0 K) but is more complicated for higher temperature. Nevertheless Wang et al. managed to compute the phase diagram for the single band Hubbard model [198]. Fig.1.5 is the theoretical phase diagram computed by DMFT and using the Gutzwiller approximation. The two phase diagrams qualitatively agree. There is a paramagnetic Insulating phase (PI), a paramagnetic metallic phase (PM), a crossover regime, and, in the case of DMFT, there is an antiferromagnetic insulating phase (AFI).

The advantage of DMFT is its good practical use: it is used for many correlated problems. Its limitations are the high computational cost, the lack of spatial resolution, and the limitation to high temperature. Whereas Gutzwiller method has spatial resolution and is less numerically demanding, it is also for now less handy and performs better at low temperature. The single band Hubbard model is very useful to understand the Mott transition but it is still an approximation because most Mott insulators have two bands close to the Fermi level. The extension to a two band model gives better agreement with the experiments [168]. Both theories cited above have their out-of-equilibrium extension that I will present in chapter 2. The material most commonly used to compare experiments and theories is vanadium sesquioxide V_2O_3, which I will present in the next section.

1.2 V_20_3 : a Mott-Hubbard prototype

In 1969, MCWhan et al. were able to grow high quality monocrystal of $(V_{1-x}Cr_x)_2O_3$ and perform resistivity and X-ray diffraction measurements. They observed a first

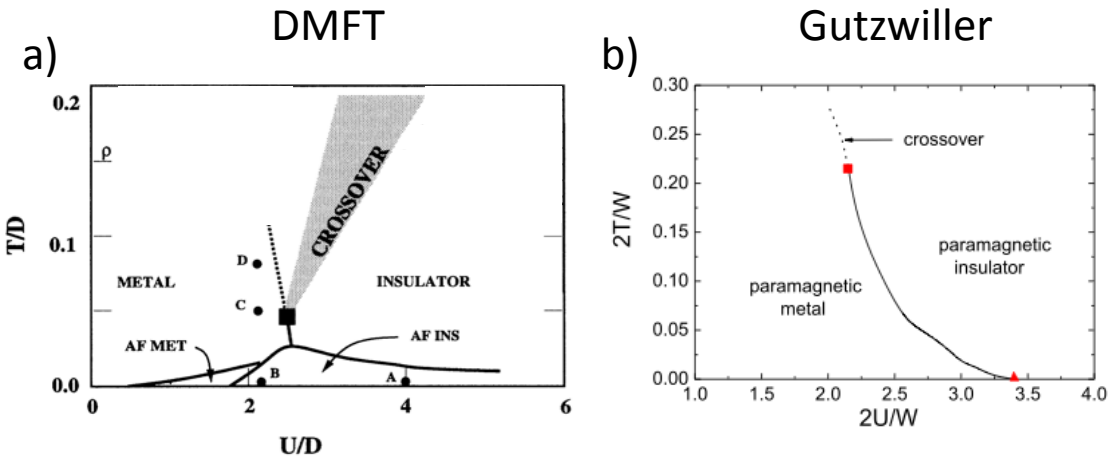

Fig. 1.5: Phase diagram of the Metal-Insulator transition computed using a) DMFT, here D is equivalent to the bandwidth W (from [164]) and b) Gutzwiller approximation (from [198])

order transition at 180 K for the pure compound accompanied with a structural phase change. A second first order transition was also seen at 300 K for the 1% Cr doped compound but this time with no structural symmetry breaking [122]. Fig.1.6 shows the phase diagram they found and the resistivity measurements done. They concluded that the material was a Mott insulator.

The phase diagram is composed of three phases, a paramagnetic metal (PM), a paramagnetic insulator (PI), and an antiferromagnetic insulator (AFI). When doping with Cr, the material crosses from PM to PI for a 1% Cr doping at 300 K: this transition is a true Mott transition since there is no symmetry breaking. It is also crossed by temperature for the 1.1% Cr doping at 220 K. The electrons go from being delocalized to being localized, the resistivity changes by mode than one order of magnitude. Note that the PM is a poor conductor and the PI is a bad insulator. The transition can also be crossed using pressure starting from PI. The transition from PM to AFI has a much sharper change in resistivity; it jumps 6 orders of magnitude. The AFI can be suppressed when doping with Ti: at 0 K the transition happens for 5% Ti doping. A phase mixture between PI and PM phases, called the crossover region, happens above the critical point at around 400 K. This critical point follows the universal properties of a liquid-gas transition [108].

Over 500 papers were published on V_2O_3 and there are still many groups working on the subject. Over the years many theoretical and experimental efforts have been made to understand in detail the behavior of vanadium sesquioxides. Different review papers from the eighties until now can be found [32, 134, 81]. It represents today a perfect test bed for new theoretical models and new experi-

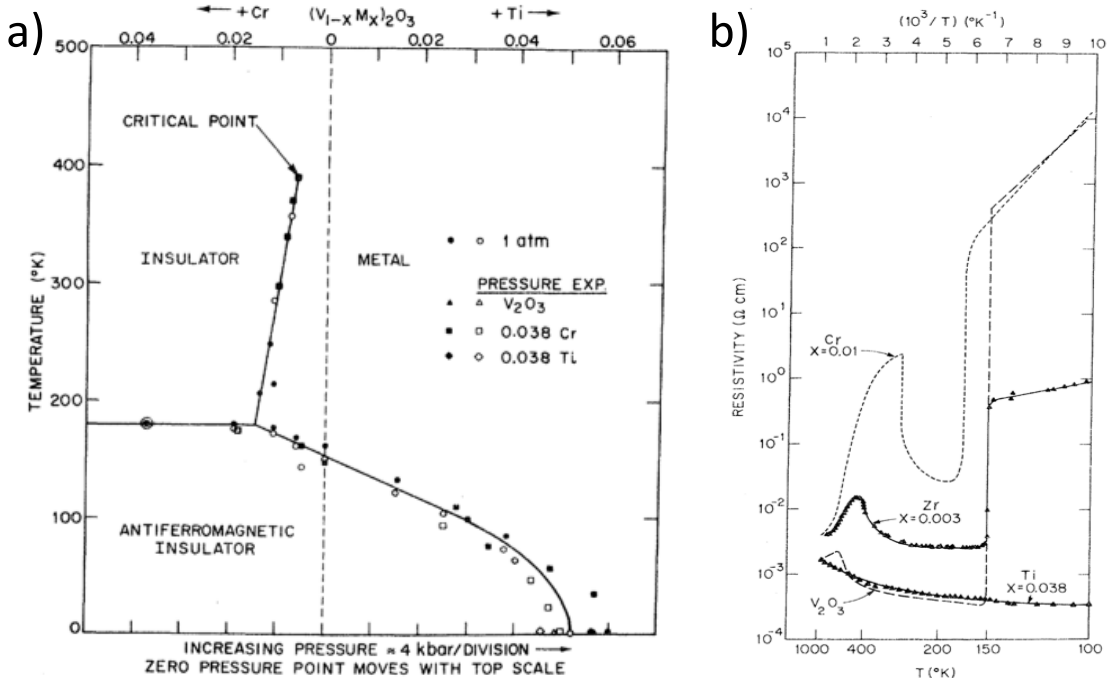

Fig. 1.6: a) Phase diagram of V_2O_3, three phases are present PM, PI, and AFI b) resistivity measurements, the abrupt changes are the phase transitions (from [120])

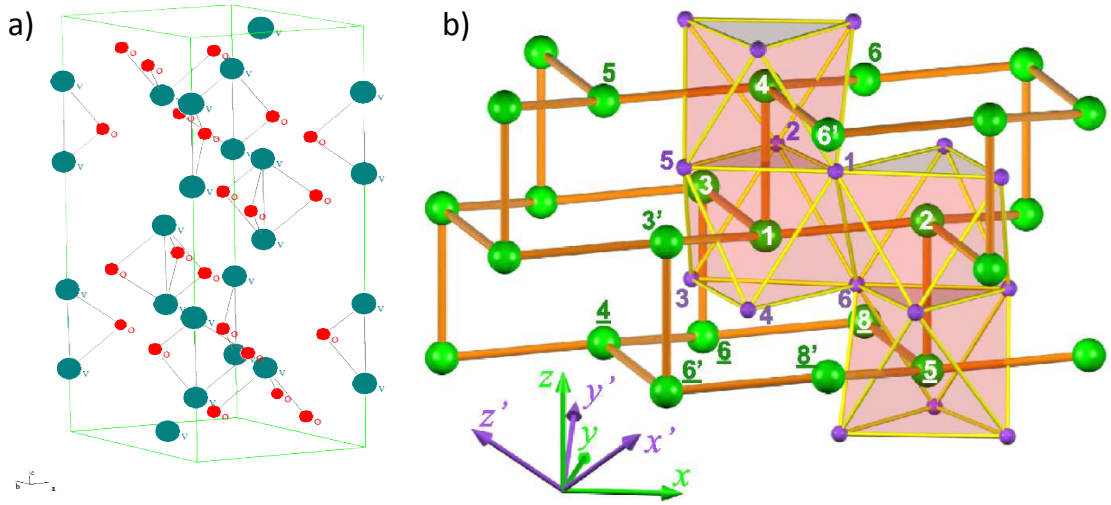

Fig. 1.7: a) Crystal lattice unit cell in the hexagonal representation, b) usual numbering of the atoms (from [167])

mental techniques as I will describe in chapter 4 and 5. I will first present the crystal structure and then the electronic structure as it is understood today.

1.2.1 Crystal structure

The crystal structure from the different phases were resolved in the seventies [122, 51, 121, 120]. In the PI and PM phase the material has a corundum crystal structure with a rhombohedral unit cell. However the usual unit cell taken is the hexagonal unit cell which contains 18 oxygen atoms and 12 vanadium atoms. The symmetry space group is $R\bar{3}c$ (group number 167). Fig.1.7 a) shows the hexagonal unit cell and b) shows the usual numbering of the atoms that I will use in this thesis. The structure can be viewed as the stacking of octahedra with 6 oxygens and a vanadium in the middle. The octahedra create in the ab-plane a honeycomb lattice. The octahedra are imperfect due to a trigonal distortion illustrated in Fig.1.9. This distortion is increased by a tilt of the c axis when crossing from the PM phase to the AFI phase. The AFI phase crystal structure is monoclinic and its symetry group is I2/a (group number 15).

The most crucial distance in order to understand the Mott transition is the vertical V_1-V_4 distance, which is smaller than the basal V_1-V_2 distance. In order to calculate this distance we need the position of the vanadiums inside the unit cell, which are given by the Wyckoff positions. Using the Wyckoff position for the vanadium, this distance is $d(V_1 - V_4) = (2z_V - 0.5)c$. The next table summarizes the different values of lattice parameters, Wyckoff position, and V_1-V_4 distance [42]:

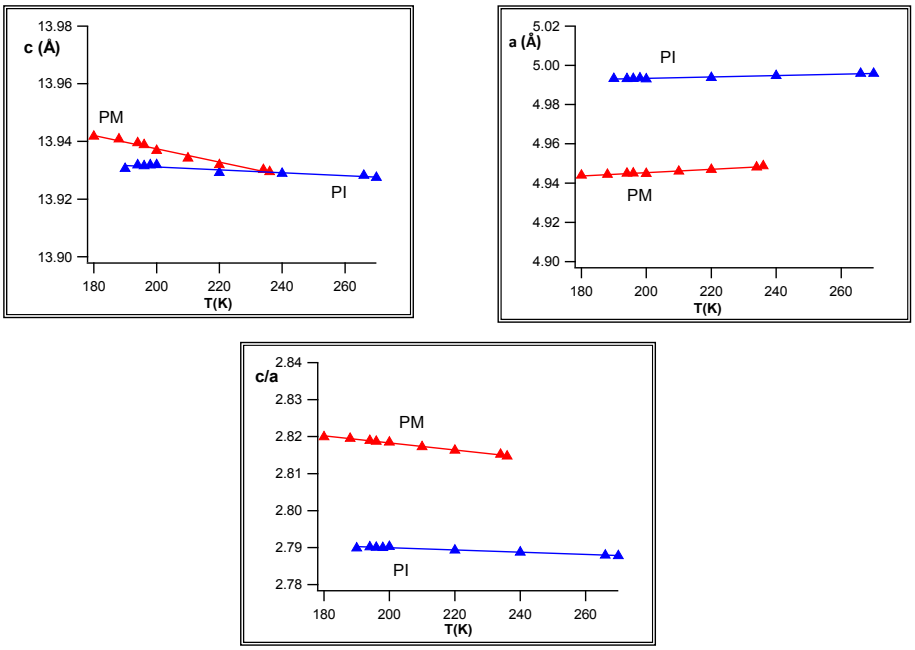

Fig. 1.8: Temperature evolution of the lattice parameters through the Mott transition. The variation of c/a during the phase transition show the complex interplay between the lattice and the electronic structure.

Sample	T (K)	Phase	a (Å)	b (Å)	c (Å)	z_V	V_1-V_4 (Å)
V_2O_3	300 K	PM	4.95	4.95	14.00	0.3463	2.697
V_2O_3	100 K	AFI	7.255	5.00	5.55	/	2.745
$(V_{0.989}Cr_{0.01})_2O_3$	300 K	PI	4.99	4.99	13.93	0.3485	2.744
$(V_{0.989}Cr_{0.01})_2O_3$	200 K	PM	4.94	4.94	13.94	0.3465	2.690
$(V_{0.972}Cr_{0.028})_2O_3$	300 K	PI	4.99	4.99	13.91	0.34867	2.745
$(V_{0.944}Cr_{0.056})_2O_3$	300 K	PI	5.01	5.01	13.89	0.34866	2.74

The more insulating the material gets, the larger the distance V_1-V_4 is. For the 1.1% Cr doping the c lattice parameter increases at the transition from PI to PM as seen in Fig.1.8 but it is compensated by a decrease of the Wyckoff position. Therefore the V_1-V_4 distance contracts. This is the only structural change occurring during the Mott transition which has no symmetry breaking with a small latent heat[99].

Since the Mott transition is a first order transition, there is a large hysteresis and a phase coexistence. Powder diffraction on the 1.1% Cr doping shows that the hysteresis is about 60 K as shown in Fig.1.8. The phase coexistence has also been seen using microscopic photoemission and displays a pinning of the phases

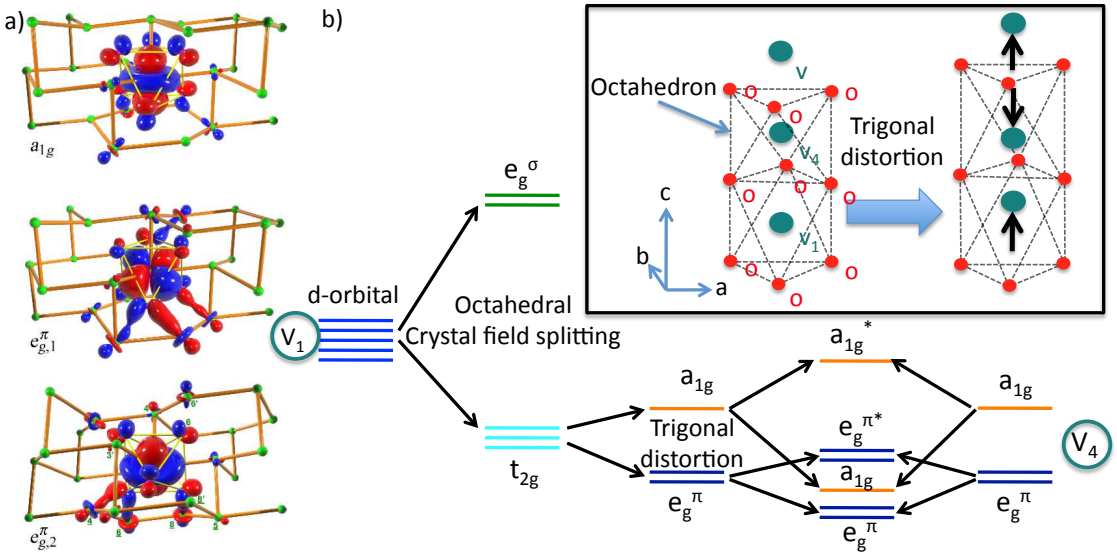

Fig. 1.9: a) a_{1g} and e_g^π orbital representations (from [167]), b) V_2O_3 electronic structure, each vanadium atom brings 2 electrons to the bond, that lye in the e_g^π and a_{1g} orbitals.

on the crystal defects [113, 112]. These properties of the phase transition are very important when trying to photoinduce a phase transition as we will see in chapter 4 and 5.

1.2.2 Electronic structure

Many theoretical approaches have been used to understand the electronic structure of V_2O_3. The vanadium atoms are in a three valent oxidation state therefore each vanadium brings 2 electrons to the V-V bond. Octahedral field splitting yields to the separation of d orbital into a lower t_{2g} band and an upper e_g^σ band. Since the octahedra has a trigonal distortion the t_{2g} are split into a lower doubly degenerate e_g^π and a single bonding a_{1g} state. The hybridization between the two vanadium atoms (V_1-V_4) leads to a strong bonding a_{1g} and an antibonding a_{1g}^* state. The main question concerning the electronic structure is whether the a_{1g} states are lower than the e_g^π states, and the effect of the Coulomb repulsion on the bands.

In 1978, Castellani et al. made an important effort to calculate the band structure. They concluded that the a_{1g} states should be lower than the e_g^π states because of the strong hopping integral of the two a_{1g} orbitals. Therefore one electron is used for the chemical bond between the two vanadium atoms and the other is in the twofold degenerate localized e_g^π orbitals. This vision should lead to a quarter filled

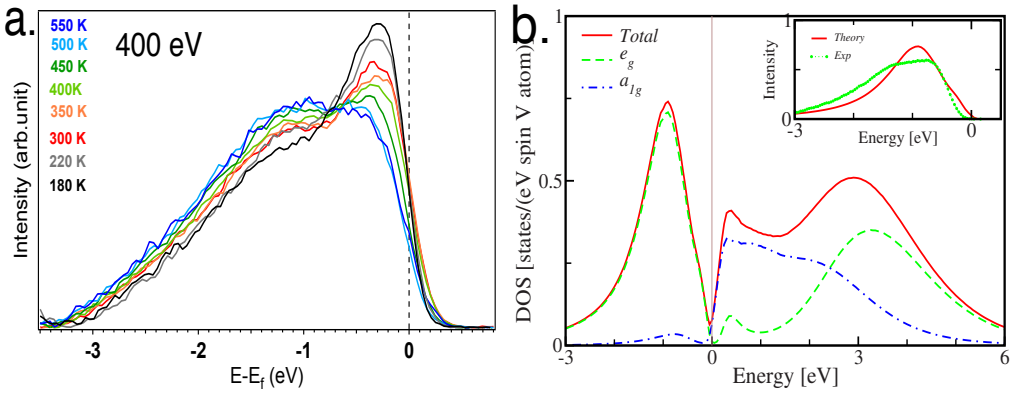

Fig. 1.10: Photemission spectra for a) V_2O_3 with temperature dependence, the QP peak increases with decreasing temperature b) $(V_{0.972}Cr_{0.028})_2O_3$ with LDA+DMFT calculations, in the PI phase the a_{1g} orbital is almost empty (from [150])

spin 1/2 Hubbard model [37, 36, 35]. In 1995, Rozenberg et al. used DMFT and found that this vision was able to capture the metal-to-insulator transition [164]. Nevertheless in 2000, Park et al. used polarized X-ray absorption and found that the vanadium atoms are in a spin one state with the $e_g^\pi e_g^\pi$:$e_g^\pi a_{1g}$ occupation ratio that varies from phase to phase, 2:1 for the AFI, 1:1 for the PM, and 3:2 for the PI [145]. Local Density Approximation (LDA) combined with DMFT calculations were able to reproduce these results [83, 100].

Fig.1.9 shows the electronic structure as understood today. The e_g^π states lie under the a_{1g} states, the Coulomb repulsion has the effect of increasing the trigonal distortion that splits the e_g^π and the a_{1g}, and reduces the coherent weight of the a_{1g}. It is important to notice that the bonding orbital a_{1g} is unoccupied, which is unusual since it normally tends to lower the system's energy. The a_{1g} orbital is along the c axis and can be seen in Fig.1.9 a). The work from Saha-Dasgupta et al using LDA+DMFT really refined the understanding of V_2O_3 electronic structure [167, 150] and showed that the trigonal distortion is responsible for the MIT. The Coulomb repulsion can be considered constant. Hard X-ray photoemission have confirmed this vision [69].

Theoretical calculations predicted a strong quasiparticle peak (QP) near the Fermi energy. But photoemission spectroscopy measurements were unable to see it [181, 180]. It was only until high energy photoemission spectroscopy was done that a strong quasiparticle peak was seen [127, 129, 128, 144]. Since high energy photoemission probes deeper into the volume (see chapter 3 Fig.3.16), the quasiparticle surface sensitivity can be inferred as was discussed in [21, 157]. Fig.1.10 shows the photoemission spectra for V_2O_3 and $(V_{0.972}Cr_{0.028})_2O_3$. The quasipar-

ticle peak for PM is reduced with increasing temperature. This reduction of the quasiparticle peak is due to the crossing into the crossover regime. Mo et al were able to see the same crossing to the crossover regime for the PI [128]. The slight change of lattice parameter with temperature changes the e_g^π a_{1g} orbital splitting, the a_{1g} becomes less coherent with temperature [11, 189].

In the Hubbard model the main driving force of the MIT is the electrons but as we have seen in V_2O_3 this transition is extremely sensitive to the crystal lattice parameters. Which is the driving force of the MIT, the lattice or the electrons? The consensus today is that the lattice structure drives the transition, but the electron-lattice interplay is still an open question today. The way to answer it would be to decouple the lattice and the electron temperature in order to force the transition in the 1.1% Cr doped V_2O_3 from lower temperature PM to the high temperature PI. We will try to answer this question using ultrafast experiments.

1.3 $BaCo_{1-x}Ni_xS_2$: a moderately ionic Mott insulator

I will now present the Mott insulator $BaCo_{1-x}Ni_xS_2$. We have chosen this compound because it presents several differences with respect to V_2O_3. $BaCo_{1-x}Ni_xS_2$ is mostly a 2D material with a moderately ionic d-p bonds system, and has 3 active orbitals near the Fermi level, whereas V_2O_3 is 3D with very strong d-p bonds mixing, and only has 2 orbitals near the Fermi energy. Since these materials are very different, the comparison of their transient properties will allow us to understand the general trends of out-of-equilibrium behavior of Mott insulators. The out-of-equilibrium properties will be shown in chapter 6.

The $BaCo_{1-x}Ni_xS_2$ system is an interesting example of a MIT controlled by doping. Its phase diagram is similar to that of cuprates (see Fig.1.11) but no superconductivity is found. At low doping, the system is a paramagnetic insulator which orders antiferromagnetically at about 305 K. The MIT is crossed for a doping of x=0.16 at 300 K and can also be crossed using pressure [171, 207]. I will first present the crystal structure then its electronic structure.

1.3.1 Crystal Structure

The system is isostructural in the whole phase diagram. No symmetry breaking is seen at the MIT, which is why the transition is a Mott transition. The structure is tetragonal formed by a square lattice of pyramidally coordinated Co or Ni ions.

Fig.1.12 shows the unit cell of $BaNiS_2$ and its first Brillouin zone. The lattice parameter are a=4.44 $\AA$ and c=8.93 $\AA$ and its symmetry is P4/nmm [118]. The

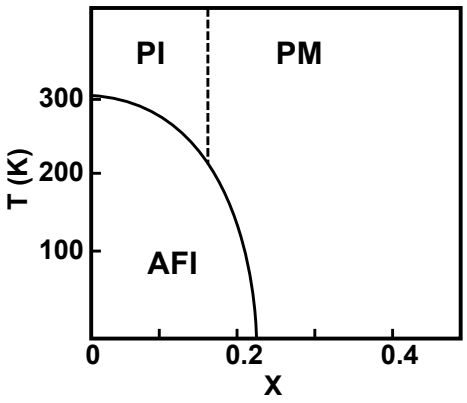

Fig. 1.11: Phase diagram of $BaCo_{1-x}Ni_xS_2$, three phases are present: PI, PM, and AFI.

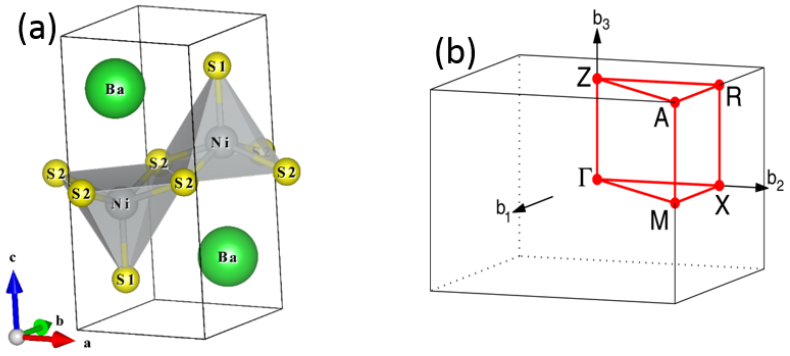

Fig. 1.12: a) Unit cell of $BaNiS_2$ b)First Brillouin zone

lattice parameter, a, increases to 4.57 $\AA$ when substituting Ni by Co. The change of lattice parameter is also seen in V_2O_3 when the MIT is crossed.

The crystals were grown using self-flux method [178] by the laboratory IMPMC at Université Pierre et Marie Curie. The typical crystal dimensions are 500x500x100 μm. The c axis is along the thickness and the ab-plane in the surface. The natural cleavage plane is the ab-plane, therefore the c axis is towards the analyzer in ARPES experiments.

1.3.2 Electronic Structure

The electronic structure of $BaCo_{1-x}Ni_xS_2$ is still not fully understood. A few theoretical calculations have been carried out but none of them can really account for the MIT [119, 82, 213]. On the experimental side only one ARPES study was performed on compounds near the transition [172]. The quality of the experimental data was fairly poor and the bands were hard to distinguish.

In order to understand the compound we performed ARPES experiments on the two extreme dopings for x=0 and x=1. The results presented hereafter are the first high resolution ARPES experiments done on these compounds. This work is a collaboration with David Santos-Cottin, Michele Casula, Yannick Klein, and Andrea Gauzzi (IMPMC at Université Pierre et Marie Curie). The aim was to first understand the Ni compound, which is the less correlated thus the band structure is easier to calculate using DFT+U. And then use the calculated band structure to understand the Co compound, which is more correlated. These strongly correlated calculations have to be done using more complex many body theories such as DMFT. The Co compound calculations have not yet been performed but the ARPES experiments allow us to understand the basic electronic properties.

Fig.1.13 shows the ARPES spectra at 100 K on $BaNiS_2$ along ΓM and ΓX directions for s and p polarizations. The data show a very strong dispersion with very narrow bands. The experiments were performed at the BaDELPh beamline at the ELETTRA synchrotron (Trieste, Italy). The photon energy was 26 eV and the energy resolution was limited by the temperature broadening, which is 37.6 meV for 100 K. The analyser slits were in the plane of the incident beam and the surface normal. Therefore the symmetry character of the orbitals could be easily seen using s and p polarization.

The 3d orbital of the Ni atoms has three active bands near the Fermi level, d_{xz}/d_{yz}, $d_{x^2-y^2}$, and d_{z^2}. The symmetry of the orbitals compared to the scattering plane are:

Orbital	d_{z^2}	d_{xy}	$d_{x^2-y^2}$	d_{yz}/d_{xz}
ΓM	even	even	odd	odd
ΓX	even	odd	even	even

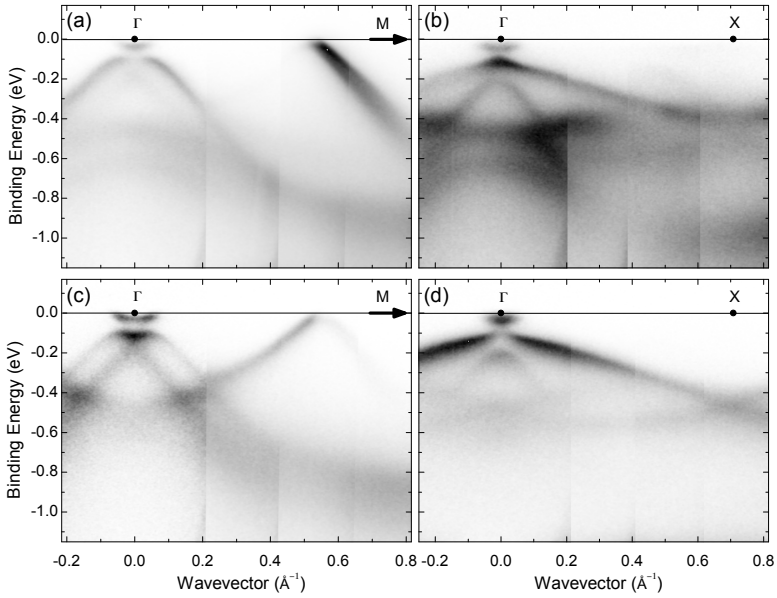

Fig. 1.13: Band dispersion in $BaNiS_2$ measured by ARPES along ΓM (ZA) and ΓX (ZR) direction for p polarization (a), (b) and s polarizations (c), (d)

As explained in 3.4.2, s polarization sees mostly odd symmetries and p polarization sees mostly even symmetries. For example the band near 0.6 $\mathring{A}^{-1}$ in the ΓM direction has a d_{z^2} or d_{xy} character for p polarization and a $d_{x^2-y^2}$ character for s polarization. The calculations in Fig.1.14 agree well with the symmetries found using ARPES. The orbitals at 0.6 $\mathring{A}^{-1}$ in the ΓM direction are d_{z^2} and $d_{x^2-y^2}$. The orbitals at the Γ point are mostly d_{xz}/d_{yz} and $d_{x^2-y^2}$.

In order to account for the band dispersion found with ARPES, the best U value for the DFT+U calculations was found to be 3 eV. Indeed with this U value, DFT+U finds the existence of the electron pocket at Γ and the hole pocket in the middle of ΓM. However the calculations find an electron pocket at R and a dispersion along k_z in the ΓZ direction. Fig.1.15 shows the k_z dispersion along ΓM direction. No dispersion is seen while varying the photon energy. Therefore we can conclude that the material is mostly 2D. Nevertheless according to the calculations the biggest dispersion along k_z should be at the X point and we have unfortunately not done the measurements along that direction. However the experimental data strongly suggest that this material is 2D.

The Fermi surface of $BaNiS_2$ is shown in Fig.1.16. The electron and the hole pockets are clearly visible. We now look at the ARPES measurements on the Mott compound $BaCoS_2$. The experiment was performed using 100 eV photons with a resolution of 10 meV at the Cassiopée beamline located in the SOLEIL synchrotron. The ARPES data on $BaCoS_2$ were taken with no specific sample ori-

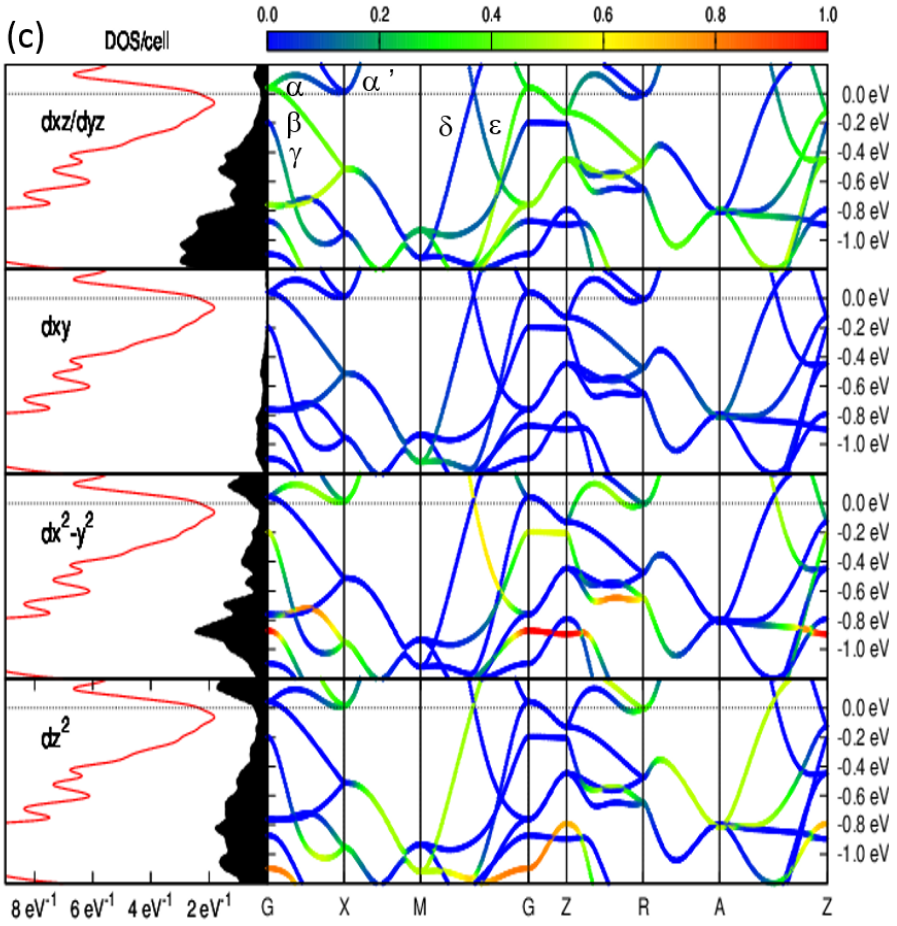

Fig. 1.14: Band structure calculations for $BaNiS_2$ using DFT+U (U=3 eV).

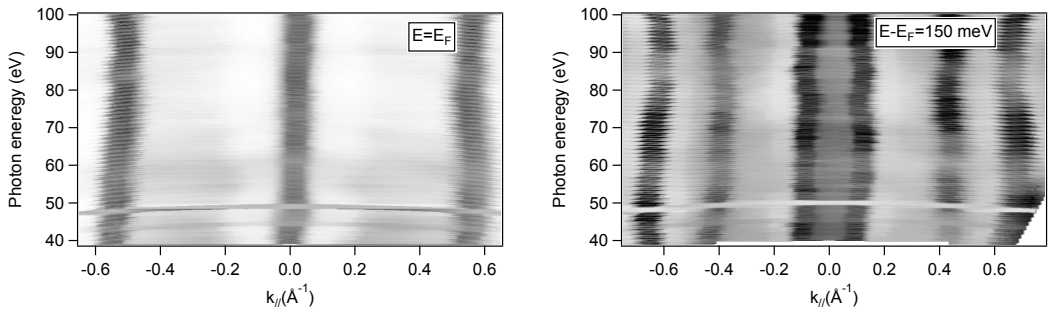

Fig. 1.15: K_z dispersion along ΓM direction for $BaNiS_2$, at E_F and at E-E_F= -150 meV. No dispersion is seen therefore the material is mostly 2D.

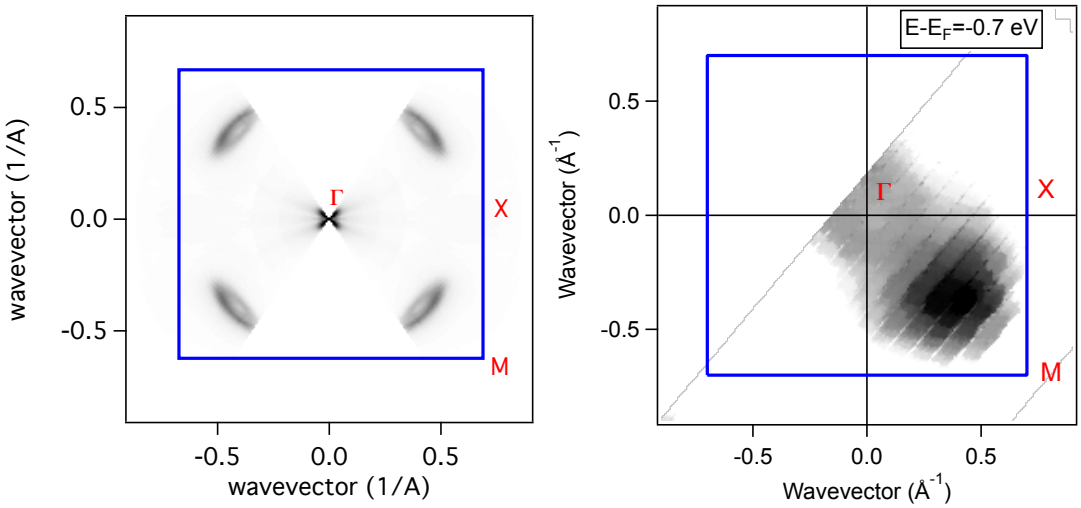

Fig. 1.16: Fermi surface for $BaNiS_2$ and isoenergy surface at E-E_F=-0.7 eV for $BaCoS_2$

entation therefore the symmetry analysis can not be properly performed. Fig.1.16 shows the isoenergy surface at E-E_F=-0.7 eV. A reminiscence of the hole pocket of $BaNiS_2$ at the middle of the ΓM direction is present in $BaCoS_2$, as well as the electron pocket at Γ. The symmetry operation was not performed on the isoenergy surface image, only the lower right corner was plotted.

Looking at the ARPES dispersion image in Fig.1.17, one can identify the same bands as for $BaNiS_2$. The d_{xz}/d_{yz} and $d_{x^2-y^2}$ at the Γ point are shifted to lower energies and are much broader. The bands at the middle of the ΓM direction are also shifted to lower energies. The band gap is about 0.4 eV. In presence of electronic correlations, an incoherent part is added to the non interaction spectral function [46]. The effect of this incoherent part is to increase the effective mass of the quasiparticle, as well as shifting the bands to lower energies. The lifetime of the quasiparticle also increases when coming closer to the Fermi level, instead of being independent of the distance to the Fermi energy. The limited lifetime of the quasiparticle under the Fermi energy broadens the electronic bands, the renormalization of the mass diminishes the dispersion, and the shift of the bands makes the material become an insulator. All these effects are seen in the band structure of $BaCoS_2$. This compound really shows how the correlation effects tend to broaden the bands, reduce their dispersion, as well as open a band gap.

The difference with V_2O_3 is striking. V_2O_3 band structure has almost no dispersion and very broad bands even in the PM phase, which proves that the pure V_2O_3 has strong correlations. The narrow band of $BaNiS_2$ suggest a rather small correlation effect.

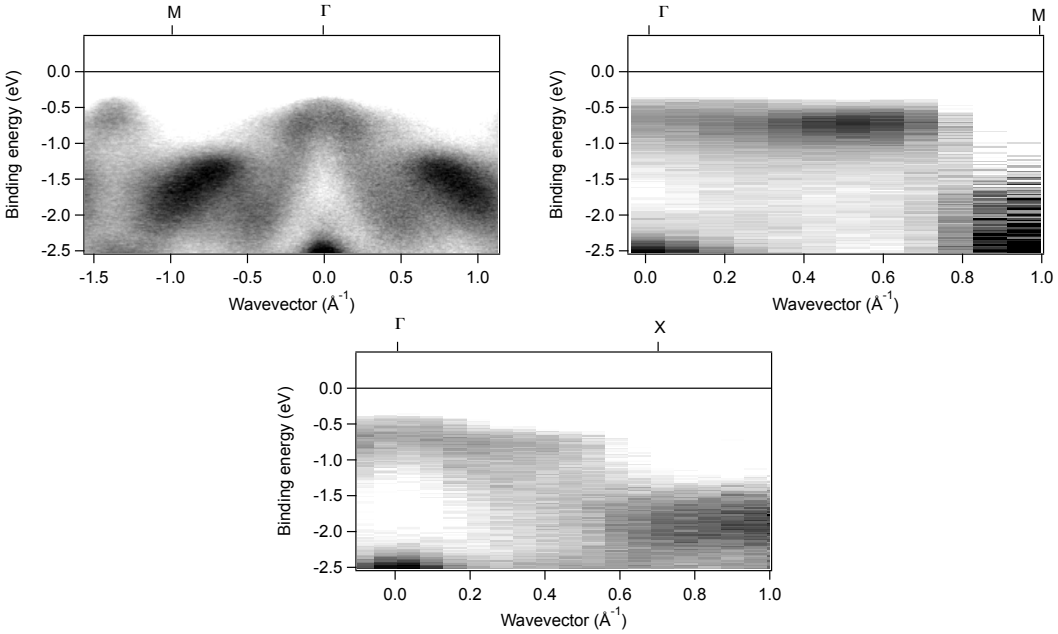

Fig. 1.17: Band dispersion in $BaCoS_2$ measured by ARPES along ΓM and ΓX. The band structure shows reminiscence of the metallic compound dispersion but the bands are shifted to lower energies and are broader due to correlation effects.

Chapter 2

Physics of ultrafast phenomena

2.1 Introduction

Physics of ultrafast phenomena has two main objectives: the former is better understanding the ground state of the material as well as its excited states, and the latter is manipulating its physical properties. In terms of input power, the first one aims at perturbating the system as little as possible using the lowest possible power and the second one, on the contrary, pushes the material to its limit by highly exciting it. Note that if one can manipulate the properties of the material, a lot of information on the ground state and the excited state can be obtained.

The main idea of this kind of ultrafast experiments is to probe the response function of the material after an optical excitation. The system is excited by a pump and is then observed after a controllable delay with a probe. The relaxation processes will give useful information on the coupling between the different degrees of freedom. In the eighties, the first ultrafast experiments were done to study the electron-phonon coupling in metals [7]. The optical pump excites only the electrons that are decoupled from the lattice for a short instant and then relax their energy through phonons. The experiment can be modeled by taking two thermal baths and introducing a coupling between them. This model is called the two temperature model. In the nineties, semiconductors were investigated to study the Coulomb correlation in excited free carriers [10]; many theoretical developments took place to explain the coherent phenomena. The next logical step was to study correlated materials in out-of-equilibrium [143]. These materials are very appealing to study with time-resolved techniques because they contain many degrees of freedoms therefore many relaxation paths can be identified and give insight on the different correlations. Since strongly correlated materials exhibit a rich phase diagram with many competing or intertwined phases [66], the energy promiscuity of the phases makes them an ideal playground to induce phase transitions with

light.

In this chapter I will first present the optical excitation and relaxation processes in solids. The behavior of metals and semiconductors under optical excitation will be presented before introducing out-of-equilibrium physics in strongly correlated materials. Finally I will examine the emerging out-of-equilibrium theories of correlated materials. In this review chapter I will not show any study done on magnetic materials [101, 27].

2.2 Ultrafast experiments

2.2.1 Light matter interaction

2.2.1.1 Excitation processes

When a photon reaches a material, it can be either reflected, transmitted, or absorbed. The sum of the probability of these three contributions is one. The light intensity after the penetration of a thickness z of the material is [203]:

$$I(z) = I_0 e^{-\alpha_{abs}(\omega)z} \tag{2.1}$$

Where $\alpha_{abs}(\omega)$ is the absorption coefficient, which depends strongly on the light frequency and the material, defined as :

$$\alpha_{abs} = \frac{2\omega k(\omega)}{c} \tag{2.2}$$

where $k(\omega)$ is the imaginary part of the the complex index of refraction. The relation between the dielectric function and the refractive index is $\epsilon_1 + i\epsilon_2 = (n + ik)^2$. We will stay in the linear regime for the dielectric function. Therefore there is no dependence on the electric field strength. For optical wavelengths, the photon can be absorbed by the material by interband transition or intraband transition as shown in Fig.2.1. An interband transition is an optical transition between the valence band and the conduction band, and an intraband transition is an optical transition inside the same band. These transitions have to obey energy and momentum conservation rules :

$$\hbar\omega = E_f - E_i \pm \hbar\omega_q \tag{2.3}$$

$$\vec{k}_{\hbar\omega} = \vec{k}_f - \vec{k}_i \pm \vec{q} \tag{2.4}$$

where E_f and E_i are respectively the energies of the final and initial electron states with wave vector $\vec{k}_f$ and $\vec{k}_i$. The $\pm$ signs refer to the emission or absorption of a phonon with energy $\hbar\omega_q$ and wave vector $\vec{q}$. An interband transition with a

phonon that is absorbed or emitted is called indirect, which underlines that the initial and final states do not have the same wave vector. An intraband transition always involves a phonon because there is no final state available with the same wave vector.

The transition probability is given by the Fermi golden rule [44]:

$$P_{i\to f} = |\langle f|H|i\rangle|^2 \tag{2.5}$$

$$H = \frac{1}{2m}\left[\mathbf{P} - q\mathbf{A}(\mathbf{R},t)\right]^2 + V(R) - \frac{q}{m}\mathbf{S}\cdot\mathbf{B}(\mathbf{R},t) \tag{2.6}$$

where $\mathbf{A}$ is the vector potential, $\mathbf{B}$ the magnetic field, $V(R)$ the atomic potential, $\mathbf{P}$, $\mathbf{S}$, q, and m are respectively the momentum, the spin, the charge, and the mass of the electron, $|i\rangle$ and $|f\rangle$ are the initial and final wave functions. In order for the transition probability be different from zero, the total symmetry of equation 2.5 should be even. Therefore, if $|i\rangle$ and $|f\rangle$ are even, H has to be even for the probability to be different from zero. If $|i\rangle$ is odd and $|f\rangle$ even, H has to be odd. Analyzing the symmetry of the initial and final wave functions and the transition operator one can find the following selection rules [44]:

Transition operator	Δ l	Δ m
Electric Dipole	±1	0,±1
Magnetic Dipole	0	0,±1
Electric Quadrupole	0,±2	0,±1,±2
Magnetic Quadrupole	±1	0,±1,±2

Where the operators are the different perturbation terms for the electric and magnetic field in equation 2.6, and Δl, Δm are the second and third quantum numbers differences between $|i\rangle$ and $|f\rangle$. Using these conservation and selection rules, the pump wavelength can be adapted to selectively excite a particular transition from one band to another. Two kind of pump methods exist, which are incoherent or coherent pumping. Incoherent pumping is nowadays the most common: it supposes that the pump excites every band and no particular optical transition is triggered, the photon energy is usually between 1 and 3 eV. One can view it as injecting energy in a system and observing the relaxation processes. Incoherent pumping is usually applied to materials with a large band structure continuum such as metals, see section 2.2.2.1. However the domain is evolving more towards coherent pumping, which tries to selectively provoke a specific optical transition between two bands or excite a collective mode. For optical wavelength the pump excites a transition between electronic bands. For lower wavelengths, the pump can be tuned to resonate with a specific collective mode such as phonons. This technique is often used to try to photoinduce phase transitions by enhancing a structural vibration mode that is thought to increase a certain competitive phase

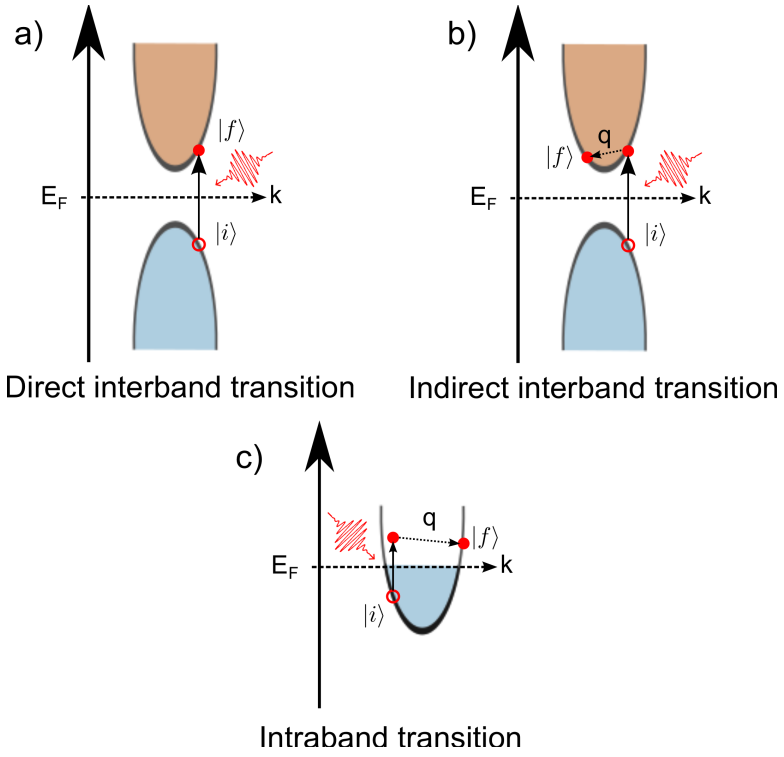

Fig. 2.1: a)Direct interband transition b) Indirect interband transition c) Intraband transition

[64, 87, 154]. For insulators, pumping above or below the gap produces different effects, the first one creates an electron hole pair and the second one acts as an AC electric field [139]. Incoherent or coherent pumping might result in a different pathway of relaxation processes, which I will present in the next section.

2.2.1.2 Relaxation processes

The absorption of the pump happens through electron excitation since the mass of the electron is much smaller than the mass of the atom, which leads to much higher transition probability as seen in equation 2.5. This excitation is very fast; it is faster than 90 attoseconds [38]. Therefore it can be viewed as instantaneous compared to the pump time length, which is usually around 10 to 100 fs. Since the electrons absorb the energy, there will be a transfer of energy from the electrons to the lattice. Once the material is photoexcited, its energy will dissipate into the lattice starting by coupling to the higher energy quasiparticle and finishing by the lower energy processes, as seen in the energy scale of Fig.2.2. The heat capacity of electrons is much smaller than the heat capacity of the lattice [102]. Therefore, in order for the electrons and the lattice to be at equilibrium, the original energy injected has mostly ended up in the lattice. Fig.2.2 shows the timescales for the different relaxation processes as well as the energy involved. The time is equivalent to the delay between the pump and the probe.

The fastest interaction is electron-electron scattering, which has a characteristic time of a few femtoseconds. This timescale is the time for the Coulomb repulsion to take effect between two charge carriers. Using Fermi liquid theory, the estimation of the time of an electron of excess energy ϵ_e to relax is :

$$\tau_{e-e} = \frac{1}{\omega_p}\frac{\epsilon_e}{E_F} \tag{2.7}$$

where ω_p is the plasma frequency, and E_F the Fermi energy. For example, in graphene the electron-electron scattering thermalizes the electronic structure in the order of 10 fs [111]: one can consider that after 10 fs the electrons follow a Fermi-Dirac distribution with a higher temperature than the lattice temperature. The relaxation processes can then be described using the two temperature model that will be presented in the following section. The pump excitation is not homogeneous inside the sample as seen in equation 2.1, the excited electrons create an electric field gradient parallel to the photon propagation, which is usually referred to as the z direction. This field promotes electron transport from to surface to the bulk, which can take place in a diffusion or ballistic regime. The characteristic time of the diffusion can be as fast as few tens of femtoseconds [23], or in the picosecond range [204].

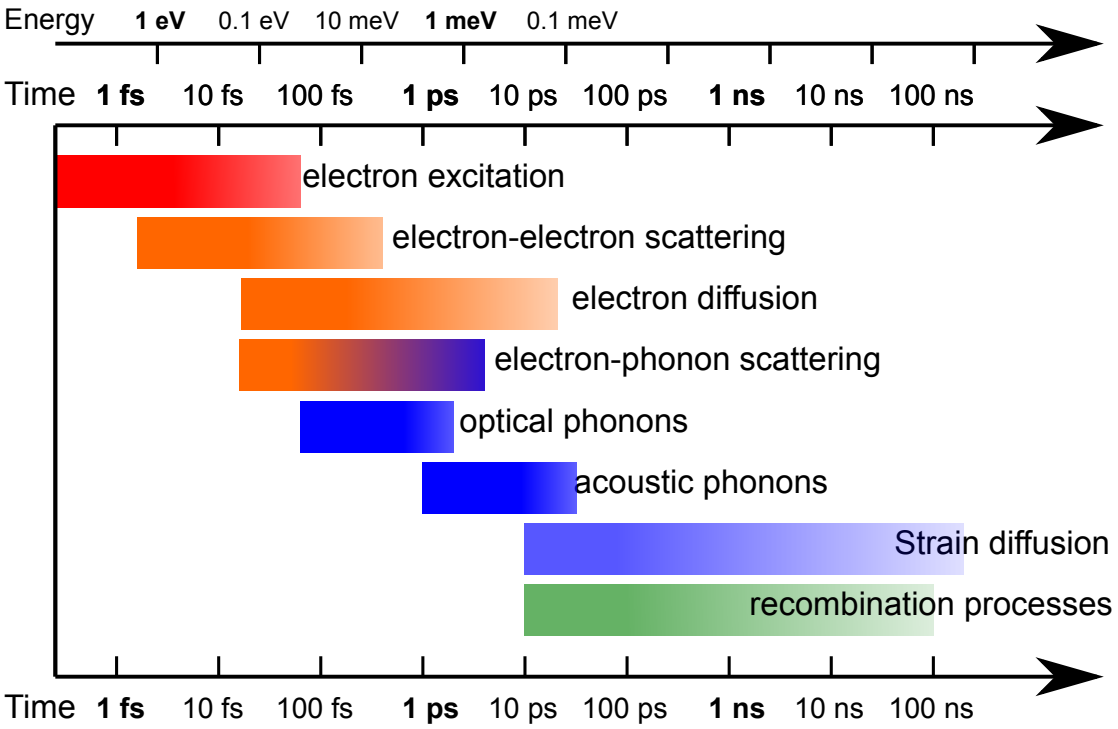

Fig. 2.2: Characteristic timescales for relaxation processes

The electron coupling to the lattice starts by the coupling to the optical phonons. The higher the energy of the phonon the more effective the relaxation is, see equation 2.10. The relaxation through the lattice is guided by the electron-phonon coupling. The higher the coupling, the faster the relaxation. The electron-phonon coupling is an important value because it estimates the interaction between the electrons and the lattice, which is an essential component for conventional superconductivity theory (BCS theory [12]). The timescale of the electron-phonon scattering depends on the phonon frequency and the coupling, if the optical phonon is energetic and the coupling strong, the relaxation due to the electron-phonon coupling will be seen earlier, usually starting after 100 fs.

Once the energy is relaxing through the lattice, acoustic phonons evacuate the energy through the sample creating strain diffusion. Strain diffusion can be characterized by the sound velocity, which is very material dependent. In V_2O_3 the sound velocity is in the order of 5 10^5 cm/s or period of tens of picoseconds. The recombination of electron-hole pairs happens around the same time.
We have seen how electrons are excited by a laser pulse and how they relax through the lattice. The different timescales of the relaxation processes give an insight on the coupling of different phenomena. We will now look at these phenomena in materials with robust band structure and then review the experiment done on

correlated materials.

2.2.2 Non correlated materials

2.2.2.1 Metals

The band structure of metals is continuous near the Fermi energy therefore no particular optical transition is excited, all the processes seen in Fig.2.1 can occur. The general accepted view is that the energy of the pump is given to the electrons that soon after relax through the lattice. At first approximation, the electrons and the lattice can be viewed as two thermalized interacting baths with a coupling constant between them. The thermalization supposes that the electrons follow a Fermi-Dirac distribution with a certain temperature and the phonons follow a Bose-Einstein distribution with a different temperature. This model was first described in 1957 by Kaganov et al. [97] and reintroduced to describe laser heating in 1974 by Anisinov et al [7]. The main equation for the two temperature model is :

$$C_e \frac{\partial T_e(t)}{\partial t} = P(t) - g(T_e(t) - T_L(t)) \tag{2.8}$$

$$C_L \frac{\partial T_L(t)}{\partial t} = g(T_e(t) - T_L(t)) \tag{2.9}$$

where T_e, C_e, T_L, and C_L are respectively the electronic temperature and its heat capacity, the lattice temperature and its heat capacity. $P(t)$ is the power source, which is given by a Gaussian function with the pump time length. g is the coupling constant, which is a function of the phonon frequency and the electron phonon coupling [2]:

$$g = \frac{3\lambda\omega^2}{\hbar\pi k_B T_e} \tag{2.10}$$

where $\lambda\omega^2$ is the second momentum of the Eliashberg coupling function [58], λ is the electron-phonon coupling, and ω is the phonon energy. Many metals have been studied using the two temperature model [59, 174, 208, 68]. The typical relaxation rate for metals is usually 1-4 ps, the peak electronic temperature is 1000-2000 K for about 1-2 mJ/cm^2 and the lattice heats only about 20 K once the electrons have relaxed their energy to the lattice.

Since the two temperature model is phenomenological, many variations of the two temperature model exist. A new term is added for each physical process. For bulk samples, an electronic diffusion term is added [187, 23]. The lattice temperature can be divided into two phonon baths with one more coupled to the electrons, introducing a third temperature[147]. For magnetic materials, a third temperature for the spin is added [16]. Since the model is phenomenological, no real prediction can be made therefore the model can not be invalidated and its

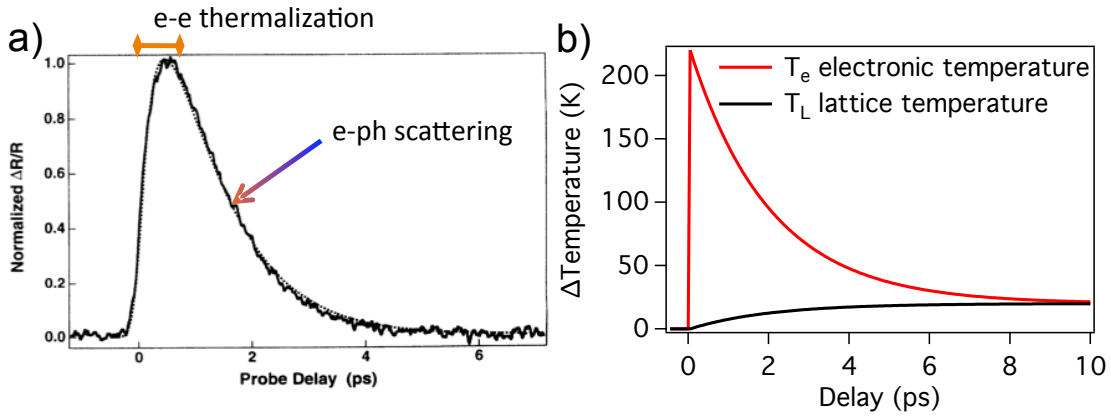

Fig. 2.3: a)$\Delta R/R$ for gold (from [186]), b) Effective temperature for the electrons and the lattice after a short laser pulse excitation.

implications have sometimes been overinterpreted in the recent years. The model really serves as a standard to compare different materials between each other. The faster the relaxation, the stronger the electron-phonon coupling.

In 1993, Sun et al. observed that the electron distribution in gold takes 500 fs to reach a Fermi-Dirac distribution thus the first hypothesis of a thermalized bath is invalid [187, 186]. A new model was created to account for the non thermalized state by [75]. It is important to notice that the notion of temperature can not be used if the electrons do not follow a Fermi-Dirac distribution. Fig.2.3 shows the differential reflectivity $\Delta R/R$ for a gold thin film and a corresponding temperature change for the electrons and the lattice. The first 500 fs the electrons are still thermalizing and the energy is then relaxed through the lattice, which takes about 4 ps. Theoretical thermalization process in metals can be calculated using time-dependent Botlzmann equation and it is shown that at low temperature electron-electron and electron-phonon scattering happen at the same time [96, 136].

Although the two temperature model has many limits, it gives a physical insight on the ultrafast phenomena occurring in metals. However, one should be careful when estimating the electron-phonon coupling with a two temperature model. The idea of raising only the electronic temperature while keeping the lattice cold is the main motivation for studying correlated materials where the density of state is extremely sensitive to the different degrees of freedom including the electronic temperature. Before doing so, we will examine highly excited semiconductors.

2.2.2.2 Semiconductors

The physics of ultrafast phenomena in semiconductors is extremely rich. The main reason is that the pump pulse creates excitons that are long lived and can

interact with the different degrees of freedom of the material. Since semiconductor fabrication is very well controlled the different degrees of freedom can be fine tuned, for example suppressing acoustic phonon relaxation pathways by creating quantum wells [22]. I will only give a brief overview of semiconductors far from equilibrium focusing on the short time scales, a more complete review can be found in [10].

There are three excitation regimes: the first is with a pump energy below the band gap which produces no absorption. The second is in resonance with the band gap that produces a strong absorption because of an interband transition: the electron-hole pairs created are long lived because the excitons are fairly robust. The third regime is with an energy above the gap which also creates many excitons but their coherence disappears faster because of efficient electron-electron and electron-phonon interaction in the continuum states. The excited electrons gather at the lowest part of the conduction band while the holes gather at the highest part of the valence band.

Once the photons are absorbed, the electrons first relaxation process is to reach a quasi-equilibrium state where the valence and the conduction band can be viewed as thermalized. Then the material relaxes through recombination processes. Fig.2.2 shows the different relaxation processes that are present in semiconductors: they are the same as for metals. The electron-electron scattering and the electron-phonon scattering enable the dissipation of the energy inside the conduction and the valence band. The energy dissipation between the valence and conduction band is mostly done by recombination processes. The most interesting part of highly excited semiconductors is the many body interaction that happens before the loss of coherence. The quasiparticles are governed by Coulomb interaction and many-body physics. The main results can be found in [41].

For low excitation density, the Coulomb interaction between two excited particles is important because electron-electron scattering is reduced. The excited particles keep their coherence for longer time and mean field theory does not capture the scattering processes [103]. For higher excitation density, the electron-electron scattering rate is much higher and there is a build up of screening of the Coulomb potential that then creates a collective mode, a plasmon, like in a metal [34]. Fig.2.4 shows the inverse dielectric function for highly excited GaAs. There is an apparition of a Drude peak after 175 fs, the Coulomb interaction is then screened and the excited carriers behave like in a metal [89]. The fact that the Coulomb screening is not instantaneous shows that the screening processes are not inherent to the band but are built by the electrons inside it. Extremely strong THz pulse can also create free carriers in semiconductors by Franz-Keldysh effect [139].

In the next section I will present time-resolved measurements on Mott insulators, which have band gaps in the same order of magnitude as semiconductors. In

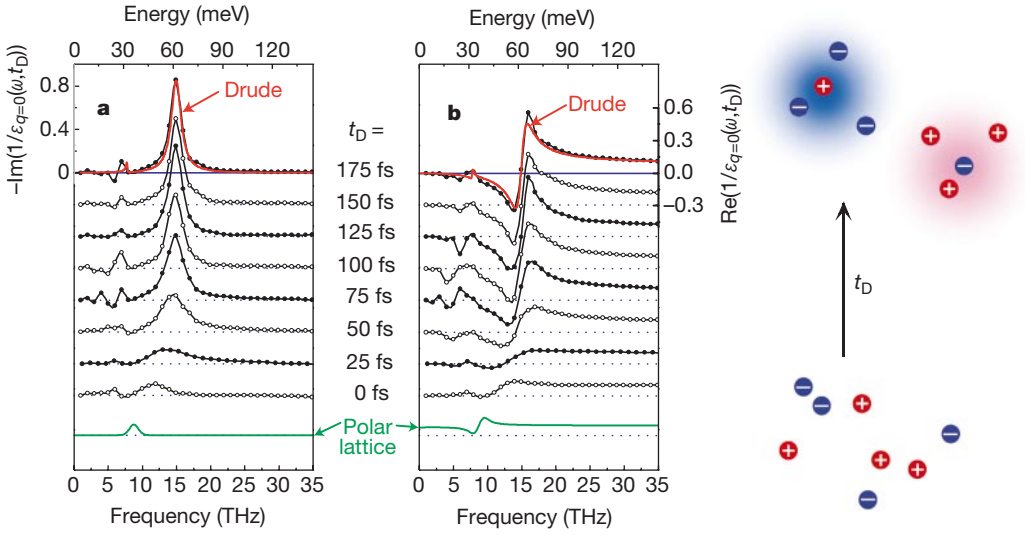

Fig. 2.4: Build-up of Coulomb screening and plasmon scattering. a) and b) are the imaginary and real part of the inverse dielectric function of GaAs. A Drude peak appears which implies that the material has become a metal after 175 fs, which is the time needed for the Coulomb screening to build-up (from [89])

Mott insulators there is also strong Coulomb interaction but it changes the band structure therefore the effect of a time dependent change of Coulomb interaction could lead to a more drastic effect. Metals and semiconductor have robust band structures compared to correlated materials therefore out-of-equilibrium physics in correlated materials is even more complex. Can photoexcited correlated metals be modeled by a two temperature model? Does the conduction band of a correlated insulator reach a quasi-equilibrium state?

2.2.3 Correlated materials

We have seen that the physics of ultrafast phenomena gives an estimation of the electron-phonon coupling and the build up of the Coulomb screening. These two ingredients are very important in correlated materials and are the main motivation to study them. Time-resolved measurements give the ability of tracking in real time the quasiparticle recombination and measure the electron-phonon coupling, which is essential for superconductors. It is logical that cuprates were among the first materials to be studied by ultrafast techniques, since the standard superconductivity theory (BCS) does not seem to apply. The investigation of the pairing mechanism with time-resolved measurements started in 1990 [80] and is an extremely active field. A Mott phase is present in the phase diagram of cuprates. Therefore Mott insulators might be an important ingredient for high-T_c super-

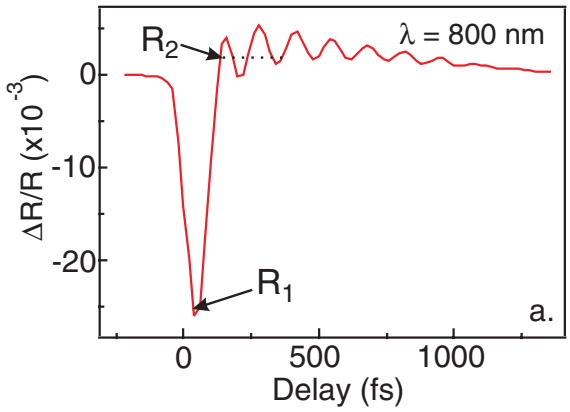

Fig. 2.5: $\Delta R/R$ for V_2O_3, the first peak is a purely electronic excitation and the oscillation are coherent phonons (from [115])

conductivity and the interplay between the lattice and the electrons is also being extensively studied with time-resolved techniques [13]. In this section I will first present work done in Mott insulators and review a few results on cuprates.

2.2.3.1 Mott insulators

In Mott insulators the electron-phonon coupling is extremely strong therefore the relaxation times are very fast. In V_2O_3 the first excitation lasts less than 200 fs [125, 115]. Fig.2.5 shows a typical time-resolved optical reflectivity for V_2O_3: the first peak is the initial electronic excitation. The briefness of this first state can arise from either very strong electron-phonon coupling, fast electron diffusion towards the non excited part of the sample, or a build up of the screening like in semiconductors. The oscillations in the line shape are the coherent optical phonons that give information on the lattice dynamics and the bond strength (see chapter 3). In Metals the band structure is very robust therefore the relaxation times are linked mostly to the electron-phonon coupling. In correlated materials the bandwidth W and the Coulomb repulsion U are very sensitive to their local environment. To really understand the origin of the first excitation, one has to understand the perturbation of the Hubbard model by a short laser pulse. Once the effect of the laser pulse is understood the relaxation pathways can be interpreted, which could differ from only electron-phonon interaction.

The laser pulse creates electron-hole pairs if the energy of the photon is higher than the gap. If the band structure is robust such as in semiconductors, the excitons will evolve according to the system's equilibrium parameters. In 1D Mott insulators and for low excitation fluences, it seems that the band structure does not change. Each atom has only 2 neighbors and the Coulomb screening is less

important compared to the other energies involved. M. Mitrano et al. were able to tune the hopping parameter using pressure in an 1D Mott insulator while keeping the other parameters constant [126]. They showed that the relaxation rate is a function of the hopping and there was no need to change the other parameters of the system. More subtle phenomena can be seen in 1D chains at very short time scales such as a fast oscillatory component in the first 100 fs. This oscillation can be seen as an oscillation between two quantum wells where the oscillation is a function of the Coulomb repulsion and the hopping parameter [195]. When raising the dimension, the coordination increases therefore the interaction between neighboring sites becomes more complex. The Hubbard model becomes harder to solve and the relaxation rate can not be simply calculated. Many approximations have to be made.

The first approximation is to consider that the excited electrons are heated to a very high temperature while the other parameters of the system are left untouched, the same mechanism as in metals. L. Perfetti et al. showed using for the first time time-resolved ARPES that the excited spectral function of 1T-TaS_2 was very similar to the higher temperature spectral function calculated using DMFT with a frozen lattice approximation [146], the Born-Oppenheimer approximation. Fig.2.6 shows the time-resolved ARPES spectra and the spectral function calculated for different temperature. The two qualitatively agree but there are strong differences. For the 100 fs spectrum, significant spectral weight can be seen lower than -0.2 eV, which is not present for the calculated 1320 K spectrum. On the opposite for 550 fs at -0.2 eV there is no more spectral weight, which is present for the calculated 1100 K spectrum. These large discrepancies point towards a change in other parameters than only the electronic temperature.

There can be two other parameters that can vary after an electronic excitation, the Coulomb repulsion U or the Bandwidth W. The bandwidth is equivalent to the hopping parameter. In G. De Filipis et al. model, they take the laser pulse as a perturbation of the hopping parameter [49]. The other interesting addition to this model is the coupling to a bosonic bath to account for the electron-phonon coupling. This will be analyzed in more details in section 2.3. Using this, F. Novelli et al. were able to account for the difference between pumping above or under the charge transfer gap in La_2CuO_4 [138]. When pumping above the gap, the materials reaction is similar to an increase of temperature. However when pumping under the gap, there is the apparition of a quasiparticle dressed by a bosonic field. The effect is similar to a small hole doping. A hole doping is also equivalent to a change in the Coulomb repulsion parameter or the filling of the bands.

Contrary to 1T-TaS_2, experiments on UO_2 have shown that spectral weight is present in the upper Hubbard band when it is excited [72]. The authors conclude

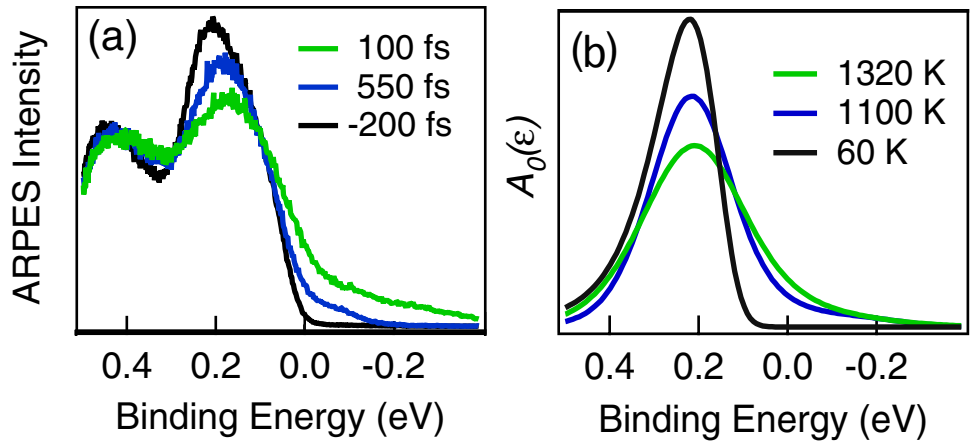

Fig. 2.6: a) 1T-TaS_2 Time-resolved photoemission spectra for a delay of 100 fs, 550 fs and -200 fs. b) Spectral function calculated with DMFT for electrons heated at 1320 K, 1100 K, and 60 K (from [146])

that UO_2 is a robust Mott insulator. The distance between the lower and upper Hubbard band gives directly the Coulomb repulsion U. S. Gilberston et al. observed that there is no breakdown of the Mott gap when UO_2 is excited as opposed to other narrow band Mott insulators. They explain that this might be due to the large gap of 2.3 eV. Nevertheless the upper Hubbard band shifts with time, which is different from a thermalization of the electrons in the upper Hubbard Band that would produce an accumulation in the lowest part of the band. This shift can portrait a change of the Coulomb repulsion in the material during the relaxation process. I will present a study on V_2O_3 in whole phase diagram in chapter 5 and 6 in order to try to disentangle the different parameters, which are the electronic temperature T_2, the lattice temperature T_L, the Coulomb repulsion U, the bandwidth W, and the specific orbital filling.

In every phase transition the lattice structure changes during the transition. Either the symmetry is broken like in VO_2 [73] or the symmetry is constant but there is nevertheless a jump of lattice parameter like in V_2O_3 [122]. In N.F. Mott views, the transition should be only driven by the electrons and the lattice structure should be fixed but it seems that a small structural variation is needed to stabilize the insulating phase. Indeed near equilibrium experiments have shown that during the Metal-to-Insulating transition the lattice is distorted [156, 158]. In theoretical models a change in the lattice parameters is needed to stabilize the different phases [150]. In physics of ultrafast phenomena, the electrons are decoupled from the lattice for brief instant therefore a pure electronic phase could be observed. If one can follow the electronic structure and the lattice structure in real time during a phase transition, one could possibly observe whether the electronic or the lattice

transition is a precursor to the other or if both are simultaneous. In the past few years there has been many reports of photoinduced phase transition. I will now give a few examples focusing on Mott insulators.

V. Guiot et al. showed that the Mott family GaV_4S_8 could be switched from insulator to metal using a microsecond electric pulse of a few kV/cm [76]. Although the timescales of these pulses are much longer than a laser pulse, they also inject hot electrons. The switching can either be irreversible or reversible according to the pulse strength. The whole material does not transit entirely but filamentary metallic paths are created [52]. Therefore the stable metallic phase is stabilized by the structure. They were able to show that this breakdown was universal to all narrow band Mott insulators and that it was similar to an avalanche mechanism [184, 185]. Unfortunately electric pulses are long and it is not possible to decouple the lattice and the electron dynamics. The same switching was seen in the manganese oxide $Pr_{0.7}Ca_{0.3}MnO_3$ with a ns laser pulse [65]. This observation supposes that the electric and the laser pulse play a similar role. To avoid lattice heating fs pulses have to be used. The switching from insulator to metal was observed in 1T-TaS_2 at 10 K using a 35 fs 1mJ/cm^2 800 nm laser pulse [183]. They infer that a new phase arises called the H phase that is a reorganization of the cluster of electrons. They argue that the nature of the transition is different from the time-resolved ARPES measurements done by L. Perfetti et al. and other transient metallic states seen in Mott insulators [91]. In irreversible transition the nature of the transition is hard to track since the transition happens only once and the specific time scales can not be distinguished. The photoinduced phase transition in VO_2 is very interesting because the structural and the electronic dynamics can be observed since the materials transits back to insulator after heat dissipation.

In 2001, A. Cavalleri et al. were able to photoinduce the high temperature metallic state from the low temperature insulating state in VO_2 [40]. The optical reflectivity and the time-resolved X-ray diffraction were able to show that the photoinduced state was the metallic high temperature phase. The question was whether the transition was structurally or electronically driven. A structure transition is limited by the speed of the phonons while an electronic transition can happen much faster. Therefore probing the time scale of the transition can give insight on the driving force. Fig.2.7 shows a schematic view of the insulator to metal transition. Path 1 is a transition where the transition is driven by the electrons along the electronic state S_e and path 2 is a transition driven by the lattice along S_L that then drives the electronic state. The transition in VO_2 was originally thought to follow path 2 [39, 14] because the switching time given by the reflectivity showed a bottleneck of 80 fs, the time needed for the structure to react. More recent experiment have shown that this transition is not limited by this bottleneck [197, 196]: especially a time-resolved ARPES study, where it

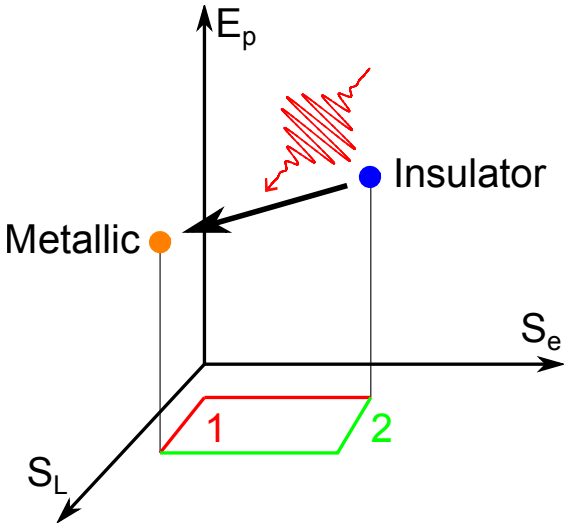

Fig. 2.7: Schematic view of a photoinduced phase transition in VO_2. S_L and S_e are the lattice and the electronic state. The two paths 1 and 2 represent respectively the scenario where the electrons trigger the phase transition or the lattice.

is seen that the system becomes metallic almost instantaneously therefore faster than the bottleneck [200]. Another time-resolved study using high harmonics argue that the instantaneous metallization is different from the equilibrium metallic phase and the system takes 1 ps to evolve towards the equilibrium metallic state [211]. A similar transient metallic state is seen in V_2O_3 and the interpretation of mechanism will be discussed in chapter 6.

2.2.3.2 High-T_c superconductors

Time-resolved measurements done on High-T_c superconductors are extremely rich. Since it is not the main topic of my thesis, I will only review briefly the experiments done using time-resolved ARPES and try to relate them to pure Mott insulators. The idea behind these measurements is breaking the Cooper pairs in order to track the repairing process that is governed by the hypothetical glue. Unfortunately the ground state is very complex and many competing orders are present therefore the observations are very difficult to allocate to a certain phenomenon. Using a three temperature model with a temperature for the electrons, the phonons coupled to the electrons, and the other phonons, the electron-phonon coupling was found to be too small to stabilize the superconductivity phase by itself [147]. The dynamic response is still much faster than in low temperature BCS superconductors and depends on the phase observed whether it's in the superconductivity phase, the Fermi liquid phase, or the pseudogap

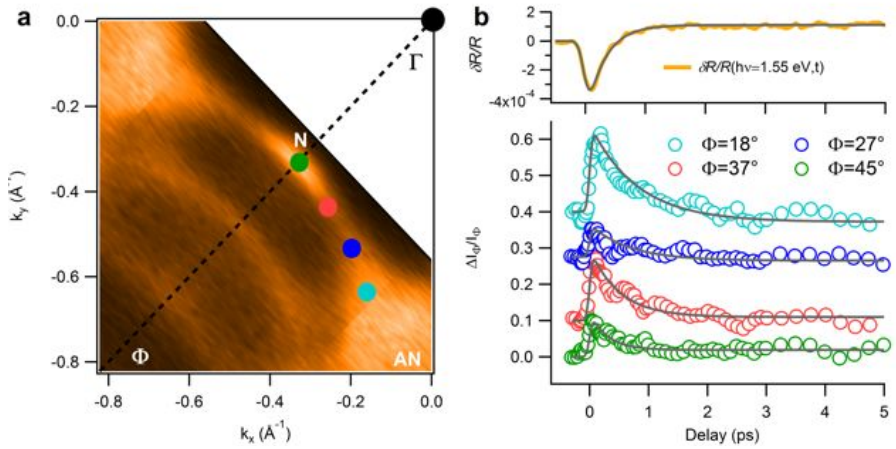

Fig. 2.8: a) Fermi surface of optimally doped $Bi_2Sr_2Y_{0.08}Ca_{0.92}Cu_2O_{8+\delta}$ at 100 K ($T>T_c$), N is referred to as the nodal region and AN as the antinodal region b) Time-resolved reflectivity and time-resolved ARPES intensity taken at the different points in a) (from [43])

phase [98, 45, 74, 179, 216]. Therefore time-resolved measurements are able to reconstruct the phase diagrams of cuprates. The advantage of using time-resolved APRES is that it directly probes the electron dispersion. Fig.2.8 shows a Fermi surface for $Bi_2Sr_2Y_{0.08}Ca_{0.92}Cu_2O_{8+\delta}$ and the time-resolved signal taken from the spectra.

Outside the superconducting phase, the physics is mostly governed by Mott physics in the underdoped sample which has different momentum region. F. Cilento et al. have shown that in the antinodal momentum region has a more Mott insulating character than the nodal region [43]. They argue that the photo-excitation actually delocalizes the quasiparticles of the antinodal region. The observation of a collapse of the Mott gap is similar to the one observed in TaS_2 and to the initial metallic state in VO_2. A more precise analysis of the momentum distribution was done by J. D. Rameau et al. shown in Fig.2.9. The momentum distribution curves according to the delay show that the effective mass of the band is reduced and the Fermi vector shifts. They argue that this is equivalent to a hole-doping. The laser excitation therefore tends to drive the system away from the antiferromagnetic Mott insulating phase. Is this mechanism the same as in standard Mott insulators? We will discuss this point in chapter 6.

Like in Mott insulators, photoinduced phase transitions have been tried in cuprates. The goal is to try to photoinduce a superconductor. We have seen that hitting the superconductor with 1.5 eV pump breaks the Cooper pairs therefore more subtle pumping is needed. M. Rini et al. showed that exciting a phonon mode in a manganite creates a metastable metallic phase [154]. The photon energy was

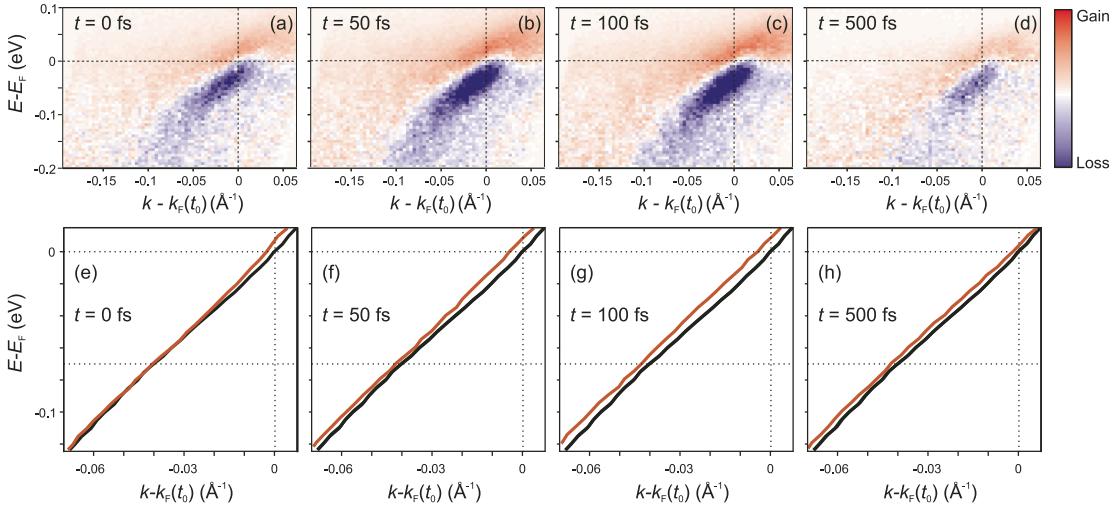

Fig. 2.9: a-d) Time-resolved ARPES spectra differences between positive and negative time delay; e-h) maxima of the momentum distribution curve extracted from a-d in red, the black line is before excitation. There is a clear renormalization of the elecron mass and a shift of Fermi wave vector, which indicate a similar behavior than a hole doping (from [152]).

exactly tuned to a specific phonon mode and it induced a five order resistivity drop. The same coherent phonon pumping has been applied on $La_{1.675}Eu_{0.2}Sr_{0.125}CuO_4$ and a Josephson plasma resonance was seen outside the superconducting dome, which is a feature of the superconducting phase [64]. This observation is very debated in the community since it has been shown that phonons can not be the only ingredient needed for superconductivity. The observation of the Josephson plasma is not equivalent to superconductivity especially if the system is out-of-equilibrium. The same strategy was used in $YBa_2Cu_3O_{6.5}$ and the probe covered a broader region of the optical spectrum [87]. It was shown that below and above T_c the coherent phonon pumping increased the inter-bilayer coupling while reducing the intra-bilayer coupling. The result points towards an enhancement of superconductivity even above T_c. Further investigations are needed since the main ingredient of superconductor is zero resistivity and the Meissner effect, which have not yet been observed with time-resolved techniques. Coherent pumping is extremely attractive and these days many experimentalists are going towards that direction.

2.3 Out-of-equilibrium theoretical models

The equilibrium state of Mott insulators is already a very difficult problem therefore out-of-equilibrium Mott insulators is an even harder one. In order to explain experimental results out-of-equilibrium theories have to take into account the way the materials are excited by the laser pulse. The excitation of the material is not homogeneous; it follows an exponential decay from the surface to the bulk. The second spatial problem to take into account is for the photoinduced transition. When a transition is photoinduced the entire material is not switched but only part of it is transformed [131]. Since most experimental probes look at an average between the switched parts and the non perturbed areas, the results differ from a total switching. The same problem can occur even if there is no metastable phase transition. These spatial problems are dealt with by taking an average between the excited state and the ground state.

There are two approaches that theorists have taken to describe out-of-equilibrium Mott insulators. The first is to artificially create holes in the valence band and electrons in the conduction band. This transcribes an optical transition done by the laser pulse and it can be seen as photodoping. The new artificial state can be calculated using standard many-body theories but the different filling has to be explicitly taken. The state calculated is a steady state and no time evolution can be really calculated. The second approach is to take the complete problem with the arrival of the pump and the relaxation processes. This method is much more complex and more computational intensive. I will describe both methods in the next two sections.

2.3.1 Steady state approach

In the density functional theory (DFT), the calculations are done by relaxing the entire crystal structure. The orbital occupancy can vary significantly according to the crystal lattice parameters. As we have seen in chapter 1, the occupancy of the a_{1g} orbital in V_2O_3 is very sensitive to the trigonal distortion. B. Mansart et al. used a "trick" to photodope the a_{1g} orbital [117]; the orbital occupancy was tuned by the lattice parameter ratio c/a. The ratio c/a was fixed at a certain value and the Wyckoff positions were let to relax. The occupancy of the orbitals and the phonon frequency were then calculated for this relaxed structure. The results of these calculations are shown in figure Fig.2.10. The change of the ratio c/a was able to tune the occupancy of the a_{1g} orbital and account for the experimentally observed phonon hardening, see chapter 4.

DFT does not account well for correlation effects, especially Coulomb screening problems. More sophisticated many body approaches such as DMFT or GW approximation can account better fore these correlations [210]. GW approxima-

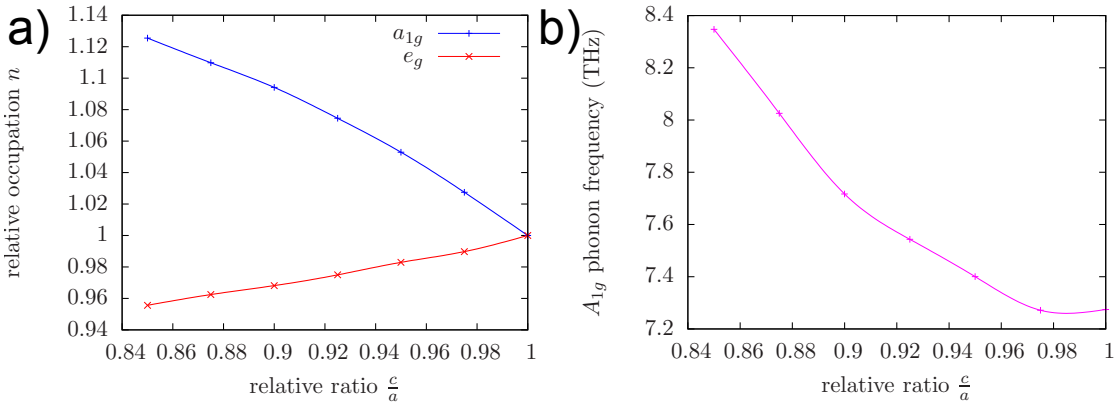

Fig. 2.10: a) Calculated variation of the orbital occupancy in V_2O_3 for the a_{1g} and the e_g orbitals versus relative ratio c/a; b) calculated phonon frequency versus relative ratio c/a. These results show that a lattice modification has an effect on the orbital occupancy. (from [117])

tion accounts well for the screened Coulomb interaction and is able to reproduce correctly the transition in VO_2. D. Wegkamp et al. showed that the collapse of the gap can be achieved by distributing holes in the valence band of VO_2 and electrons in the conduction band [200] while the lattice is kept frozen. The holes in the valence band enhance the screening and create a metallic phase. These theoretical results show that the important ingredient during the VO_2 photoinduced phase transition is the change of the Coulomb screening effects in the valence band. These results will be compared in chapter 6 to the experimental observation done in V_2O_3.

2.3.2 Full dynamical approach

The previous section showed theoretical results used to reproduce effects seen just after the pump excitation but they lacked temporal resolution, no relaxation processes or timescales can be calculated. In this section I will present results that use a full dynamic approach where time is explicitly taken as a parameter. During an ultrafast experiment, energy is brought to the system and therefore the system needs to dissipate this extra energy. This is not the case in cold atoms experiment where the out-of-equilibrium conditions are created by varying a parameter with no external force [215, 20, 149]. In order to dissipate the energy in condensed matter, the system can be coupled to a thermostat. A. Amaricci et al. showed that the Hubbard model coupled to a thermostat leads to a new stationary state for any coupling values [3]. The addition of a new dissipation term changes also the equilibrium state. Therefore the equilibrium phase diagram has to be reviewed

before any dynamical approach. Another option is to consider an explicit coupling to a bosonic bath, which can be viewed as phonons. The coupling can be affected by the perturbation pulse. The model used is the Hubbard-Holstein model [50]:

$$H_{Hub} = -t \sum_{<i,j>,\sigma} (c^{\dagger}_{i,\sigma} c_{j,\sigma} + c^{\dagger}_{j,\sigma} c_{i,\sigma}) + U \sum_{i} n_{i\uparrow} n_{i\downarrow} + \omega_0 \sum_{i} a^{\dagger}_{i} a_i + g \sum_{i} n_i (a^{\dagger}_{i} + a_i) \tag{2.11}$$

where the first two terms are the Hubbard Hamiltonian as described in equation 1.1, ω_0 is the phonon frequency, $a^{\dagger}_{i}$ and a_i are the creation and annihilation phonon operators, and g is the electron-phonon coupling. The time dependent Hubbard-Holstein model has been solved using various techniques, such as double phonon cloud method [49, 138], time dependent Gutzwiller approximation [4], or time dependent Dynamical Mean Field Theory (DMFT) [8]. These calculations are quite complex and are being done on simplified models that do not always reflect the complexity of the different orbital interactions.

The first test for these methods was to see the evolution of the system after a quench of the Coulomb repulsion U, going from 0 to a fixed U. It was seen that for medium values of U, the system returns fast to a thermalized state but for small and large U values the system is trapped in a metastable state [53, 173]. Fig.2.11 shows the double occupation calculated with nonequilibrium DMFT and time dependent Gutzwiller approximation. At the critical U_c the double occupation is zero: it is the same as for equilibrium. These results show that the system has a memory of its original state. This is underlined by the difference between starting from two different U values in Fig.2.11.b). With the same parameter values the system thermalization depends on its initial state.

Although these results are very interesting, a U quenching is very different from a laser excitation. The laser excitation can be modeled by simply injecting doublons [4] or by explicitly tuning the hopping parameter with the AC electric pulse [54, 49]. If the hopping is increased it favorizes double occupancy thus creating an electron hole pair. P. Werner and M. Eckstein calculated using nonequilibrium DMFT the evolution of a single band Hubbard-Holstein model under DC electric field and AC electric pulses [202]. Fig.2.12 shows the photoemission spectra calculated for a single band Hubbard-Holstein model using nonequilibrium DMFT. Fig.2.12 a-c show the time evolution after a laser pulse of the upper Hubbard band for different electron-phonon coupling g. Fig.2.12 d) shows the effect of a DC electric field as a comparison. During the excitation, spectral weight is seen in the entire upper Hubbard band and then it relaxes very quickly to the bottom of the band. Increasing the electron-phonon coupling creates phonon side bands already in the equilibrium state (see E=0). In-gap states are created with increasing DC electric field thus creating a collapse of the gap, which is seen in real Mott insulators with electric pulses [76]. An interesting feature is that the upper

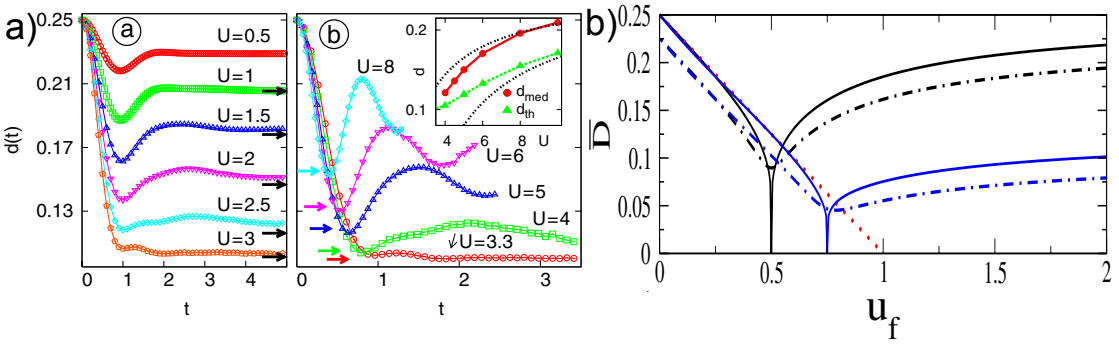

Fig. 2.11: a) Double occupation versus time after a quenching from U=0 to U calculated with nonequilibrium DMFT (from [53])b) Average double occupation in the metastable state after a U quenching calculated using time dependent Gutzwiller approximation. The blue curve is starting with U=0 and the black starting at U=0.5 (from [173]). Both calculations show the apparition of a metastable state that depends on the initial conditions.

Hubbard band has always residual weight and never really disappears contrary to experiments.

These time-resolved many body theories are very interesting and are encouraging for future development. The difference between the theories and the experiments is that they consider mostly a one band Hubbard model but in reality most Mott insulators are two band Hubbard models, for example the a_{1g} and the e_g orbitals in V_2O_3. This approach is being investigated with Gutzwiller approximation [17]. The spatial problem is also an issue, since in experiment the excitation is not uniform and only the surface is observed in photoemission. Electron diffusion and coordination problems can occur and impact the dynamic of the system. Recent calculations have also explored these issues and are able to see the diffusion of the carriers from the surface to the bulk [5, 55].

The hardest problem in modeling Mott insulators is the calculation of the Coulomb repulsion U even at equilibrium. In the early years of DMFT the U was tuned to fit with the experiment. More recently effort has been made to calculate the U using ab initio methods [190, 210], but it seems that the use of a frequency dependent U gives a better result than a static U [201]. The inherit problem of DMFT is the long range Coulomb screening that is not well accounted for, since DMFT is a purely local scheme. GW approach on the contrary is better adapted for the long range Coulomb screening effects, which can explain why D. Wegkamp et al. have found such a drastic effect in VO_2 when it is hole doped. In experiments the usual pump energy is 1.5 eV, which is fairly big compared to the energy region looked at using DMFT. Therefore the screening effect of the Coulomb repulsion might be considerably changed during the photoexcitation.

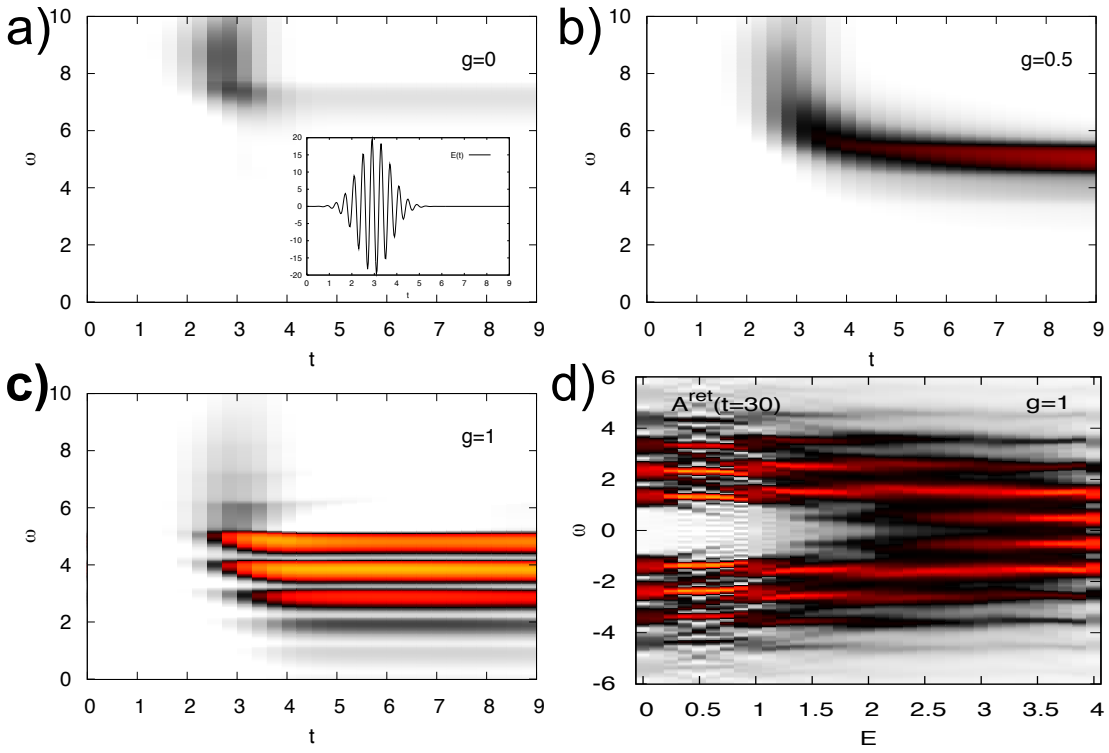

Fig. 2.12: Photoemission spectra calculated using nonequilibrium DMFT, red is more intensity and white is less. a-c) Upper Hubbard band evolution after an electric pulse excitation for different electron-phonon coupling g, the pulse is taken as shown in inset of a). d) Lower and upper Hubbard band for the metastable state arising from a DC electric field. (from [202])

An interesting theoretical approach would be to combine nonequilibrium GW and DMFT or Gutzwiller approximation in a two band Hubbard-Holstein model, to account for the dissipation pathways and the true band structure of real materials.

Chapter 3

Experimental methods

3.1 Introduction

Interactions among electrons happen at the femtosecond or even at the attosecond timescale. The electron-phonon coupling occurs faster than a few picoseconds. Therefore experimental techniques have to be able to capture these fast dynamics. The fastest electronic detection systems are as fast as 50 GHz which corresponds to a 20 ps time resolution and thus they can not observe non-thermal phenomena [31]. There are two options to access these timescales, the first one is using laser systems and the second one is using particle accelerators. In order to perform time-resolved measurements, equilibrium techniques using light or fast particles have to be adapted. These setups generally use the pump-probe scheme where the pump pulse excites the system and the probe pulse detects the system after a controllable delay, by varying the delay between the pump and the probe one can access the time-resolved evolution of the material after photoexcitation, as seen in Fig.3.1. Usually these experiments are carried out at high repetition rate in order to acquire enough statistics but the time between two pulses is limited by the complete relaxation time of the material. The probe used can be light of different wavelengths or particles such as electrons [148]. In this thesis, I will only show work done with photons.

The important part of experimental work is defining where and what we are observing. Is it the surface or the bulk? Are we observing the electrons, the lattice, or both? According to the wavelength, light can be used to probe the electronic structure or the lattice structure. Between 0 and 6 eV the transmission or the reflectivity probes the dielectric function of the material which gives information mostly on the band structure but also contains lattice information. In this region the probed depth depends strongly on the material. Above 2 keV, one can perform X-ray diffraction which probes mostly the lattice structure and has a typical

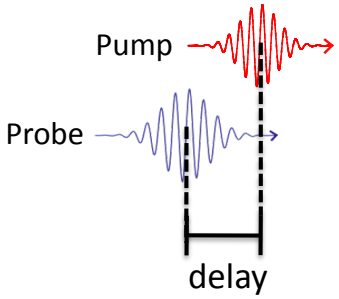

Fig. 3.1: Pump-probe scheme. The pump excites the material and the probe observes the material after a controllable delay.

probing depth of a few microns. Photoelectron spectroscopy can be perform using photons above 6 eV, it probes the electronic structure and it observes the surface but can also study the bulk at higher energy. Other techniques using photons like RIXS or EXAFS can be carried out but I will not present them in this thesis.The pump probe is usually between 0 and 6 eV.

All the techniques cited above have been used for many years but only for the past 30 years have they started to be adapted for time-resolved measurements. The advent of stable femtosecond laser systems has been the key ingredient of the emergence of time-resolved experiments. Fig.3.2 shows the different probes that are used in this work, and specifies for each the properties observed and the probing depth. The most common experiment is the time-resolved optical spectroscopy. I will present this technique in 3.2 for single color, white light, and THz time domain spectroscopy. In order to deconvolute the electronic and the lattice dynamics more direct techniques can be used. I will first present time-resolved X-ray diffraction to probe the lattice in 3.3 and then time-resolved photoemission spectroscopy in 3.5.

3.2 Time-resolved optical spectroscopy

Optical spectroscopy is a very old experimental method. It consists of analyzing for each wavelength the transmission or the reflection of a material. The first to do this was Isaac Newton (1666-1672) with his observation of the dispersion of white light through a prism. A material's optical properties can be entirely described with its dielectric function, which is related to its electronic band structure [203]. Time-resolved optical spectroscopy is based on the observation of the change in the dielectric function after a pump pulse. One can either probed one wavelength or a broader range. The first time-resolved reflectivity measurement was done by Von der Linde et al. and Alfano et al. in 1971 [194, 1]. Since then, the

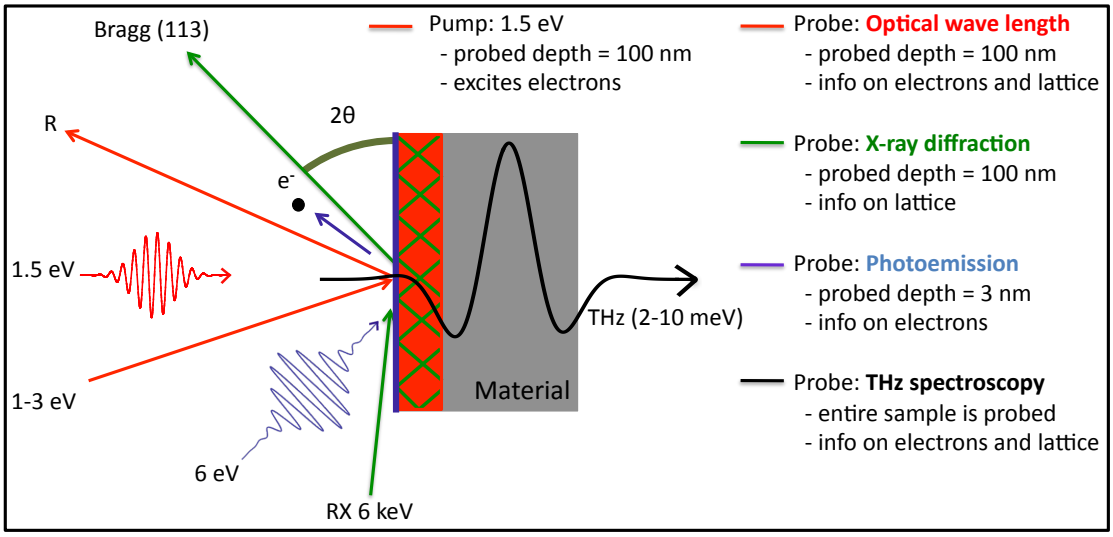

Fig. 3.2: Scheme of the different pumps and probes used in this work. The pump is always a 1.5 eV laser pulse. The probes are optical reflectivity, THz spectroscopy, X-ray diffraction, and photoemission spectroscopy.

domain has grown and probes ranging from the entire visible spectrum to the THz spectrum can be used. Single color time-resolved reflectivity is ideal to probe coherent phonons and relaxation times because of its very good signal to noise ratio. Whereas white light spectroscopy offers a broader view of the dielectric function [140] and THz spectroscopy probes almost the DC conductivity [15].

3.2.1 Single color reflectivity

3.2.1.1 Detecting relaxation times and phonons

Single color time-resolved reflectivity is used to observe the transient change in reflectivity at a certain wavelength. A pump pulse excites the system and a monochromatic probe pulse is reflected after a controllable delay. Fig.3.3 shows a typical transient response of a material in terms of $\Delta R/R$. The different relaxation times can be allocated to different degrees of freedom, electron scattering, phonons, spins, or diffusion through the sample. Their assignment is done by varying the temperature, fluence, pump and probe polarization, and etc. On top of this decay, an oscillatory signal can be seen which is due to optical coherent phonons. The phonons are said to be coherent when they oscillate in phase. Two theories exist to explain the excitation of coherent phonons, Impulsive Stimulated Raman Scattering (ISRS) and Displacing Excitation of Coherent Phonons (DECP). I will very briefly explain both theories.

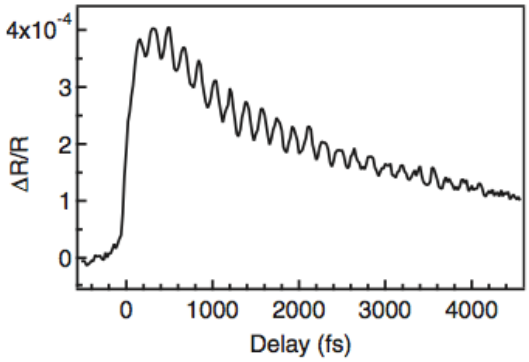

Fig. 3.3: Typical time-resolved reflectivity trace(from [116])

Let us consider the general equation of motion of an atom that is projected along a normal coordinate q [123]:

$$\frac{d^2q}{dt^2} + 2\gamma\frac{dq}{dt} + \omega_0^2 q = \frac{F(t)}{m} \tag{3.1}$$

where ω_0 is the phonon frequency, γ the damping constant, m the mass of the atom, and $F(t)$ the driving force. The ISRS and DECP theories diverge on the underlying mechanism of the driving force. Since the femtosecond laser pulse has a large bandwidth, the difference between frequencies inside the pulse can be the frequency of a phonon. Therefore the laser pulse can stimulate Raman scattering. The ISRS theory uses this to explain the excitation of phonons and supposes that the polarisability of the material α depends on the inter-atomic distance and therefore q. The driving force can be written as [206, 194, 1]:

$$F(t) = \frac{1}{2}N\left(\frac{\partial\alpha}{\partial q}\right)_0 : \mathbf{E}^2(z,t) \tag{3.2}$$

where N is the density of excited oscillator, and $\mathbf{E}$ the electric field. The DECP theory supposes that the laser pulse creates a sudden change in the electronic temperature and in the density of electron in the conduction band, that results in a sudden change of the equilibrium position that starts the oscillatory movement. If the force is due to the sudden change of conducting electrons one can write [214]:

$$F(t) \propto \omega_0^2 j(t) \tag{3.3}$$

where $j(t)$ is the density of conduction electrons. q can be linked to $\Delta R/R$ with the following equation [214, 26]:

$$\frac{\Delta R}{R}(t) = A_e T_e(t) + A_L T_L(t) + A_{ph} q(t) \tag{3.4}$$

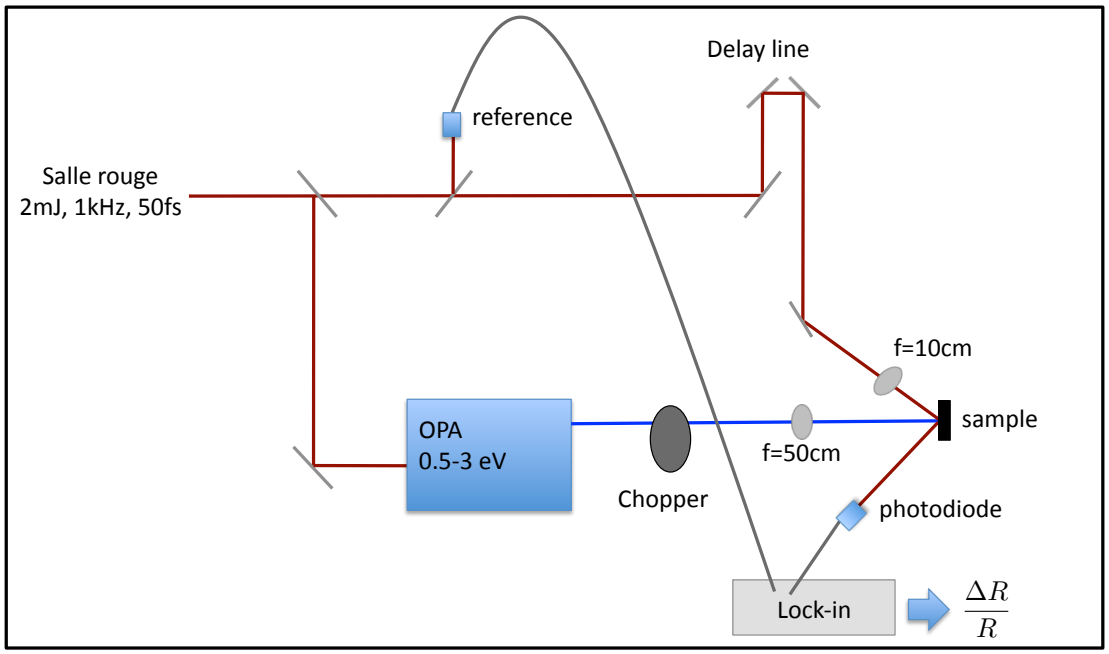

Fig. 3.4: Time-resolved single color reflectivity experimental setup

where A_e, A_L, and A_{ph} are constants, T_e and T_L are respectively the electronic and the lattice temperature. The two theories are similar in that they explain the observation of the coherent phonon by an abrupt change in either the polarisability or by a change of equilibrium atomic position, DECP can be viewed at a simplified case of ISRS. The frequency of the phonon is key because it gives an insight on the lattice structure at the femtosecond timescale.

3.2.1.2 Experimental setup

I will describe the setup of the Salle Bordeaux in LOA. The in house laser system delivers a 35 fs, 10 mJ, 800 nm (1.5 eV) laser pulse with a repetition rate of 1 kHz. Fig.3.4 shows the experimental setup for the time-resolved single color reflectivity experiment. The laser pulse is separated into a probe and a pump pulse. The pump pulse goes directly to the sample or is used to generate another wavelength with an Optical Parametric Amplifier (OPA). The probe is directly sent to the sample and its reflection is detected by a slow photodiode. The probe spot size is always kept much smaller than the pump spot size. The pump pulse is either filtered out using a filter if the wavelength is different from the probe or crossed polarized with a polarizer in front of the photodiode.

The most crucial part of the setup is the detection system. The pump is chopped at 500 Hz in order to have one of two probe pulses that detects the excited material.

To compensate the long fluctuation, part of the probe beam is used as a reference and a lock-in amplifier at 500 Hz is used to detect the difference between the signal and the reference. The output of the lock-in is directly $\Delta R/R$. This technique is able to obtain a signal to noise ratio of 5 10^8 which is close to the shot noise limit[25].

3.2.2 White light reflectivity

3.2.2.1 Optical spectroscopy

The idea behind time-resolved white light spectroscopy is to track in real time the optical conductivity at all frequency. Fig.3.5 shows the density of state of a correlated metal and a Mott insulator with its respective optical conductivity. With the optical conductivity one can retrieve the Coulomb repulsion and the electronic bandwidth. However the experimental observable is usually not directly the optical conductivity $\sigma(\omega)$ but the reflectivity $R(\omega)$ which is the amplitude of the complex reflectivity $\sqrt{R(\omega)}e^{i\rho(\omega)}$. The causality relation links the real and imaginary part of a causal response function. This relationship is given by the Kramer-Kronig relation [203] :

$$\Re eG(\omega) = \frac{1}{\pi}\wp \int_{-\inf}^{\inf} \frac{\Im mG(\omega)}{\omega' - \omega} d\omega' \tag{3.5}$$

$$\Im mG(\omega) = -\frac{1}{\pi}\wp \int_{-\inf}^{\inf} \frac{\Re mG(\omega)}{\omega' - \omega} d\omega' \tag{3.6}$$

where $\wp$ is Cauchy's principal value. With this relation we can recover the phase of the reflectivity and write the real and imaginary part of the dielectric constant $\epsilon_1(\omega)$, $\epsilon_2(\omega)$ [203] :

$$\epsilon_1(\omega) = \frac{(1 - R(\omega))^2 - 4R(\omega)sin^2\rho(\omega)}{1 + R(\omega) - 2\sqrt{R(\omega)}cos^2\rho(\omega)} \tag{3.7}$$

$$\epsilon_2(\omega) = \frac{4(1 - R(\omega))\sqrt{R(\omega)}sin\rho(\omega)}{1 + R(\omega) - 2\sqrt{R(\omega)}cos^2\rho(\omega)} \tag{3.8}$$

The relationship between the real part of the optical conductivity and the dielectric function is $\sigma_1(\omega) = \omega\epsilon_2(\omega)/4\pi$.

The most difficult part of this analysis method is recovering the phase of the reflectivity because in order to apply the Kramer-Kronig relations one has to consider the values for all the frequencies which is experimentally very hard. To circumvent this problem, we use the property that the integral over all frequencies is a conserved quantity for optical properties of material since the total charge

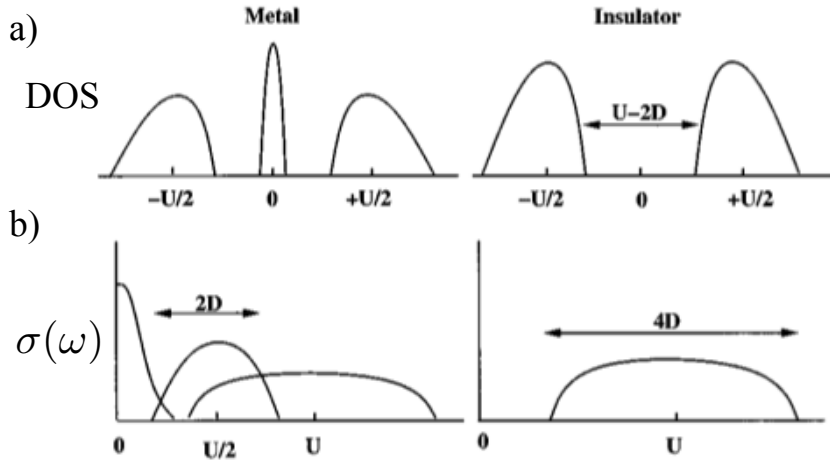

Fig. 3.5: a) Density Of States (DOS) for a correlated metal and a Mott insulator b) Optical conductivity for the DOS from a). The metallic and the insulating state can be clearly identified with their optical conductivity probed by spectroscopic techniques (from [163]

is conserved. This leads to different sum rules that can be found in [203, 13]. Time-resolved reflectivity is the same as time-resolved single color reflectivity but looking at all the frequency. All the mechanisms described in section 3.2.1 are still valid however a more spectroscopic analysis can be done.

3.2.2.2 Experimental setup

I will describe the experiment situated in the T-Rex Laboratory at Elettra (Italy).The experimental setup, shown in Fig.3.6, is very similar to single color reflectivity setup. The laser is a Ti:Sapphire that delivers a 800 nm (1.5 eV), 5 μJ, 80 fs pulse at a repetition rate of 250 kHz. The probe pulse is focalized in a Sapphire crystal and produces a super continuum pulse between 1.2 and 3 eV. The pulse is then focalized on the sample and then dispersed with a prism on a photodiode array; a reference is extract before the sample. The pump pulse is chopped at 2 kHz in order for the probe pulse to detect the material with the pump and without the pump. A parity detector records when the pump is passing through. Fast electronics compare the difference between pump on and pump off. The output signal is $\Delta R(\omega)/R(\omega)$ for frequency between 1.2 and 3 eV.

Time-resolved optical reflectivity is a powerful method to track properties of materials. However the range probed has to contain spectroscopic information like a Hubbard exciton [140]. If no real spectroscopic features are present in the region, the analysis will not give any useful information. Therefore other regions of the

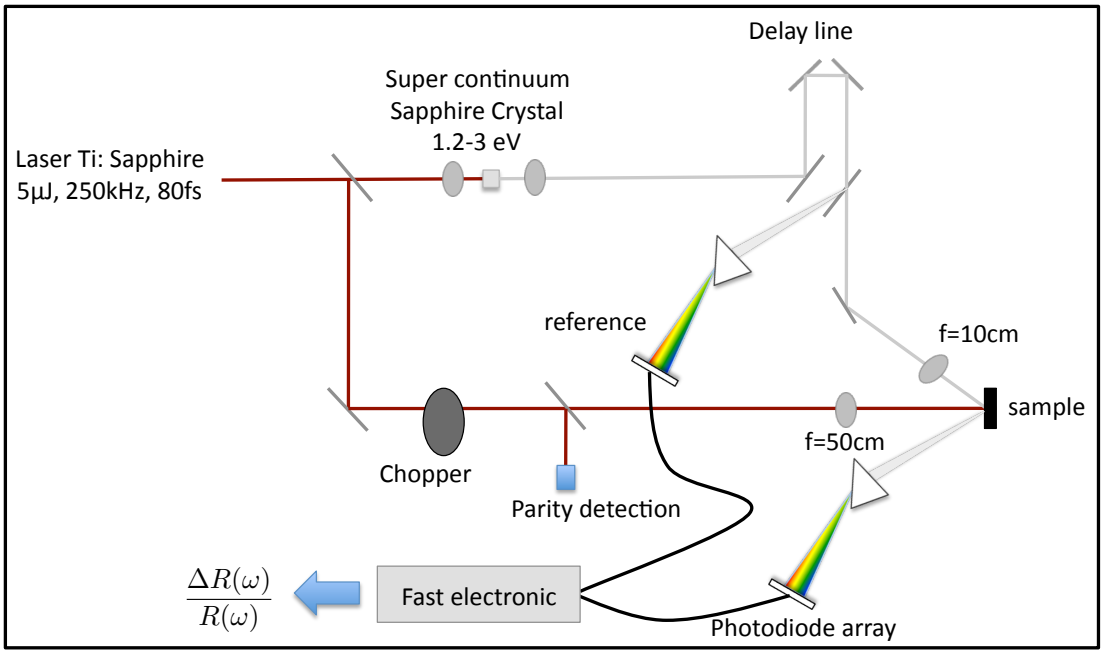

Fig. 3.6: White light setup

optical conductivity have to be probed as for example in the THz region.

3.2.3 THz spectroscopy

3.2.3.1 THz time domain spectroscopy

The THz region is the electromagnetic spectrum between 0.4 meV (0.1THz) and 125 meV (30 THz). These energies probe very close to the gap and can well distinguish between an insulator and a metal, as seen in the optical conductivity in Fig.3.5. This region is also where collective modes lie for example phonons, magnons or even Josephson plasma modes [87]. These modes create absorption or emission peaks in the THz region and can be tracked while the material is photoexcited. In our case we are mainly interested in the broadband response which is an information on the gap of the material. Time domain spectroscopy consists of recording in time a THz pulse which is composed of different frequencies. The Fourier transform will give the amplitude and the phase for each frequency. We can derive the loss function $Loss(\omega)$ from the Fourier transform of the transmitted signal:

$$Loss(\omega) = -ln\left(\left|\frac{T(\omega)}{T_{ref}(\omega)}\right|\right) \tag{3.9}$$

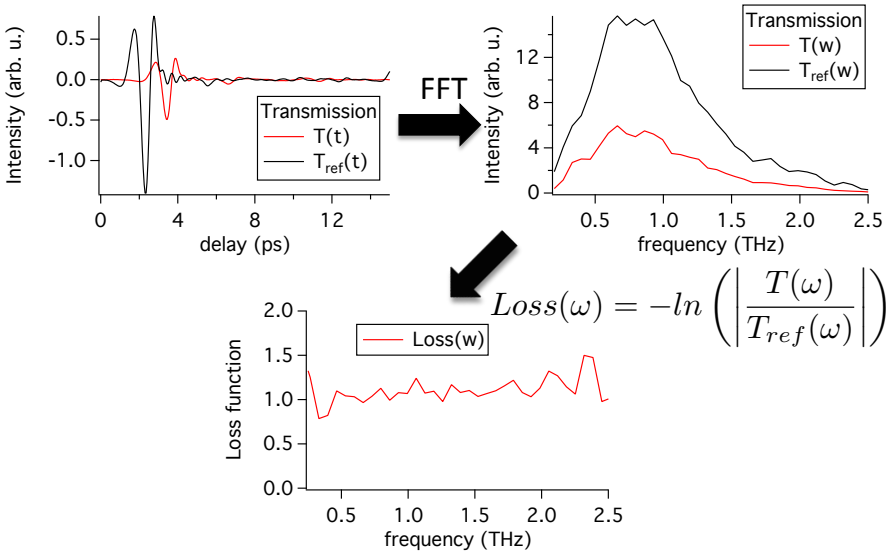

Fig. 3.7: Step to calculate the loss function.

where $T(\omega)$ is the Fourier transform of the time domain THz signal transmitted through the sample and $T_{ref}(\omega)$ is the reference spectrum. The Loss function is a measure of the absorption for each frequency. If this quantity is flat, it is a signature of the Drude response in the case of a metal or the gap in the case of an insulator. If this quantity presents features, these can be assign to certain collective modes.

Fig.3.7 shows the procedure to calculate the loss function. For time-resolved measurements, the whole THz pulse should be resolved for each delay, thus a 2D scan should be performed. If the spectrum contains resonances the 2D scan is very important because the resonances can move and create changes in the phase of certain frequencies [15]. Only monitoring the THz pulse peak intensity will not allow the whole spectral information to be retrieve, since the phase can vary. However if the spectrum is flat which reflects the broadband response, one can sit on the peak of the THz signal and only change the pump delay. This supposes that all the frequencies change with the same amplitude and their phases do not change. This hypothesis should be carefully verified by performing a resolving the THz pulse for a few pump delays, in order to ensure that the phase does not change.

3.2.3.2 Experimental setup

The THz spectroscopy experiments in this thesis were performed in Radboud University in Nijmegen (The Netherlands). Fig.3.8 shows the experimental setup.

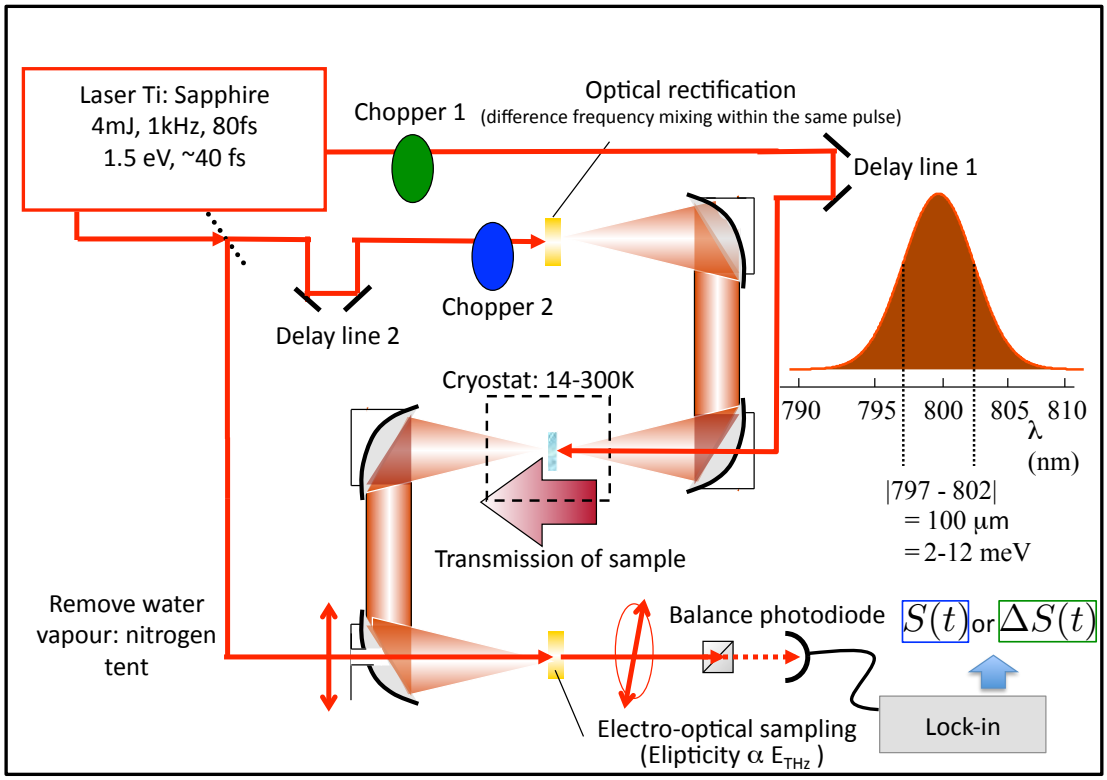

Fig. 3.8: THz time domain spectroscopy setup

The Laser was a Ti:sapphire at 1 kHz repetition rate with a 4 mJ pulse of 40 fs duration centered at 1.55 eV. The beam was split into 3 pulses, a pulse to generate THz waves in a ZnTe crystal, a probe pulse to perform the electro-optical sampling to record the transmitted THz pulse, and a pump pulse to excite the material. The electro-optical sampling is a THz detection method where the 800 nm pulse and the THz pulse are focalized in a ZnTe crystal. The THz electric field changes the polarization of the 800 nm light, which is then detected using a balance detector. The THz pulse and the pump pulse are focused on the sample illuminating it entirely. The entire THz generation and the detection are done under nitrogen flux to avoid water absorption.

To perform equilibrium time domain spectroscopy, chopper two should be turn on and the pump pulse turn off. By varying the delay line 2, the THz pulse is detected using electro-optical sampling with a lock-in amplifier at the frequency of chopper 2 rendering the transmitted signal as shown in Fig.3.7. To perform the 2D scan, one should turn on chopper one and off chopper two, for each delay 1 the entire THz pulse should be detected by varying delay 2. To look at the broadband response, delay 2 can be set to the maximum of the THz pulse.

These spectroscopic techniques are very powerful but since they probe optical transitions (white light spectroscopy) or free carriers (THz spectroscopy) their interpretation changes when the system is out-of-equilibrium. For example silicon at equilibrium is transparent for THz frequencies therefore one can infer that there is a gap. When free carriers are excited to the conduction band using a pump pulse, the free carriers in the conduction band and valence band block the THz pulse but the gap is still present. The THz pulse is absorbed by the electrons in the conduction band as well as the holes in the valence band. Therefore in a Mott insulator THz spectroscopy can not differentiate between a collapse of the gap or the excitation of free carriers. Time-resolved X-ray diffraction and time-resolved ARPES provided a more direct visualization of the lattice and band structure of the out-of-equilibrium material.

3.3 Time-resolved X-ray diffraction

X-ray diffraction is the fundamental method that enables the resolution of crystal structures. The technique probes directly the periodicity of the lattice and is the keystone of all condensed matter physics. In 1895, X-rays were discovered by Röntgen in Würzburg (Germany) and in 1912 Von Laue, Friedrich, and Knipping did the first diffraction experiment with X-rays [153]. In 1913, the Braggs, father and son, gave the first interpretation of the diffraction patterns using lattice planes. Since 1912, X-ray were produced using X-ray tubes then, in 1970, synchrotron radiation was used [153].
In this section, I will first present standard X-ray diffraction than a brief presentation on synchrotron radiation. And finally I will present the time-resolved version of X-ray diffraction.

3.3.1 X-ray diffraction

When X-rays hit a crystal, light is diffracted only in certain directions. The Braggs, father and son, explained this in their 1913 paper [28] or in the son's Nobel prize speech in 1922 [28, 29], (they received the noble prize 1915 but could not go because of the war). The Bragg law is as follow:

$$2d_{h,k,l}sin(\theta) = n\lambda \tag{3.10}$$

where d is the distance between two lattice planes, θ is the angle between the incident beam and the plane, $n\lambda$ is n times the incident wavelength. Fig.3.9 shows the vector version of the Bragg law that can be written as [199]:

$$\vec{k_d} - \vec{k_i} = \vec{q}_{h,k,l} = h.\vec{a^*} + k.\vec{b^*} + l.\vec{c^*} \tag{3.11}$$

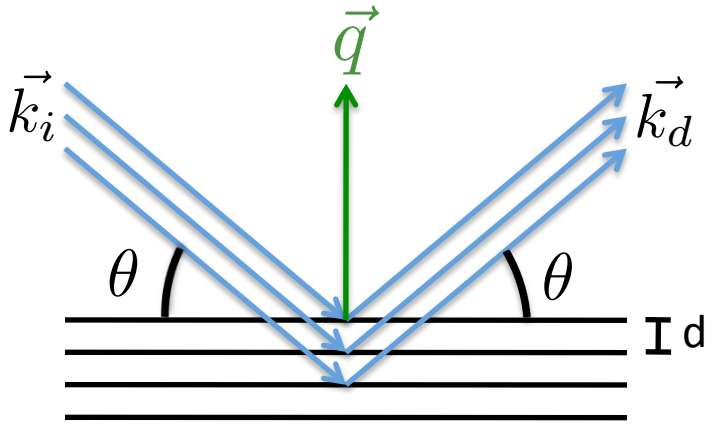

Fig. 3.9: Vector version of Bragg's law.

where $\vec{k_i}$ the incident beam wave vector, $\vec{k_d}$ the diffracted beam wave vector,$\vec{q}_{h,k,l}$ is the direction in the reciprocal space of the plane observed with the Miller indexes h, k, and l. In order to be in diffraction condition, the reciprocal direction has to be the bisector of the incident and diffracted beams and have its norm equal to the norm of the difference between the vector of the two beams.

A geometric interpretation of the diffraction conditions was proposed by Ewald [61], shown in Fig.3.10. The crystal is placed in the center of the Ewald sphere of radius $2\pi/\lambda$. The incident beam is horizontal going from the left part of the circle to the middle and the refracted beam has its origin at the center. The origin of the reciprocal space is O, when a spot touches the Ewald sphere the direction observed is the vector going from O to the spot and the refracted beam goes from the center to the spot.

In order to calculate the distance between two planes, it is easier to use the norm of the reciprocal vector $\vec{q}_{h,k,l}$ which is perpendicular to the hkl-planes [199]. We have $d_{h,k,l} = 2\pi/|\vec{q}_{h,k,l}|$. The reciprocal vector are:

$$\vec{a^*} = 2\pi\frac{\vec{b}\wedge\vec{c}}{v},\ \vec{b^*} = 2\pi\frac{\vec{c}\wedge\vec{a}}{v},\ \vec{c^*} = 2\pi\frac{\vec{a}\wedge\vec{b}}{v} \tag{3.12}$$

where v is the unit cell volume. In experiments, the monocrystal is placed at the center of rotation of a diffractometer with several rotations and the detector has also several rotations. One can project the crystal's axes on the difffractometer's axes and construct the orientation matrix. In this thesis I use the angle convention described in [33]. The Bragg diffraction conditions can be rewritten:

$$(\prod_i S_i).UB.\vec{h} = (\prod_j D_j - Id).\vec{k_i} \tag{3.13}$$

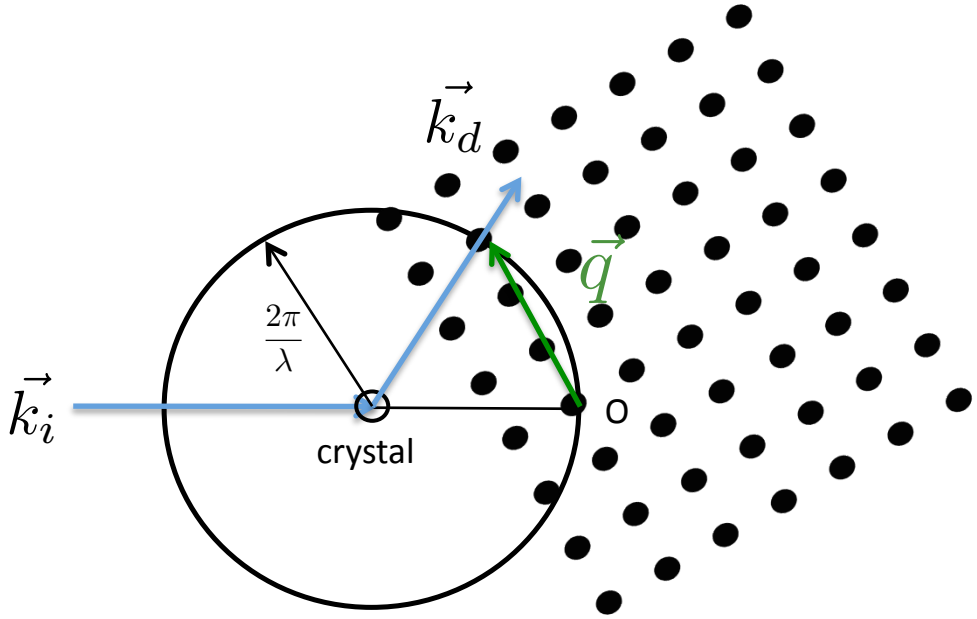

Fig. 3.10: Ewald's sphere

Where S_i are the rotation matrix of the sample, $k\omega$, κ, $k\phi$, UB is the orientation matrix of the sample, $\vec{h}$ the vector h,k,l and D_j the rotation matrix for the detector δ, $\_\gamma$. The conditions for a direction to cut the Ewald sphere are:

$$\|R.UB.\vec{h} + \vec{k_i}\| = \frac{2\pi}{\lambda} \tag{3.14}$$

In the Bragg conditions, the intensity of the Bragg reflection for one type of atom can be written as:

$$I(q_{\vec{h,k,l}})(t) \propto \|F(t)\|^2 e^{-2W(t)} \tag{3.15}$$

where F is the norm of the structure factor and e^{-2W} the Debye-Waller factor. The time dependence show that the atomic position can vary according to the pump-probe delay. The structure factor is the discrete Fourier transform of the positions of the atoms in the unit cell. These positions are given by the Wyckoff positions, they can be found for each space group on the Bilbao crystallographic Server [9]. The structure factor is:

$$F(q_{\vec{h,k,l}})(t) = \sum_j f_j e^{-2i\pi(hx_j(t)+ky_j(t)+lz_j(t))} \tag{3.16}$$

where j is the atom in the unit cell, f_j its atomic diffusion factor, and x_j, y_j, z_j its position in the unit cell. The structure factor is important in order to detect displacement inside the unit cell, for example phonons in Bismuth [95]. Note that Bismuth is the test bed for observing coherent phonons with new techniques, as time-resolved X-ray diffraction [94], time-resolved optical reflectivity [24], or time-resolved ARPES [62]. The second term that acts on the intensity of the Bragg peak is the Debye-Waller factor :

$$W(t) = 1/2\langle(\vec{q_{h,k,l}} \cdot \vec{u_n}(t))^2\rangle \tag{3.17}$$

where $\vec{u_n}$ is the second moment of the atomic distribution. This quantity is linked to thermal excitation of the crystal. A theory based on dynamical diffraction has been applied to time-resolved experiments by P. Sondhauss and J. Wark [182] but this theory supposes perfect crystals which is not the case with our samples. Nowadays, most detailed crystal structures are refined using Synchrotron radiation described in the next section.

3.3.2 Synchrotron radiation

When a charge particle is accelerated radially it emits an electromagnetic radiation called synchrotron radiation. This radiation was first observed by Iwanenko and Pomeranchuk in 1944 [92] but formalized in 1947 by Elder, Gurewitsch, Langmuir, and Pollock [57]. Synchrotron radiation was first viewed as a parasite phenomenon because the main research was done for particle physics. Only in 1968 was an accelerator built to maximize the synchrotron radiation. The Synchrotron Radiation Center (SRC), located in Stoughton Wisconsin, operated the first dedicated storage ring, Tantalus, that was designed by Ed Rowe [162]. Over 30 synchrotrons exist today and many are third generation, which means that the synchrotron radiation is produced using either bending magnets or insertion devices. The light that is emitted is extremely bright and can attain the brightness of 10^{20} photons/s/mm^2/mrad^2/0.1% bandwidth, which is about 10^{14} higher than X-ray tubes. Besides the advantage of being brighter than X-ray tubes, synchrotron radiation is tunable in wavelengths. The light emitted covers the entire spectral range from infrared to hard X-rays, which is an advantage compared to lasers that only work at specific wavelength. Synchrotron radiation is used in many research area such as material science or even protein crystallography because the light is extremely bright and tunable especially in the X-ray region.

Fig.3.11.a) shows a scheme of a synchrotron center. 1. The electrons are produced and accelerated in the LINAC, 2. They are then accelerated in the Booster, 3. They attain 0.99% of the speed of light and are stored in the storage ring. 4. is a bending magnet, 5. is a quadrupole to keep the electron bunch collimated, 6. is an

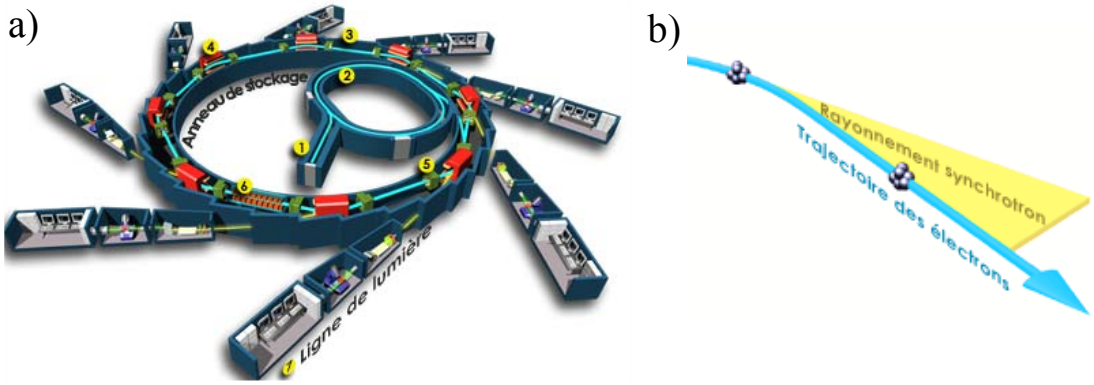

Fig. 3.11: a) Synchrotron laboratory b) Synchrotron radiation

insertion device called an ondulator, which is an alternation of dipoles that make the electron bunch oscillate to produce even brighter light. 7. is a beam line that uses the synchrotron radiation. A beam line usually consists of a monochromator that selects one specific wavelength, mirrors to focus the light on the sample, slits to stop the unwanted light, and an end station to perform the experiment.
In this thesis, I will present work done on the beamlines: Cristal, and Cassiopée at the Synchrotron SOLEIL (France), Badelph at Synchrotron Elettra (Italy), Beamline 6.0.1 in ALS (USA). I performed different types of photoemission spectroscopy and time-resolved diffraction experiments.

3.3.3 Time-resolved X-ray diffraction

Time-resolved diffraction is the time-resolved version of the equilibrium technique. Using the time structure of the synchrotron, the first nanosecond experiment was done by Larson et al. in 1982 [107]. The best time resolution achievable today is 10 ps [191]. In many cases this is not good enough to really observe the the fast electron or atomic dynamics that arise during the first picosecond. Achieving better time resolution is very challenging. The first subpicosecond X-ray pulse was produced using the Kα from a plasma generated by a femtosecond laser [160, 161]: this approach produces very few photons, is not very stable, and it is not continuously tunable in wavelength. The other technique to produce subpicosecond pulses was developed by Schoenlein et al. It consists of slicing part of the picosecond electron bunch in a synchrotron storage ring using the interaction between a femtosecond laser pulse and the electron bunch in an insertion device[176, 175]. The photon flux is also very small but tunable in wavelength. The only high flux femtosecond X-ray pulse is produced by Free Electron Lasers (FEL) that deliver 2 10^{12} photons per pulse with a time duration shorter than 80

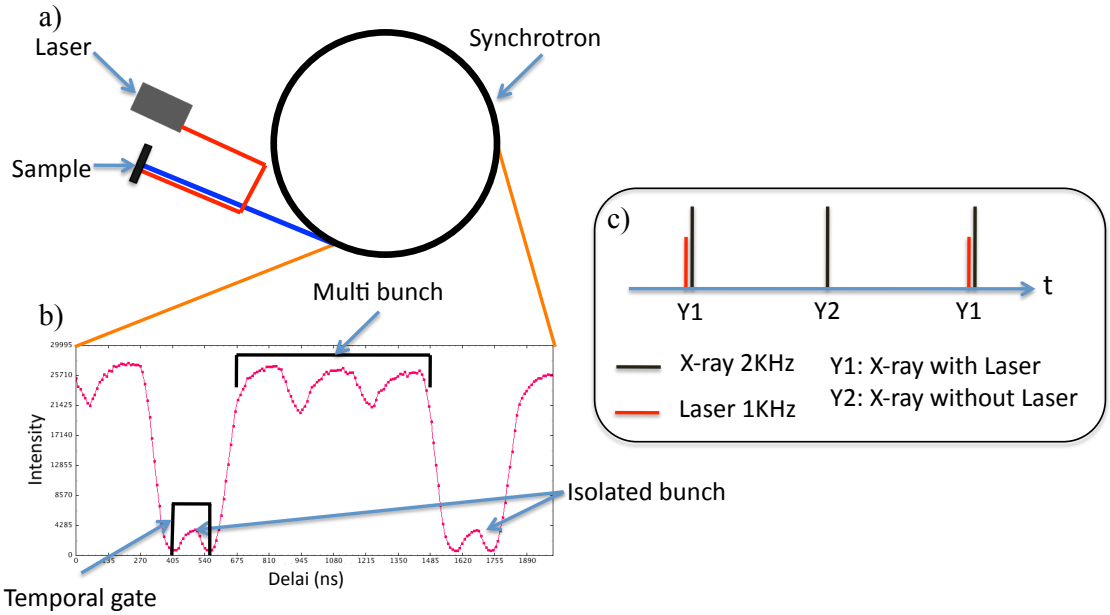

Fig. 3.12: a) Diagram of the synchrotron with a synchronized laser system b) Time structure of the synchrotron hybrid filling mode, an isolated electron bunch can be gated using a boxcar c) acquisition scheme, one out of two X-ray pulse is pumped in order to have an unpumped reference.

fs. During the course of my thesis we weren't able to gain access to any femtosecond X-ray sources. Therefore I will only present work done with the time structure of the synchrotron, which gives a resolution of 100 ps. The experiments were done at the beamline 6.0.1 at ALS and at beamline Cristal at SOLEIL.

Fig.3.12.a) shows a diagram of the synchrotron with synchronized laser. The laser is usually in a hutch next to the X-ray hutch and the laser beam is transported to the sample that is placed at the center of rotation of the diffractometer. Fig.3.12.b) shows the time structure of the hybrid filling mode of the synchrotron. A single electron bunch is isolated from the multibunch part to enable the temporal gating. A boxcar is used to temporally gate the detector on the isolated bunch in order to observe only the signal coming from it. The X-ray acquisition repetition rate is 2 kHz while the laser's is 1 kHz as shown in Fig.3.12.c). The direct comparison between the X-ray pulse with the laser pulse and the one without it makes it possible to compensate the rapid X-ray fluctuations. The laser is triggered with the synchrotron RF signal to insure a minimum jitter. The delay is controlled either electronically or with a delay line. The two crucial settings are the spatial and temporal overlap. The zero delay is done roughly with a fast photodiode, and the spatial overlap is done using a fluorescent paper and the laser spot is kept large

to ensure a homogeneous excitation. No 2D detector exists with a acquisition rate of 2 kHz therefore only Avalanche Photodiodes (APD) can be used. The crystal is oriented using a 2D detector and the time-resolved measurements are done with an APD. The APD is fairly large therefore it integrates over a large portion of the Ewald sphere. The precise 2θ value of the Bragg reflection can therefore not be observe. The only equation that can be used is then equation 3.14 because the detector angles are unknown. A shift in the rocking curve angle will translate to a change of lattice parameters. A change of intensity is either due to a change of the Debye-Waller factor or due to a change of structure factor.

The penetration length between the laser and the X-rays is usually very different therefore the X-ray beam has to be in a grazing condition and the laser in normal incidence to compensate this difference. In order to detect a Bragg peak in grazing incidence, the angle between the surface direction and the observed one has to be larger than the angle θ from Bragg's law. Therefore not all Bragg reflection can be measured in grazing incidence. Time-resolved X-ray diffraction is a very powerful technique to track the change in a crystal structure but is very difficult to perform experimentally.

3.4 Angle resolved photoelectron spectroscopy

When photons with sufficiently high energy hit a material, electrons are ejected from its surface. This effect was first observed by Hertz in 1887 [85]. It was later explained theoretically by Einstein in a paper of 1905 [56], for which he received his Nobel prize in 1921. These ejected electrons contain a lot of information on the electronic structure of the material. Analyzing their kinetic energy and direction enables one to recover the binding energy and the momentum of the electrons before their emission. In 1957, the Swedish scientist Kai Siegbahn was the first one to turn this effect into a real spectroscopic method, called photoemission, by using X-rays to study the binding energy of electrons [137]. He received a Nobel prize in 1981 for his work. David W. Turner did the same using UV light in 1961 [192]. The technique has since then gained precision especially with the use of synchrotron radiation, (the energy resolution can be better than 2 meV and the angular resolution better than 0.2° [47, 46]), and is now called Angle Resolved Photoelectron Spectroscopy (ARPES). The limitation today is the limited energy resolution and the surface sensitivity. To tackle the first problem scientists are exploring the use of lasers to obtain a perfect monochromatic light, as good as 70μeV [141, 142]. The second limitation is being solved by using higher energy X-ray photons which are more bulk sensitive, this technique is called Hard X-ray Photoelectron Spectroscopy (HAXPES).

I will first present the fundamental principle of ARPES in 3.4 and then present

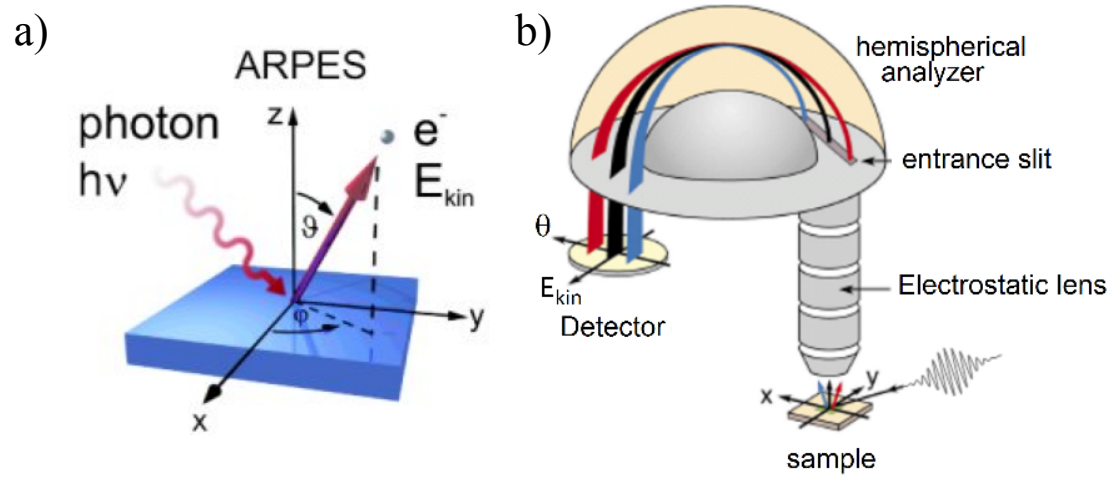

Fig. 3.13: a) Geometry of the emission of the photoelectron. b) representation of the photoelectron detector (from [46])

its time-resolved version in 3.5.

3.4.1 Fundamental principle

The experimental quantities observed in ARPES are the emission angle and the kinetic energy of the electron. Fig.3.13.a shows the geometry of the photoelectron detection, the angles θ and φ characterize the emission angle and the energy of the electron is E_{kin}. Fig.3.13.b represents the detector which is usually a hemispherical analyzer. The electrostatic lens collects the photoelectrons. They then pass through the entrance slit which will select only one φ angle and cut the others. The hemispherical analyzer will disperse the photoelectrons in energy in order to detect them on a 2D detector the θ angle along one direction and the kinetic energy along the other. Since this technique only allows one φ angle to be detected, the sample has to be rotated around its surface's normal to obtain all the photoelectron directions. The entire experiment has to be done under ultra high vacuum (UHV) in order for the electron to propagate in vacuum and keep the surface clean.

Each detected photoelectron carries information on its initial state before being ejected from the material. We can recover it using energy and momentum conservation rules, that are given by:

$$E_f - E_i = h\nu \tag{3.18}$$

$$\vec{k}_f - \vec{k}_i = \vec{k}_{h\nu} \tag{3.19}$$

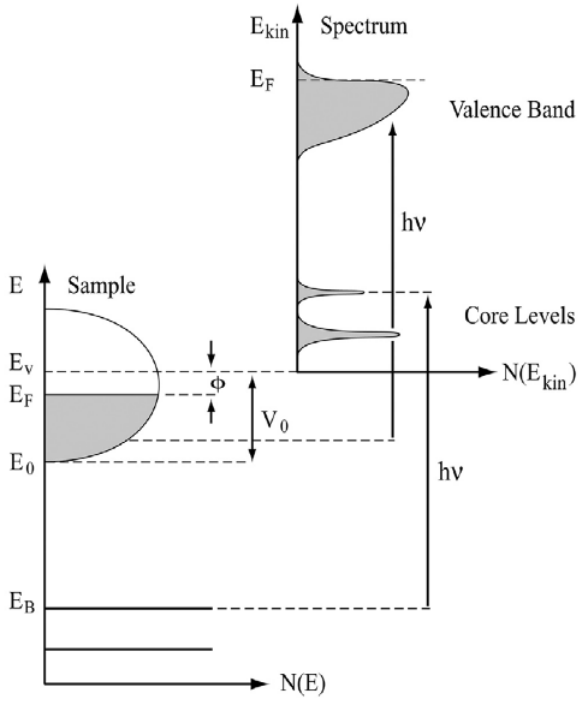

Fig. 3.14: Conservation laws for the photoelectron process (from [46]).

where E is the energy, k the momentum, the indexes i and f refer to the initial and final state. Note the importance of having a monochromatic light to define uniquely the initial electron state. For low energy photons, their momentum can be neglected. Equation 3.18 can be rewritten in terms of binding energy and equation 3.19 by using the momentum of a electron in vacuum $K = p/\hbar$:

$$E_{kin} = h\nu - \phi - E_B \tag{3.20}$$

$$K_x = \frac{1}{\hbar}\sqrt{2mE_{kin}}sin(\theta)cos(\varphi) \tag{3.21}$$

$$K_y = \frac{1}{\hbar}\sqrt{2mE_{kin}}sin(\theta)sin(\varphi) \tag{3.22}$$

$$K_z = \frac{1}{\hbar}\sqrt{2mE_{kin}}cos(\theta) \tag{3.23}$$

where E_B is the binding energy, ϕ is the work function of the material which corresponds to the energy between the Fermi energy (E_F) and the vacuum level as depicted in Fig.3.14.

In order to get more insight on the momentum of the electron in the solid, one has to consider the three step model to describe the photoemission process:

1) excitation to a bulk final state
2) transport to the surface
3) transmission through the surface

The first two steps do not break any symmetry but the last one does. The symmetry is broken along the z direction therefore we can separate K into two components the first which is conserved $K_{\parallel} = K_x + K_y = k_{\parallel}$ along the surface and the second one perpendicular to the surface $K_{\perp} \neq k_{\perp}$ which is not conserved because of the abrupt change along the z direction, k refers to the initial momentum and K the final one. We introduce the surface potential V_0 to account for the extra source of the momentum at the surface. We can rewrite $k_{\parallel}$ and $k_{\perp}$ as follows:

$$k_{\parallel} = \frac{1}{\hbar}\sqrt{2mE_{kin}}sin(\theta) \tag{3.24}$$

$$k_{\perp} = \frac{1}{\hbar}\sqrt{2m(E_{kin}cos^2(\theta) + V_0)} \tag{3.25}$$

The surface potential V_0 is usually unknown therefore the most used method is to vary the photon energy to detect the periodicity along $k_{\perp}$. We used this technique for the compound $BaNiS_2$ [170]. These relations are very useful to retrieve the band structure of the material but the first process in the three step model has an effect on the intensity observed and can add some more information.

3.4.2 Photoemission intensity

The photoemission intensity can be calculated using the three step model described above. The first step is the optical excitation of an electron in the N-electron ground state. The interaction can be treated as a pertubation, Fermi's golden rule gives:

$$w_{i,f} = \frac{2\pi}{\hbar}|\langle\psi_f^N|H_{int}|\psi_i^N\rangle|^2\delta(E_f^N - E_i^N - h\nu) \tag{3.26}$$

$$H_{int} = \frac{e}{2mc}(\mathbf{A}\cdot\mathbf{p} + \mathbf{p}\cdot\mathbf{A}) = \frac{e}{mc}\mathbf{A}\cdot\mathbf{p} \tag{3.27}$$

where $|\psi_f^N\rangle$ and $|\psi_i^N\rangle$ are respectively the final and initial wave function of the N-particle system, $\mathbf{p}$ is the momentum operator and $\mathbf{A}$ the electromagnetic vector potential, the interaction is written using the dipole approximation. The excited electron leaves the system therefore the final state actually has N-1 particles. We can described this using the one-particle spectral function that accounts for the subtraction or addition of one particle to a N-particle system:

$$A(\mathbf{k},\omega) = A^+(\mathbf{k},\omega) + A^-(\mathbf{k},\omega) = -(1/\pi)ImG(\mathbf{k},\omega) \tag{3.28}$$

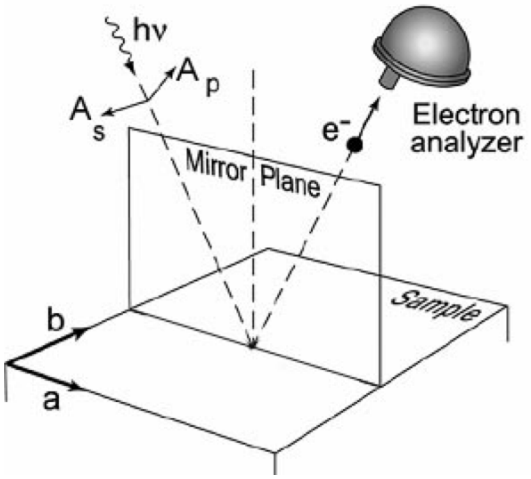

Fig. 3.15: Polarization dependence of ARPES intensity. The mirror plane contains the surface's normal, the incident beam, and the emitted electron. The polarization s and p are respectively in plane and out of plane (from [46]).

$$A^{\pm}(\mathbf{k},\omega) = \sum_m |\langle \psi_m^{N\pm1} | c_k^{\pm} | \psi_i^N \rangle|^2 \delta(\omega - E_m^{N\pm1} + E_i^N) \tag{3.29}$$

where $A^{\pm}(\mathbf{k},\omega)$ is the partial spectral function for addition or substraction of one particle, $A(\mathbf{k},\omega)$ is probed by ARPES. The index m is for the excited state; $c_k^{\pm}$ creates (or annihilates) an electron with energy ω, momentum k, and spin σ in the N-particle initial state ψ_i^N. We can then write the total measured intensity as:

$$I(\mathbf{k},\omega) = I_0(\mathbf{k},\omega,\mathbf{A}) f(\omega) A(\mathbf{k},\omega) \tag{3.30}$$

where $f(\omega)$ is the Fermi function, and $I_0(\mathbf{k},\omega,\mathbf{A})$ is proportional to the square of the one electron matrix element defined in equation 3.26. This matrix element depends strongly on the momentum and electron energy ,the photon energy, and its polarization. The latter can give insight on the symmetry of the probed orbitals.

Fig.3.15 shows the geometry of an ARPES setup. We will only consider the electron emitted from the mirror plane. The matrix element is defined as $|\mathbf{M}_{f,i}^k|^2 = |\langle \phi_f^k | \varepsilon \cdot \mathbf{x} | \phi_i^k \rangle|^2$, where ε is the unit vector along the polarization direction of $\mathbf{A}$ and $\mathbf{x}$ is the electronic position. The integration of the function is done perpendicular to the mirror plane. Therefore the function has to be even under the reflection with the mirror plane to be different from zero. The detected electron is the final state, which is a plane wave state $e^{i\mathbf{k}r}$ with its momentum in the mirror plane thus its symmetry is even under the reflection with the mirror plane. Therefore $\varepsilon \cdot \mathbf{x} | \phi_i^k \rangle$ has to be even in order for the whole function to be even. If the initial state is odd then $\varepsilon \cdot \mathbf{x}$ has to be odd (the polarization has to be s because s is odd under the reflection with the mirror plane) on the contrary if the initial state is even $\varepsilon \cdot \mathbf{x}$

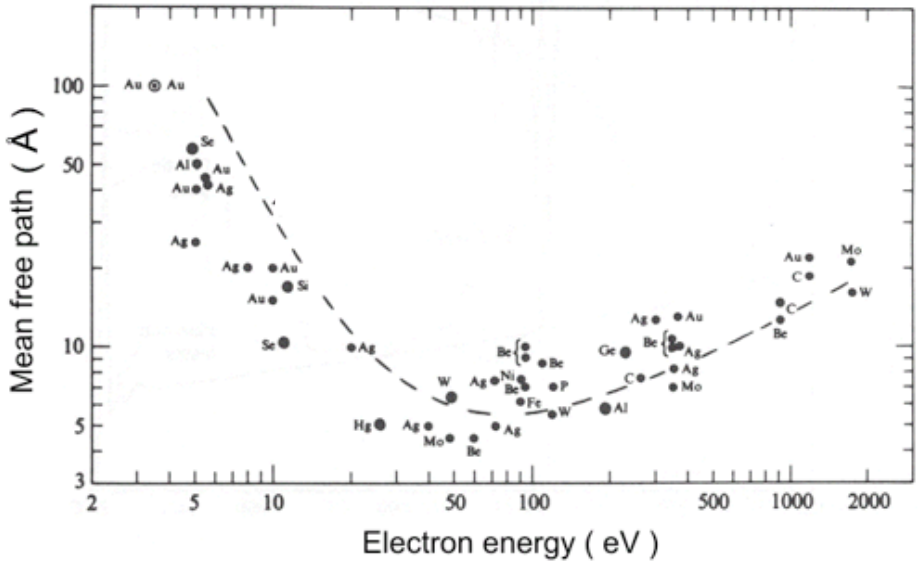

Fig. 3.16: Mean Free Path of excited electrons in solids versus their kinetic energy (from [177]).

has to be even (polarization p). An illustration of these symmetry properties can be seen in [170].

3.4.3 Probing depth

The second step of the three step model is essential to understand the probing depth of ARPES. The excited electron is transported to the surface therefore its mean free path gives the probing depth. This mean free path varies significantly according to its kinetic energy because of inelastic scattering. Fig.3.16 shows the mean free path of electrons in matter versus their kinetic energy. The variation of the ARPES intensity with the direction perpendicular to the surface, z, is given by:

$$I(z) \propto e^{\frac{-z}{\lambda cos(\theta)}} \tag{3.31}$$

where λ is the mean free path of the excited electron.

When choosing a photon energy one has to consider different aspects. For lower energy, less than 10 eV, the angle resolution is better and the probed depth is larger but the whole Brillouin zone can be too large to explore. Between 10 and 300 eV the intensity comes mostly from the surface and the angle resolution is preserved. For energy higher than 300 eV, more core levels can be reached and the probing depth increases with energy but the angular resolution worsens. One has to consider also $k_\perp$ to choose the correct energy to be in a specific plane in

the Brillouin zone. Because ARPES is a surface technique, surfaces have to be extremely clean and therefore they have to be prepared in situ.

We have seen that ARPES is a very powerful technique to visualize the band structure of a material. Analyzing its intensity can give insights on the symmetry of the orbitals. In the next section I will present the time-resolved version of ARPES.

3.5 Time-resolved ARPES

Time-resolved ARPES (tr-ARPES) consists of using a pump pulse and probing with another light pulse to perform ARPES. The energy of the probe pulse has to be higher than the work function of the material, typically above 4.5 eV. Experiments can be done using synchrotron radiation [18] as the probe pulse but the time resolution is intrinsically limited by the electron bunch width, about 100 ps. In order to obtain better time resolution laser systems have to be used to produce the pump and the probe pulse. Unfortunately, the highest energy achievable using nonlinear optics in solids is 6.994 eV [142]. J. Koralek et al. and M. Lisowski et al. proved that using a probe at 6 eV gives a spectral function similar to the one at higher photon energies [104, 109]. The major inconvenience of this type of probe is that only 0.5 $\mathring{A}^{-1}$ of the reciprocal space can be explored. Other systems using high harmonic generation exist but the generation of the probe pulse is done in gases which necessitates a more complicated setup. These setups generate higher energy photons, that enable a larger exploration of the Brillouin zone as well as a larger energy range [159, 84]. ARTEMIS is an open facility using high harmonic generation, which enables the exploration of a larger reciprocal space, for example the Dirac cone in graphene at the K point (1.6 $\mathring{A}^{-1}$) [93]. One of the major challenges of all tr-ARPES setups is to obtain a high enough repetition rate for the light source, to avoid problems related to excessive acquisition time. In this thesis I will only describe tr-ARPES using a 6 eV probe.

3.5.1 Fundamental principle

The fundamental principle is very similar to the other time-resolved techniques described earlier. A pump pulse excites the system and a probe pulse of 6 eV is used to perform conventional ARPES. This enables to directly probe the excited electrons and to unequivocally disentangle the electronic response from the other degrees of freedom. For example one can extract the exact electronic temperature for all delays as we did in [79]. In order to observe fast transient electron dynamics, the cross correlation between the pump and the probe has to be as small as possible

but the energy resolution is limited by the Fourier limit of a gaussian pulse by :

$$\Delta\omega\Delta t \geq 0.441 \tag{3.32}$$

where $\Delta\omega$ is the light frequency bandwidth and Δt the duration of the pulse. For example if the time resolution is 50 fs then the energy resolution can not be better than 73 meV.

There are two other limiting factors to tr-ARPES. The first is space charge that arises if too many electrons are emitted at the same time from the surface. This happens more frequently when the beam intensity per pulse is high. The electron bunch emitted from the sample is large and the electrons repel each other, therefore there can't be more than a certain number of photons per pulse. In order to increase the statistics the laser repetition rate must be kept high enough (at least 1 kHz). The second limitation is the pumping fluence. If the pump fluence is too high photoemission with 3 or more photons (multiphoton processes) can happen and the spectra are different from the one particle spectral function. All these factors have been accounted for in the FemtoARPES setup, described in the next section.

3.5.2 FemtoARPES setup

The FemtoARPES setup is the tr-ARPES experiment installed in the synchrotron SOLEIL. It is a collaboration among the LSI (école polytechnique), the LPS, (université Paris-Sud), and Synchrotron SOLEIL. Detailed information on the setup can be found in [63]. Fig.3.17 shows the photoemission chamber with the arrival of the two laser pulses. The manipulator consists of 5-axis (x-y-z-θ-φ) which enables to probe the entire Brillouin zone up to 0.5 $\mathring{A}^{-1}$ from the Γ point. The hemispheric analyzer is a SPECS Phoibos 150 which has an energy resolution of 10 meV and an angular resolution of 0.15°. The temperature can go from 30 K to 600 K. The vacuum is around 5 10^{-11} mbar.

Fig.3.18 shows the laser setup with the fourth harmonic generation. The laser system is a commercial Ti:Sapphire COHERENT laser, consisting of a MICRA oscillator and a RegA amplifier. A liquid crystal pulse modulator, called Silhouette, is used after the oscillator to correct the phase of the pulse in order to obtain a Fourier transform limited pulse as described in equation 3.32. The repetition rate of the system is 250 kHz and delivers a 35 fs, 6 μJ pulse at a wavelength of 790 nm (1.55 eV). The fundamental frequency is then separated into two pulses, one is used to pump the material and the other one is used to produce the fourth harmonic for probe pulse.

In non linear optics, the two input waves and the output wave have to interfere constructively in order to produce the highest output intensity. The constructive

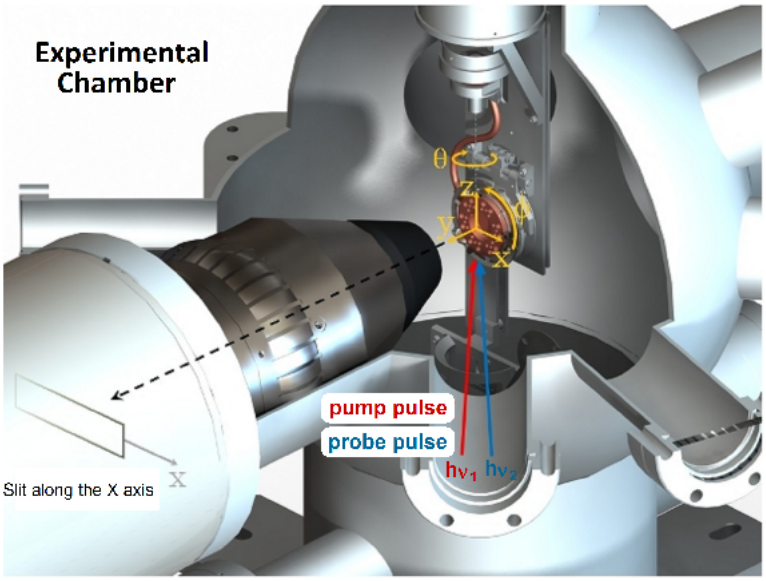

Fig. 3.17: Experimental chamber of the FemtoARPES setup.

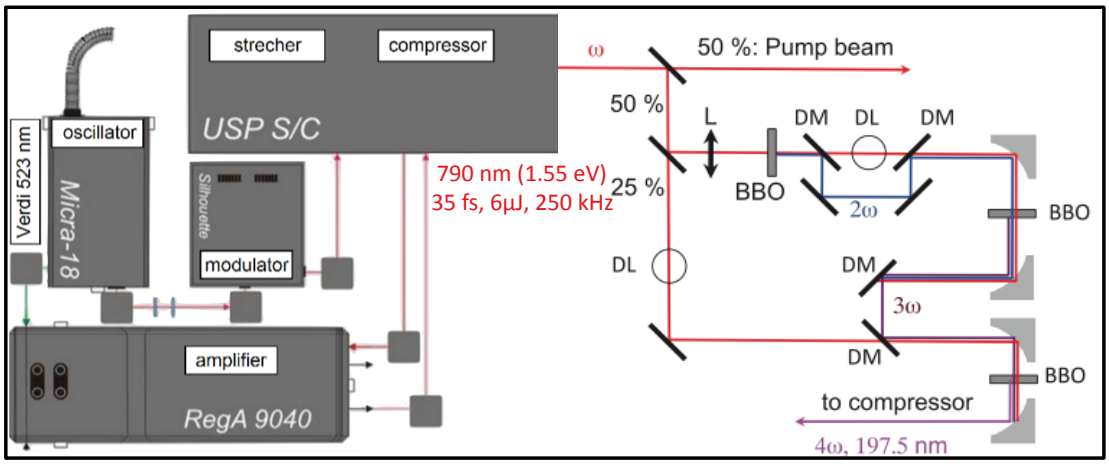

Fig. 3.18: FemtoARPES laser setup to produce the fourth harmonic

interference imposes a phase matching of the three waves. In order to obtain the highest photon energy for the probe pulse it was calculated that the generation of the fourth harmonic using the fundamental plus the third harmonic would be better than just doing two frequency doubling in cascade because of phase matching. All frequency mixing or doubling are done in BBO crystals. First the fundamental is doubled then the third harmonic is created using the second harmonic plus the fundamental. Finally the fourth harmonic is produced using the third harmonic and the fundamental. The final pulse has an energy of 6.28 eV with a duration of 55 fs therefore an energetic resolution of 56 meV. The overall temporal resolution of the experiment considering also the pump pulse is 70 fs. These conditions are achieved when the laser and the harmonic generation are perfectly aligned, the most common temporal resolution is a 100 fs and 80 meV for the energety resolution.

The FemtoARPES setup was used to study the ultrafast electron dynamics of V_2O_3 described in the Chapter 5. The good time resolution enabled the resolution of the very fast dynamics. Since the photons used are around 6 eV, the mean free path of the photoelectrons is large therefore the bulk properties are probed (see Fig.3.16).

Chapter 4

Tracking the Lattice

The major advantage of time-resolved experiments is to decouple for a few hundred of femtoseconds the electrons and the lattice. The relaxation pathways will be guided by the coupling between them. Therefore the responses of the electrons and the lattice after a photoexcitation have to be probed separately in order to deconvolute them. In correlated material a change in the lattice structure has a big impact on the electronic structure. Therefore probing the lattice is essential to understand the properties of the excited state. In this chapter, I will look at the lattice response of V_2O_3 upon photoexcitation using time-resolved single color reflectivity and time-resolved X-ray diffraction.

4.1 Time-resolved optical reflectivity study of V_2O_3

As we have seen in chapter 1, the band structure of V_2O_3 is extremely sensitive to its trigonal distortion which is related to the frequency of the A_{1g} phonon. Fig.4.1 shows the A_{1g} phonon, which is a breathing symmetric optical phonon mode. At equilibrium, the PI phase has a higher Raman phonon frequency than the PM phase [188]. Tracking this frequency in time can provide a probe to understand the structural changes that occur during photoexcitation or during a phase transition.

O. Misochko et al. performed time-resolved optical reflectivity on V_2O_3 and showed that the A_{1g} phonon was blue shifted compared to the Raman frequency [125]. A photoinduced blue shift is very rare because an equilibrium heating effect would produce a red shift because of the lattice expansion. A hardening of the bonds also exists in gold and graphite. The one in gold only happens for extremely high fluences [60]. For graphite, the hardening is due to a reduction of the electron-phonon coupling at high electronic temperature [205]. B. Mansart et al. carried out

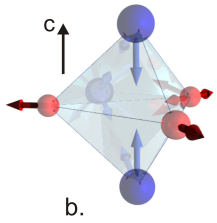

Fig. 4.1: A_{1g} optical phonon mode (from [117])

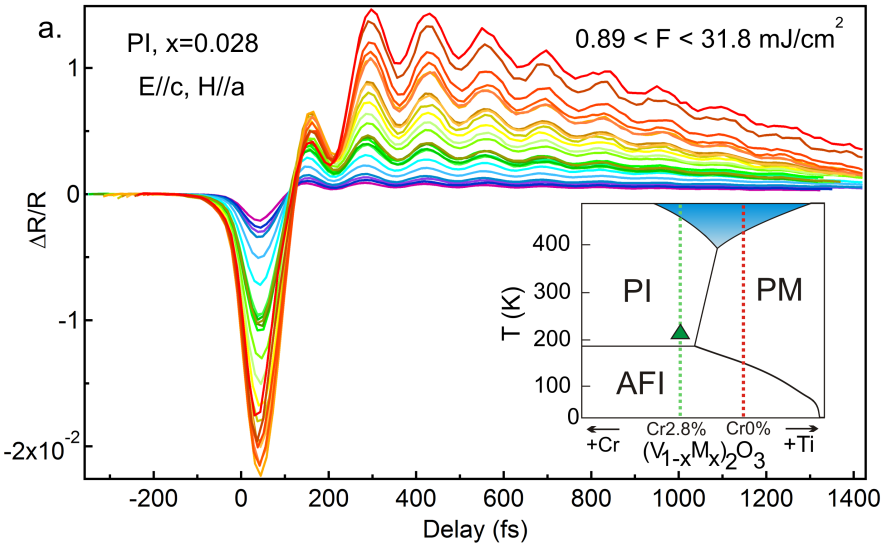

Fig. 4.2: Time-resolved reflectivity in the PI phase. The oscillation represent the coherent optical phonon (from [117])

an extensive study on V_2O_3 in the PI and PM phase looking at the frequency of the A_{1g} according to the crystal directions [117]. The experimental setup used is the one described in section 3.2.1. Fig.4.2 shows a time trace of $\Delta R/R$. The first peak is a pure electronic response that lasts less than 200 fs. The oscillatory component is the A_{1g} phonon, which can be extracted by subtracting the non oscillatory background and fitting or performing the Fourier transform of the oscillation.

All the traces were fitted with a single frequency for the A_{1g} phonon, and one for the E_g phonon, when it was observed. Fig.4.3 shows the frequencies for different fluences, dopings, and crystal direction. All directions show a hardening compared to the Raman frequency but the strongest shift occurs when the photon propagation vector k is parallel to the c axis. For c in plane and the electric field E is parallel to a or b crystal axis, the hardening is clearly fluence dependent. At higher fluence all the frequencies tend to lower, which is consistent with a heat increase that softens the bonds. We have seen that the a_{1g} orbitals are bonding.

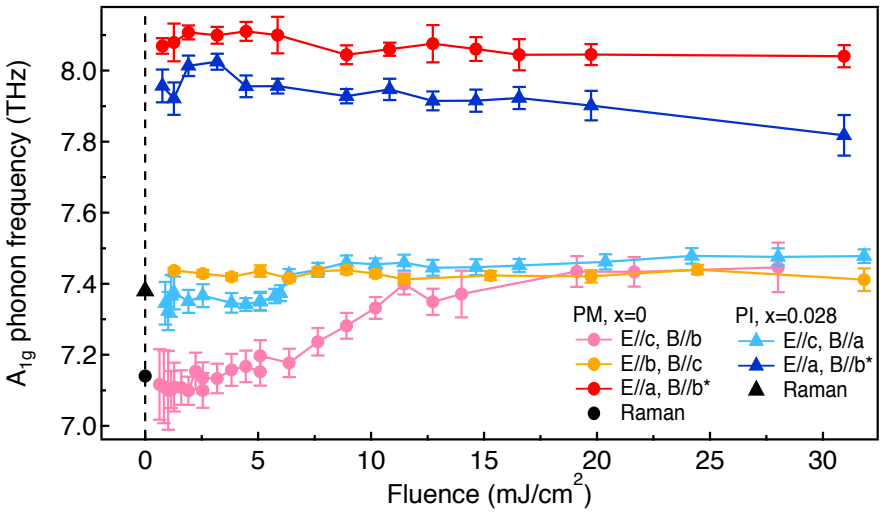

Fig. 4.3: Coherent A_{1g} optical phonon frequency for different fluences, dopings, and crystal directions. The photoinduced frequencies are all blue shifted compared to Raman frequency. (from [117])

1.5 eV is exactly the energy needed for the e_g^π to a_{1g} transition. As we have seen, the a_{1g} orbitals are bonding and can explain the hardening seen. The e_g^π to a_{1g} transition is a d-d transition, therefore according to the selection rules electric dipole transition should be forbidden; but since there is significant d-p mixing with the oxygen atoms they are allowed. The transition is also enabled by electric quadrupole and magnetic dipole. Projecting the momentum operator on the t_{2g} orbitals, one finds that the most efficient transition rate is when the crystal axis c is parallel to the photon propagation vector k, which is what is seen in the experiment.

The observation of coherent phonons lasts only for 1.5 ps and the hardening seems to still be present. Time-resolved optical reflectivity can only probe coherent phonons therefore when the phonons lose their coherence they can not be observed anymore. The structural information is available as long as the phonons are observed, which in our case is 1.5 ps. Since this phenomenon is structural, its lifetime can be relatively long. The question is how long does this hardening lasts? The hardening supposes that the V_1-V_4 distance is reduced and thus changes the trigonal distortion. The electronic structure of V_2O_3 is extremely sensitive to it therefore the electronic structure might be affected by the structural change. In the next section we tried to observe exactly the lattice deformation using time-resolved X-ray diffraction, and tackle the question of the lifetime of the hardening. The effect of the hardening on the electronic structure will be investigated in the next chapter.

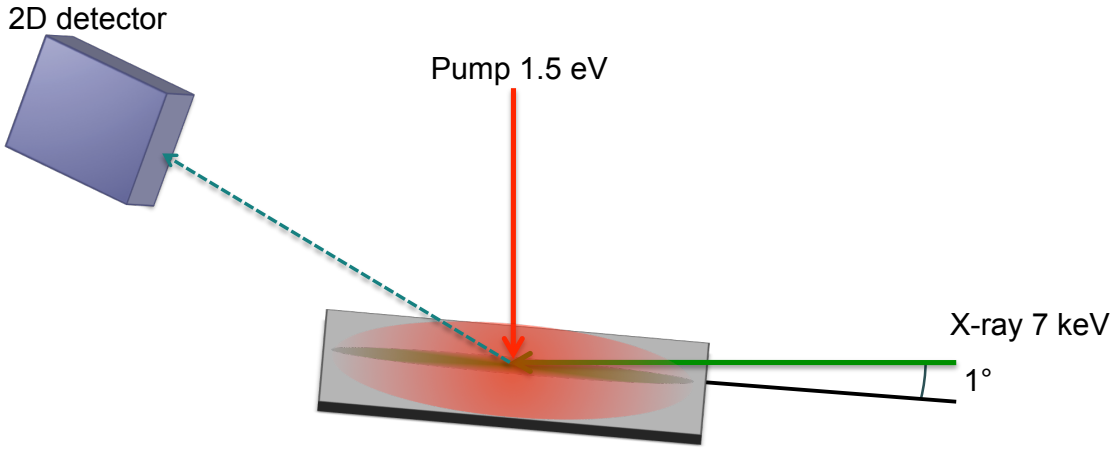

Fig. 4.4: Time-resolved X-ray diffraction geometry. The X-rays are grazing to match the penetration depth of the laser.

4.2 Time-resolved X-ray diffraction study of V_2O_3

We performed time-resolved X-ray diffraction on V_2O_3 in the PI and PM phase. The experiment were performed on the beamline 6.0.1 at ALS (Berkeley) and on the beamline Cristal at Soleil (Saint-Aubin). The temporal resolution was about 100ps. Fig.4.4 shows the experimental setup. The spatial overlap in depth was achieved by diffracting in grazing incidence at 1°, which gives a penetration length at 7 KeV of 115 nm [9]. The pump laser is in normal incidence and has a penetration length of 112 nm [106]. The spreading of the focal spot of the X-ray is about 2 mm. Since the pump and the probe wavefronts are not colinear, the X-ray does not see a temporal homogeneous excitation. The pump-probe delay at the two extremities of the sample are different. This delay difference is 6.6 ps, which can be neglected compared to the time resolution of the experiment. As explained in 3.3.3, we first looked at the average heating effect with the 2D detector and then performed time-resolved measurements using a point detector.

The position of the Bragg peak on the 2D detector can be seen in Fig.4.5. The unit cell is hexagonal therefore only 2 non collinear Bragg reflections are necessary to obtain the change of the lattice parameters a and c. We use the (113) and the (116) Bragg reflections that can be obtained in grazing incidence with a crystal that is cut with the (110) direction perpendicular to the surface. Using the position of the Bragg peaks on the 2D detector, which gives a directly a 2θ value, and using equation 3.10, we calculate the lattice deformation $\Delta a = 0.00153$ Å and $\Delta c = -0.002$ Å for 10mJ·cm^{-2}. The thermal expansion of a and c are α_a=6.5 10^{-6}Å·K^{-1} and α_c=-2.9 10^{-6}Å·K^{-1}. The lattice parameter deformations are equivalent in temperature to ΔT_a=46 K and ΔT_c=49 K for 10mJ·cm^{-2} and ΔT_a=18 K and

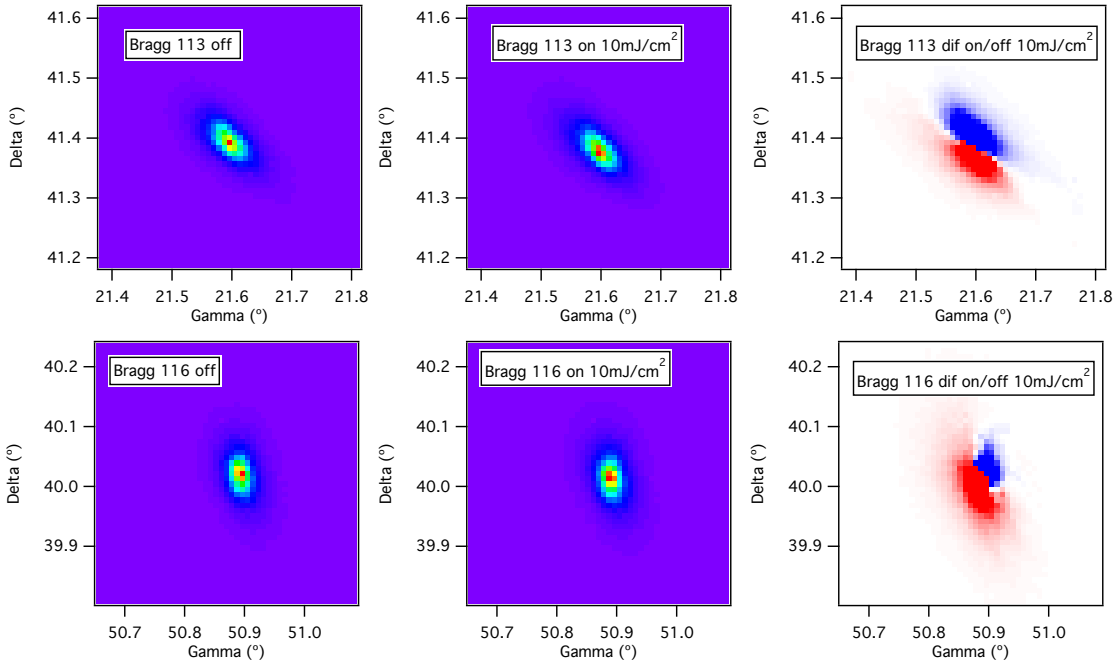

Fig. 4.5: Position of the Bragg peak on the 2D detector with and without the pump laser. The shift of the Bragg reflection corresponds to a dilatation of the lattice parameters because of a heat increase of 50 K due to laser heat accumulation.

ΔT_c=19 K for 5 mJ·cm^{-2}. This heat accumulation is surprisingly high because the thermal conductivity of V_2O_3 is 0.03 W·cm^{-1}·K^{-1} [6] not much lower than other materials that don't present this effect (Bismuth is 0.08 W·cm^{-1}·K^{-1}). This effect is seen in the PM phase and the PI phase. The data shown were done for a 5.6% Cr doped sample but the same results were obtained for the pure V_2O_3 sample.

Since the use of the 2D detector gives the direct value of the lattice parameter, we can use the new values of the peak position to see if the orientation matrix has changed. Fig.4.6 shows the rocking curve according to the Kϕ angle (angle that rotates the sample keeping the surface direction constant) with and without the pump laser. The shift of the peak is opposite to the one expected with a temperature change. We can conclude that the crystal axis direction changes when the laser is turned on therefore the sample rotates. We recompute the orientation matrix for the sample with the laser turned on to account for the sample rotation.

We carried out time-resolved experiments on the pure V_2O_3 sample with different grazing incidence angles and looking at the (113), (116), and (024) Bragg reflections. Fig.4.7 shows the Kω rocking curve of the (113) Bragg reflection for various delays and incidence angles. The Kω angle is the standard θ angle of the

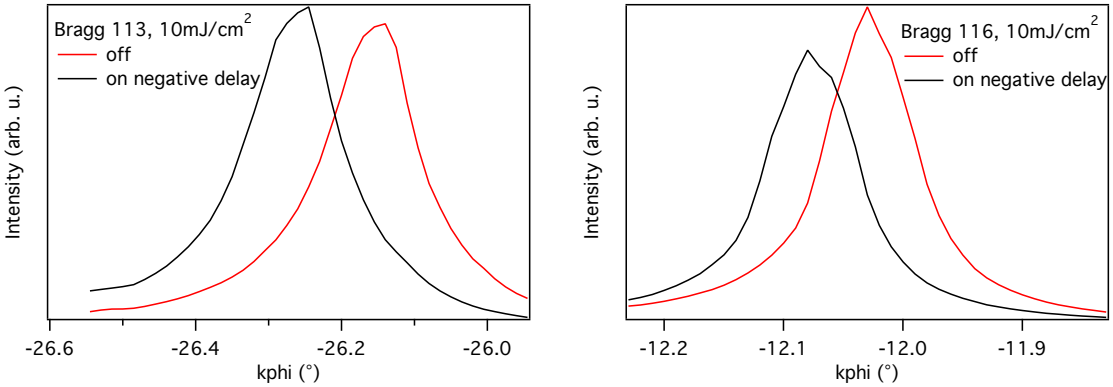

Fig. 4.6: Kϕ Rocking curve wih and without pump laser. The laser heat accumulation makes the the crystal turn, which related to a peak shift.

difractometer. Varying the incidence angle changes the penetration length of the X-ray, the larger the angle the deeper the probing depth. The differences between positive and negative delay are plotted beside. As seen before there is always a shift of the peak between the negative delay and the pump laser off. The differences in negative delays are always flat indicating that our normalization is well performed. For all the incidences, the 2 ns delay is typical of a peak shift, which is an odd function compared to the point were the difference crosses zero. The shift is smaller and smaller with increasing incidence. The 0.06 ns is very different: for small incidences the difference is very asymmetric and for larger incidence it becomes more symmetric. Very similar features are seen in the (116) and the (024) Bragg reflection.

In order to better understand the short timescales we look at the differences according to delay. The differences for the (113) Bragg reflection are represented in Fig.4.8. We again notice that at the short time scales the differences are more asymmetric for the small incidence angle. Moreover this first state is shorter in time for small incidence angles than for large incidence angles. For 1° incidence the first state lasts 100 ps and for 4° incidence it lasts 400 ps. The integral of the peaks and their center of mass are shown in Fig.4.9. The integrated Bragg reflection intensity is affected by the Wyckoff positions and the Debye-Waller factor. The center of mass gives the shift of the peak if the shape of the rocking curve does not vary significantly. We have seen that the difference is very asymmetric for short timescales therefore the center of mass does not give a precise indication of the shift of the peak for those delays. But the center of mass is very precise for longer timescales since the difference is symmetric.

The first intriguing feature concerning the integral curves is the first initial peak. The intensity increases which is completely different than a temperature increase.

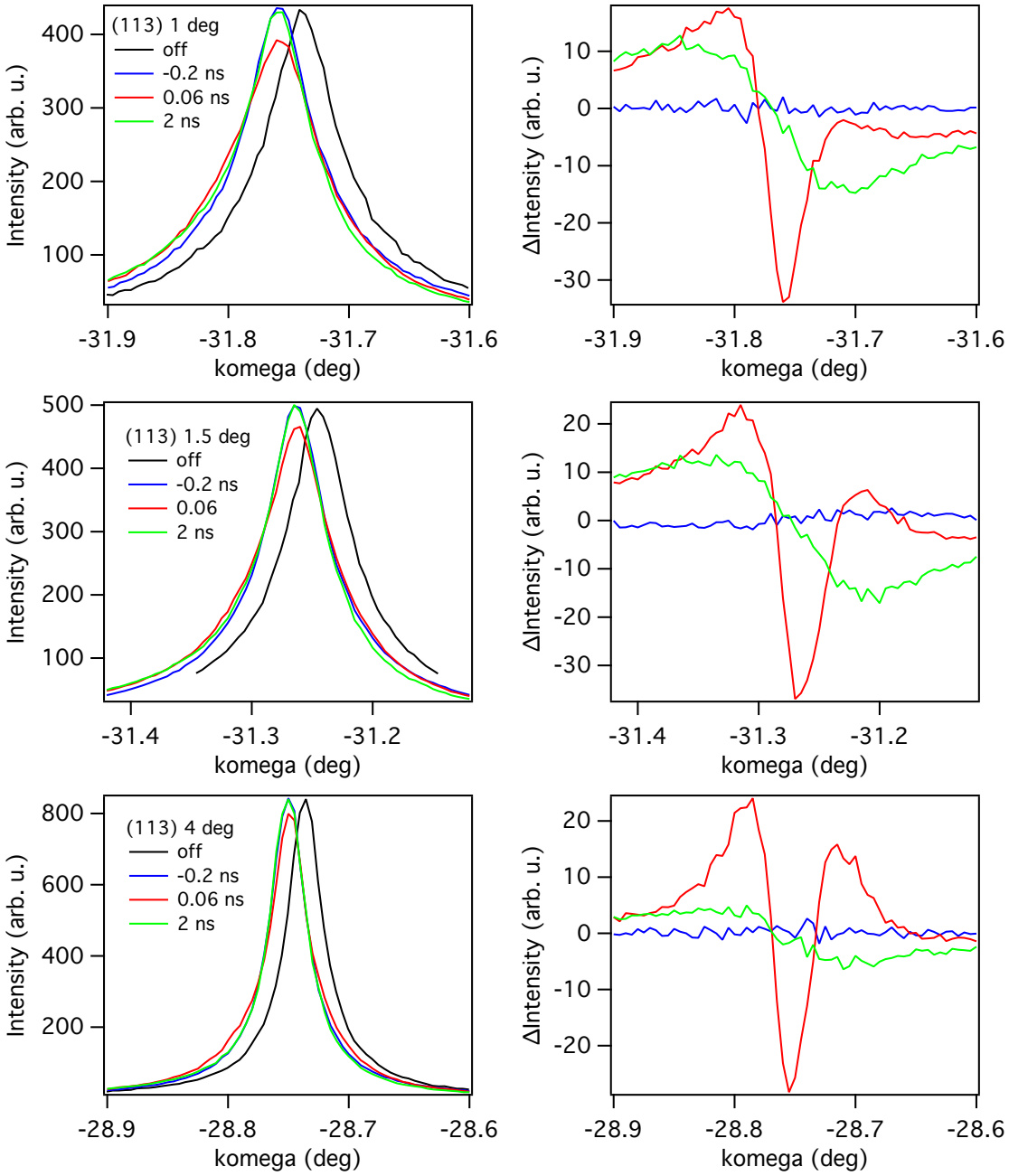

Fig. 4.7: Kω rocking curve of the (113) Bragg reflection for various delays and incidence angles. The difference at 60 ps is asymmetric whereas at 2 ns is symmetric.

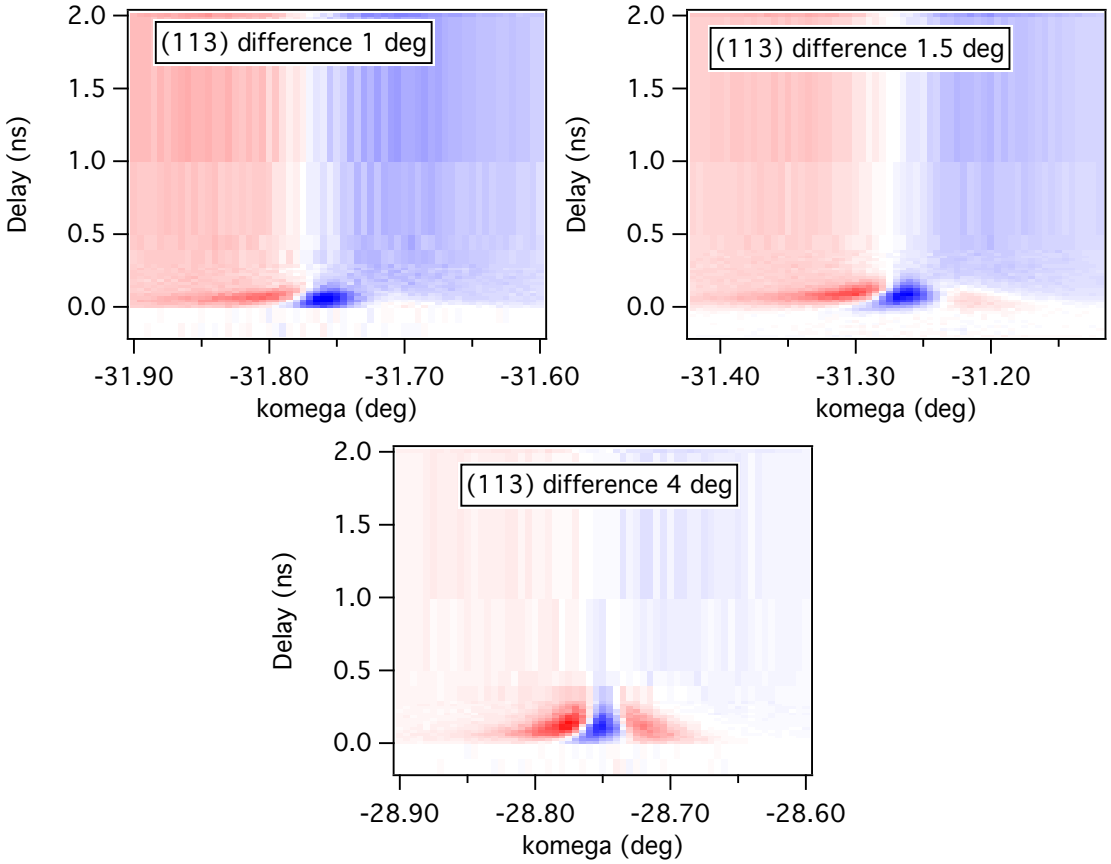

Fig. 4.8: Kω rocking curve differences for the (113) Bragg reflection versus delay. Red is positive and blue is negative.

A Debye-Waller factor only diminishes the intensity with increasing temperature. The second factor that affects the intensity is the structure factor that is calculated with the Wyckoff position for the Oxygen X_O and the Vanadium Z_V, for which the variation of intensity is shown in Fig.4.11. The structure factor of the (113) Bragg does not depend on the Z_V position therefore one can calculate directly the X_O change. The Z_V position is calculated with the (116) intensity variation. We then calculate the intensity of the (024) which is smaller than one while it is found experimentally that it is bigger than one, as seen in Fig.4.9. A change of the Debye-Waller factor nor a variation of the Wyckoff positions can explain the increase of intensity seen. The maximum of the intensity shifts according to the incidence angle. Fig.4.10 plots the delay of the maximum intensity versus penetration depth of the X-ray taking the zero delay for the most grazing incidence. The linear regression gives a slope of 6.8 10^5 cm/s, very close to the sound velocity along the (110) direction which is 7.2 10^5 cm/s [209]. We can conclude that the first peak is due to a shock wave propagation in the z direction, similar to the acoustic phonons observed using time-resolved reflectivity [115].

The intensity at a delay of 2 ns can also be analyzed using a structure factor change. The first approximation is to neglect the Debye-Waller factor. We perform the calculation for an incident angle of 1.5°. Using the intensity of the Bragg reflection (113) and (116) we find the relative Wyckoff positions of X_O=0.99522 and Z_V=1.00036. The calculated intensity for the (024) reflection, with X_O=0.99522 and Z_V=1.00036, is 1.01657 to compare to the experimental value of 1.0136, which is very satisfying. The variation of the intensity versus the relative Wyckoff position is shown in Fig.4.11. At equilibrium, the Wyckoff positions change with temperature and the time-resolved variation observed is equivalent to 31 K, which is calculated with the positions found in [155].

The intensity gives a value of the change of the Wyckoff position but not the ratio of c/a. The orientation matrix can be used to calculate the change in the lattice parameters for the 2 ns delay. In Fig.4.7 the peak at 2 ns is shifted compared to the negative delay. Since the difference is not asymmetric the center of mass gives a good value for the position shift. The change of the lattice parameter can be captured by equation 3.14. We rewrite the equation using a metric change which changes the orientation matrix:

$$UB' = \begin{pmatrix} a*_x & b*_x & c*_x \\ a*_y & b*_y & c*_y \\ a*_z & b*_z & c*_z \end{pmatrix} . \begin{pmatrix} \frac{a*_{pos}}{a*_{neg}} & 0 & 0 \\ 0 & \frac{b*_{pos}}{b*_{neg}} & 0 \\ 0 & 0 & \frac{c*_{pos}}{c*_{neg}} \end{pmatrix} \tag{4.1}$$

where UB' is the new orientation matrix. a^*_x, a^*_y, and a^*_z are the projection of the a^* reciprocal vector on the axis of the diffractometer. $a*_{pos}$ and $a*_{neg}$ are the reciprocal lattice parameters for a positive and negative delay. We suppose

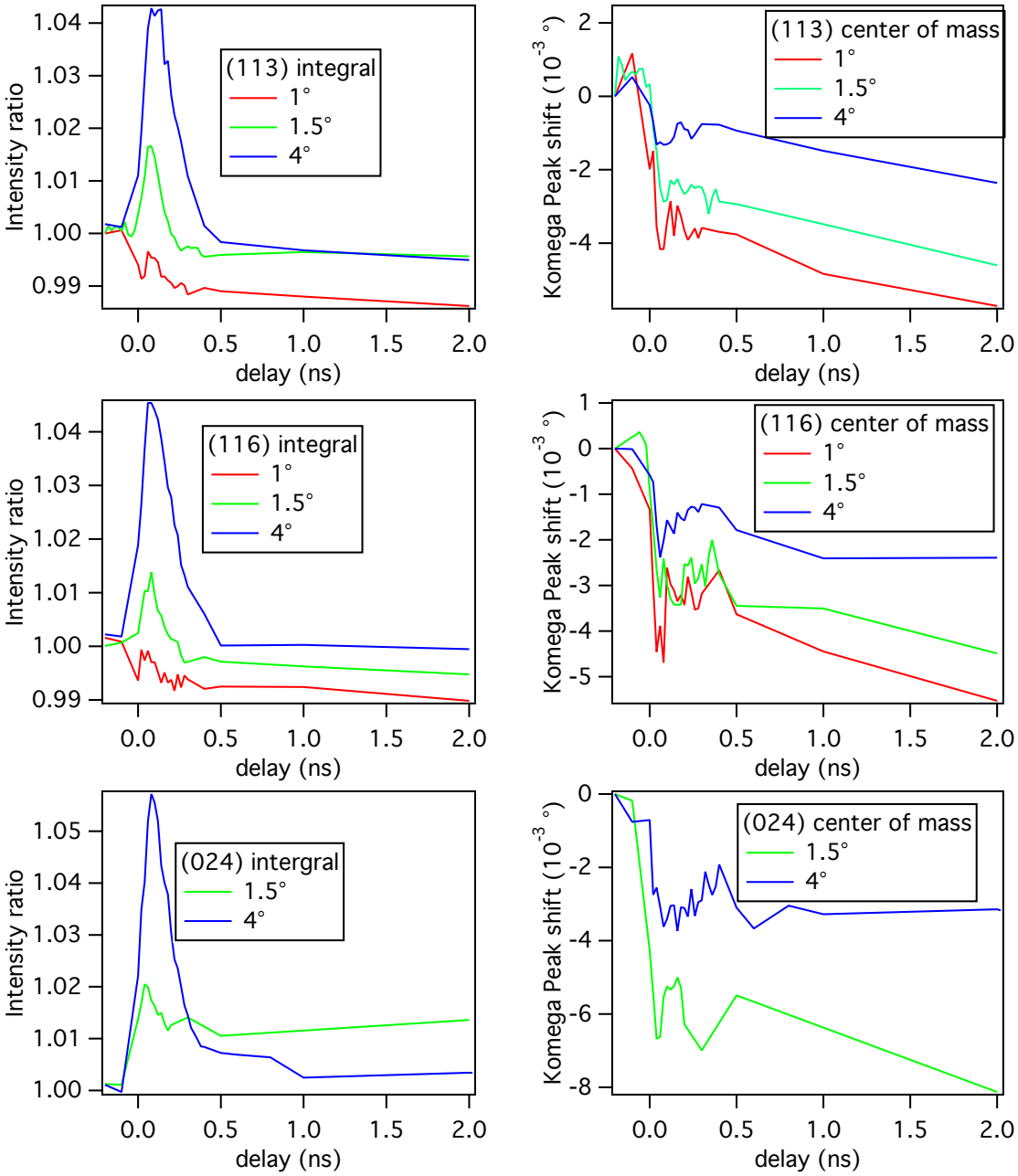

Fig. 4.9: Integral of the peak and center of mass of the peak in Kω for different incidence angles and Bragg reflection. The increase in intensity during the first 300 ps is not compatible with heat nor with a modification of the structure factor. At 2 ns, the change is equivalent to an increase of temperature of 30 K.

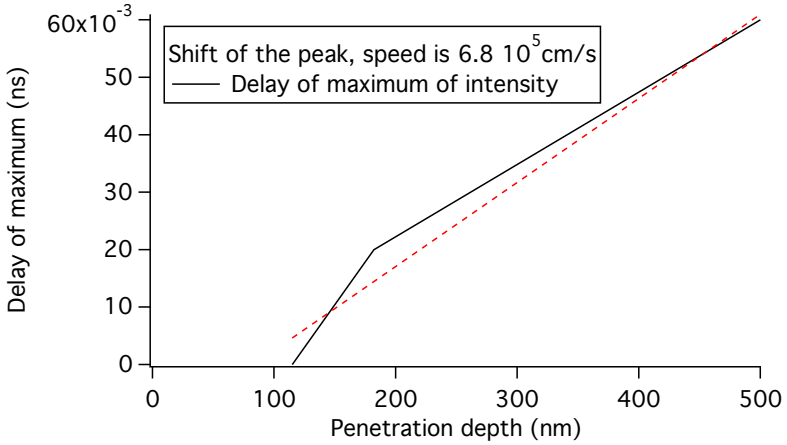

Fig. 4.10: Delay of the maximum intensity change versus penetration depth. The speed of the deformation is the same as the speed of sound in the material.

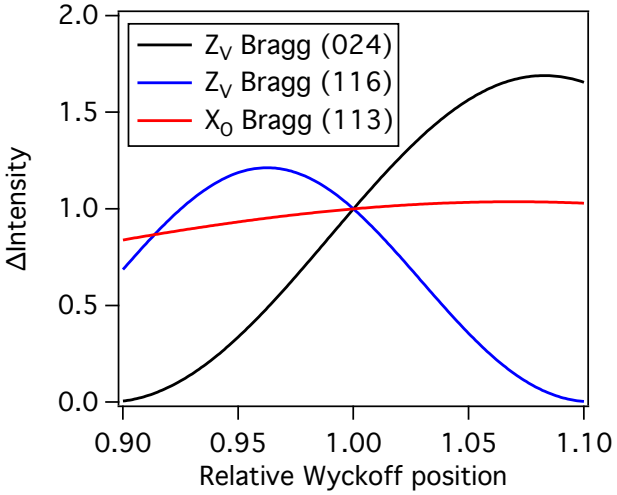

Fig. 4.11: Intensity of Bragg (113), (116), and (024) versus relative Wyckoff position.

that a*=b*. The hypothesis is that the lattice directions $\vec{a}*$ and $\vec{c}*$ do not rotate in time and only their norm change, which is reasonable for short delays. Using the shift for the 1.5° incidence for the 3 Bragg reflections we find the new lattice parameter $\Delta a = 6.4610^{-4}$ Å and $\Delta c = -5.77910^{-4}$ Å for 5mJ·cm^{-2}, which gives an equivalent temperature raise of ΔT_a=19.5 K and ΔT_c=14.3 K. There are only 2 lattice parameters therefore theoretically only 2 Bragg reflections are sufficient. We verify the results by using only the (113) and the (116), which gives ΔT_a=19.2 K and ΔT_c=10 K. The error using this method to analyze the shift of the peaks is quite big but still gives an order of magnitude. Therefore we can conclude that there is an increase of temperature of about 20 K at 2 ns delay, similar to the analysis using the Wyckoff position.

The heating seen can be compared to the theoretical heat deposited by the pump laser. The calculated change of temperature due to the energy deposited by the pump laser is :

$$\Delta T_L = \frac{AF\Omega}{l_s C_p} \tag{4.2}$$

where A the absorption coefficient ($A = 0.773$ [11]), l_s the optical penetration depth ($l_s = 118$ nm [11]), Ω the molar volume of the hexagonal unit cell, ($\Omega = 3.010^{-5} m^3 \cdot mol^{-1}$ [51]), F the fluence of the pump laser, and C_p the heat capacity of V_2O_3 ($C_p = 102$ J·Mol^{-1}·K^{-1} [99]). For a fluence of 5 mJ·cm^{-2} we find ΔT_L= 96 K which is higher than the experimental value of 20-30 K. The main approximation is the overlook of the electron diffusion, which can be quite significant in bulk materials [23]. The difference between the calculated value and the measured value suggest that more than half the energy of the pump is evacuated by electron diffusion and the shock wave during the first 300 ps.

At 2 ns the relative ratio change of c/a is 0.99983, which is significantly different from what is expected from the phonon hardening data of time-resolved reflectivity. It is most likely that the phonon hardening has disappeared at 2 ns and even after 100 ps since a change of the c/a ratio of 4% would produce a drastic effect on the peak position. Time-resolved X-ray diffraction might be unable to detect the hardening because of the lack of temporal resolution or because of the perturbation by the shock wave. These measurements have shown that the phonon hardening is not present at 2 ns and a shock wave is present for the first 300 ps. Further investigations using free electron laser are needed in order to observe the phonon hardening with the required time resolution. The incidence angle should be kept very small to avoid the detection of the shock wave.

Chapter 5

Tracking the electrons

In the previous chapter we have seen the evolution of the lattice after a laser excitation. We have seen that the lattice presents a hardening at short timescales and then the energy is relaxed through the lattice, which leads to an equivalent temperature increase of about 20-30 K for 5 mJ/cm^2. Since the electron-phonon coupling in correlated materials is extremely strong, a change of the lattice affects the electronic structure. Probing directly the electronic structure provides the means to understand the cause or the consequence of the structural change.

In this chapter we will focus on the electronic structure evolution of the material. In the first section, I will look at the possibility of photoinducing a phase transition between the PM to the PI phase in V_2O_3. The probe used will be time-resolved THz spectroscopy. In the second section, I will track precisely the electronic structure using time-resolved ARPES in V_2O_3 and in $BaCo_{1-x}Ni_xS_2$.

5.1 Time-resolved THz spectroscopy study of V_2O_3

THz time domain spectroscopy is a very good method to probe the gap of a material as seen in chapter 3. The Thz pulse is blocked if the material is metallic and is transmitted if it is insulating. Fig.5.1 shows the loss function for different points in the phase diagram. The difference between the PM phase and the PI phase is clearly visible and no resonances are seen therefore in this THz region the property probed is the presence of free carriers. For a 1.1% Cr doping V_2O_3 crosses the PI-PM phase transition with temperature. This transition is a pure Mott transition with no symmetry breaking therefore if the transition is purely electronic one should be able to photoinduce extremely rapidly the transition. If the transition is structurally driven the transition should be slower. Previous experiments have shown that for pure V_2O_3 thin films, it is possible to go from the

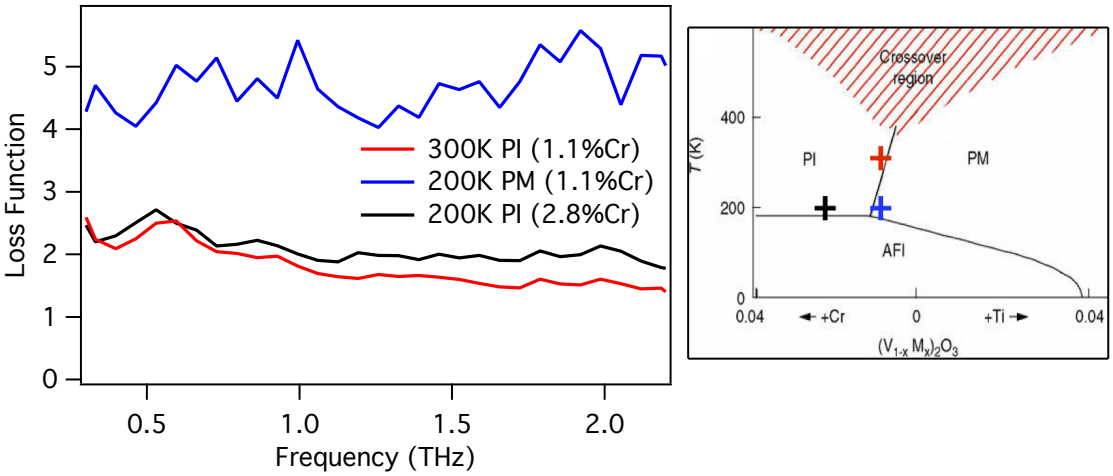

Fig. 5.1: The loss function derived from THz transmission spectroscopy for $(V_{1-x}Cr_x)_2O_3$ (x=0.011) at 300 K (PI phase) and 200 K (PM phase) and for $(V_{1-x}Cr_x)_2O_3$ (x=0.028) at 200 K (PI phase). Positions of the different measurements points on the phase diagram. The flat loss function is a good signature of the gap since there are no resonances in this THz range. The loss function is low in the PI phase because the THz pulse is well transmitted and high in the metallic phase.

AFI phase to the PM phase with a laser pump pulse [110] or an electric pulse [31]. The induced transition is shown to be thermally induced because the incubation time is slow. This transition is accompanied by a symmetry breaking therefore it can not be considered as a pure Mott transition. To my knowledge, there has been no report trying to photoinduce a Mott insulator from a correlated metal where no symmetry breaking is seen.

The V_2O_3 samples were cut from high quality single crystals from Purdue University and were oriented using Laue diffraction in order to have the (110) direction in the hexagonal notation perpendicular to the surface.

$(V_{1-x}Cr_x)_2O_3$ (x=0.011) goes through the Mott transition at around 230K. The enthalpy of this transition is very small because there is no symmetry breaking [99], therefore the energy needed to transit is also small. Fig.5.2 shows the equilibrium THz transmission versus temperature. The hysteresis loop is clearly visible and the transition is very abrupt because the sample is a monocrystal. In powders the transition is smoother because different crystal domains have different transition temperature [112].

Fig.5.3 shows the THz transmission when pumping the material. The black triangles are the starting points at different temperatures in the PM phase where the system was pumped. In order to verify the starting point of the measurements

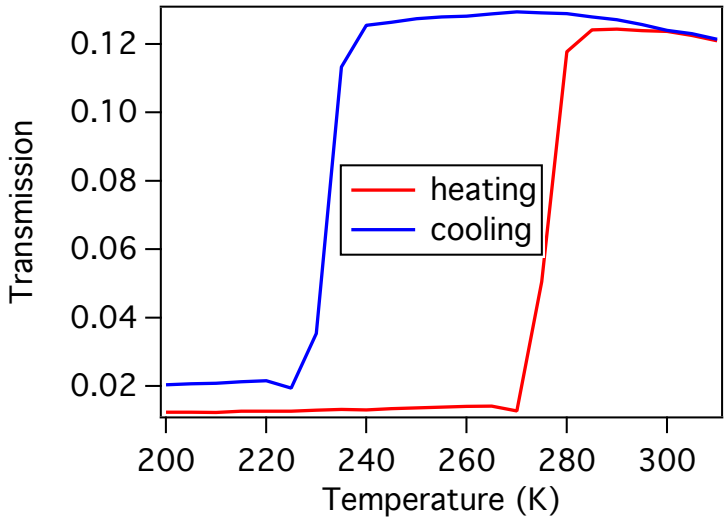

Fig. 5.2: The equilibrium THz transmission in the hysteresis cycle of $(V_{1-x}Cr_x)_2O_3$ (x=0.011), red being the heating and blue the cooling.

we monitored the transmission at negative time delays. When the fluence was increased the system transits to the PI phase. If the starting temperature is below the hysteresis loop when the pump is turned off the material transits back to the metallic phase. However if the starting temperature is inside the hysteresis, the system stays insulating and only transits back if the temperature is lowered outside the hysteresis. The fluence needed to transit from metallic to insulator is proportional to the distance between the starting temperature and the transition temperature of the heating cycle. The transition can be incomplete if the fluence is not high enough, these effects are surely due to domain formation [112]. All these transitions are due to heat accumulation from the 1 kHz pump: the sample does not have time to evacuate the heat between two pulses. The grey area represents the energy needed for the transition. No time-resolved signal was seen at any temperature using fluences lower than the one used to transit completely. No sign of a purely electronic photoinduced phase transition is seen starting in the PM phase. The electronic bath is initially heated at extremely high temperature, which would trigger the phase transition if the electrons were the motor of this phase transition. The non observation of the purely electronic phase transition shows that only heating the electron is not enough for the phase transition to be triggered or that another phenomenon pushes the material in another direction, such as the hardening. As we have seen in the previous chapter, when the laser is turned on there is heat accumulation of 20 K for 5 mJ/cm^2 plus a pulse to pulse heat increase of 20 K. In order for the material to transit back to the lower temperature state the accumulated heated state should be outside the hysteresis

thus at 220 K. The pulse to pulse temperature increase should then be around 60 K for the material to transit back and forth. Using the observation of the X-ray diffraction, a 60 K pulse to pulse temperature increase is accompanied by a 60 K heat accumulation. Therefore the original temperature state should be 160 K, which lies in the AFI phase. Unfortunately bulk V_2O_3 breaks when passing through the AFI transition. Thus the photoinduced phase transition with the sample that retransits after each pulse is not possible with a 1 kHz laser system. Moreover it was observed that the material takes about 1 s to transit back when turning off the pump laser. The solution to observe the photoinduced transition with a time resolution is to perform the experiment at 1 Hz but the signal to noise ratio of our experiment is too low to be able to do experiments at 1 Hz.

The time-resolved measurement in the PI phase were performed by varying the pump delay while sitting on the peak of the THz pulse. We verified that the loss function stayed flat at different delays. Fig.5.4 is the time-resolved change in transmission of the $(V_{1-x}Cr_x)_2O_3$ (x=0.011) at 300 K (PI phase). The change is negative suggesting that the THz pulse is more reflected or absorbed after photo excitation, thus suggesting a metallization of the material. At 0.5 mJ/cm^2, the first sharp peak is limited by the time resolution of our experiment (300 fs) and is surely a pure electronic excitation. This feature is also seen in time-resolved optical reflectivity [115]. The signal reaches a plateau with τ_1=2.7 ps same as for the 1.6 mJ/cm^2 curve, which does not have a sharp first peak maybe because of heat accumulation. The phonon hardening supposes that the V_1-V_4 distance reduces therefore pushing the system towards a metallized state. The relaxation with τ_1=2.7 ps could be the result of the hardening effect but unfortunately an increase of temperature would produce the same effect. An increase of temperature also creates more free carriers near the Ferrmi level that can block the THz pulse. In order to distinguish between an increase of temperature or a consequence of the hardening, we probe the spectral function of the material using time-resolved ARPES.

To my knowledge, all previous experiments photoinducing phase transitions have been carried out on materials where the high temperature phase was a metal. We have shown for the first time that a laser pulse is able to switch a metal to an insulator. Although the mechanism of the switching is surely due to heat accumulation from the kHz laser pump, using a single high fluence pulse would enable the photo switching. As we have seen in the previous section the heated state is already present at 1 ns. Therefore the photo switching should be faster than 1 ns.

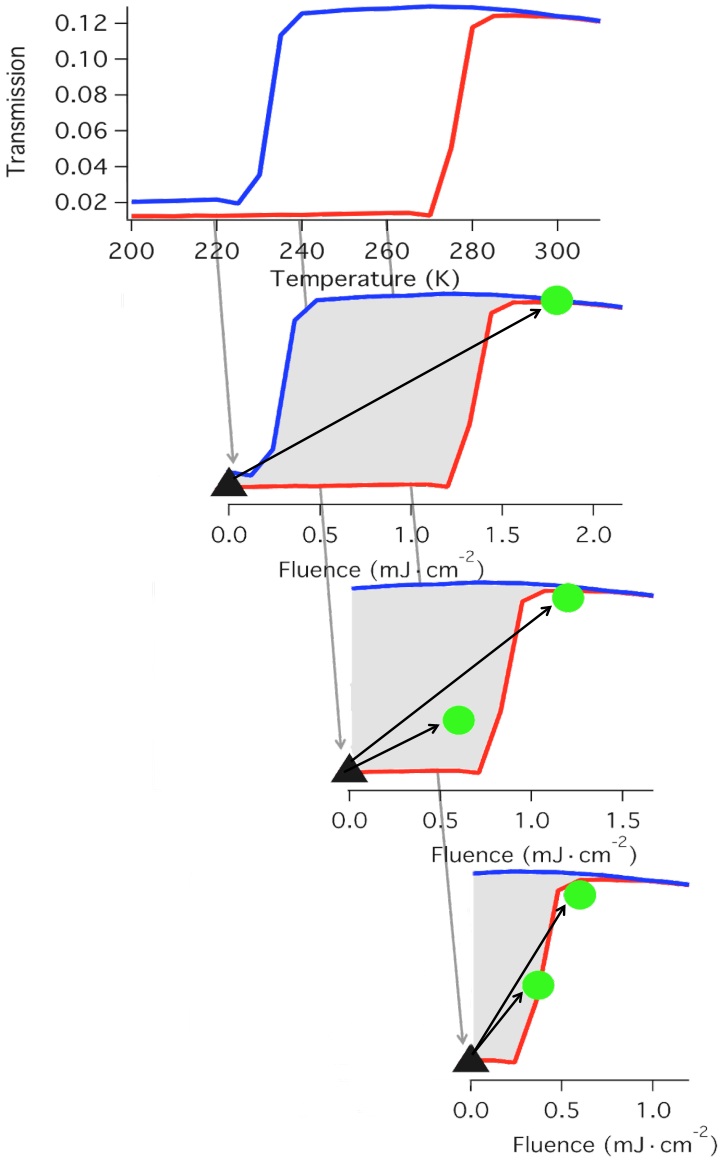

Fig. 5.3: Negative time delay transmission of $(V_{1-x}Cr_x)_2O_3$ (x=0.011) with a pump laser. The black triangles show the initial transmission before pumping the sample. The green circles are the transmission at negative delays. The arrows indicate the effect of the optical pump. The phase transition is triggered by the accumulation of heat of the 1 kHz pump pulse. The fluence threshold is linear with the distance from the starting point to the heated line of the phase transition.

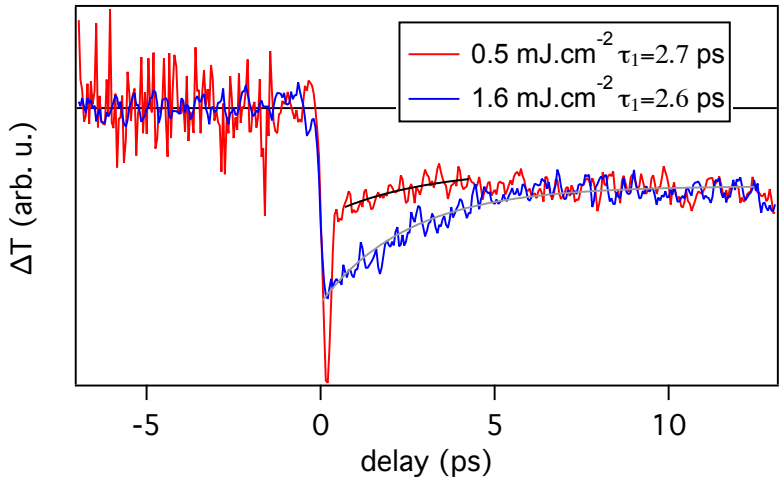

Fig. 5.4: Time-resolved variation of the transmission in $(V_{1-x}Cr_x)_2O_3$ (x=0.011) at 300 K (PI phase). The negative sign means that there are more free carriers due to heat or a metallization. The first relaxation time could be related to the phonon hardening seen with optical reflectivity.

5.2 Time-resolved ARPES study of V_2O_3

We now look at the measurements done with time-resolved ARPES, which is the most direct method to probe the electronic structure. The entire phase diagram was investigated at 200 K and 300 K. The probed points in the phase diagram are represented in Fig.5.5. The aim of this study was to understand the fast initial electronic response of V_2O_3 and the effect of the phonon hardening on the electronic structure. The comparison inside the same phase was carried out to disentangle the temperature effect from the phase specific response.

All the bulk samples were oriented along the hexagonal c direction and cleaved in situ. The c direction was always kept towards the analyzer. The surface is very robust to contamination and can last 2 days in a vacuum of 10^{-10} mbar. Unfortunately the bulk material is very hard to cleave correctly and the surfaces presented many defects. Multiphoton photoemission is amplified by surface defects, thus preventing high fluence pumping. Most of the measurements were done under 2 mJ/cm^2 and no significant heat accumulation was seen since the pump spot size is very small and the sample touched large parts of copper. The cross section of V_2O_3 is very poor at 6.3 eV and the time-resolved signal very small. Very long acquisition time were needed to acquire enough statistics. For the sake of grasping the data quality, most of the spectra are presented without any smoothing technique in order to allow the reader to make his own opinion on whether the differences seen are significant or not.

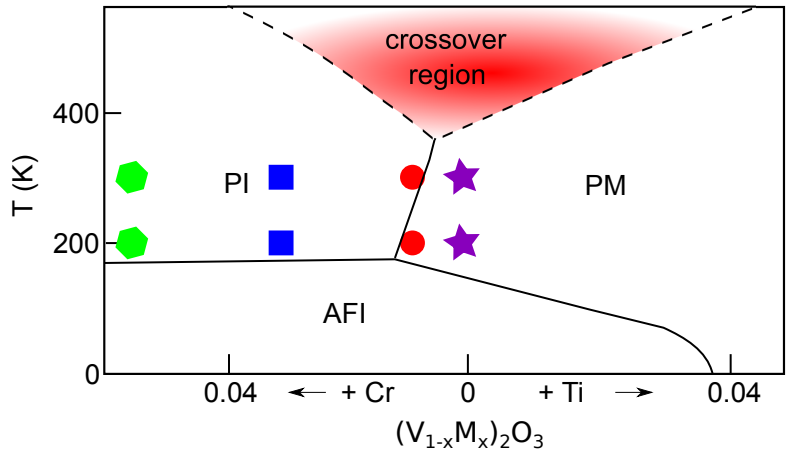

Fig. 5.5: Phase diagram of V_2O_3. The different markers represent where the measurements were done.

Fig.5.6 shows the spectra in the PI phase with the laser's 6.3 eV photons for different dopings as well as in the PM Phase. In the PI phase, all the spectra are not identical and more surprisingly the 5.6% Cr doped has a smaller gap than the 2.8 % Cr doped. The 5.6% Cr doped has a higher electric resistance than the 2.8% Cr doped [121]. The relation between the gap given by photoemission and the electric resistance is not direct since in the AFI phase the gap becomes smaller with Cr doping but the electric resistance increases [121, 129]. The dotted lines are a guide to the eye to estimate the gap and to compare to the photoinduced response of the system. In the PM phase, the lineshapes are fairly similar to the spectra in [157] at low photon energies. At these low energies the quasiparticle peak (QP), which the region between -1 eV and 0 eV of the PM spectrum, is weak. The closer the Mott transition is to the observed point, the smaller the QP. The 1.1% Cr doped has a smaller QP peak than the pure sample at 290 K or at 205 K, this is consistent with the literature [129].

V_2O_3 photoemission spectra has been proven to be very sensitive to the photon energy [127] because the bulk QP is weakened at the surface [157, 21]. The coordination number changes at the surface which changes the local electronic density. Only using high energy photons or low energy photons can the real bulk QP weight be seen because at those energies the photoemission spectra are more bulk sensitive. The photon dependence of the probed depth can be seen in Fig.3.16. Fig.5.7 shows the temperature dependence of the 2.8% Cr doped sample (PI phase) and the pure sample (PM phase). In the PM phase the QP weight increases with decreasing temperatures thus proving that the 6.3 eV probe is able to capture information about the bulk properties of the material. In the PI phase, the temperature increase fills states in the gap: this is consistent with the results from Mo

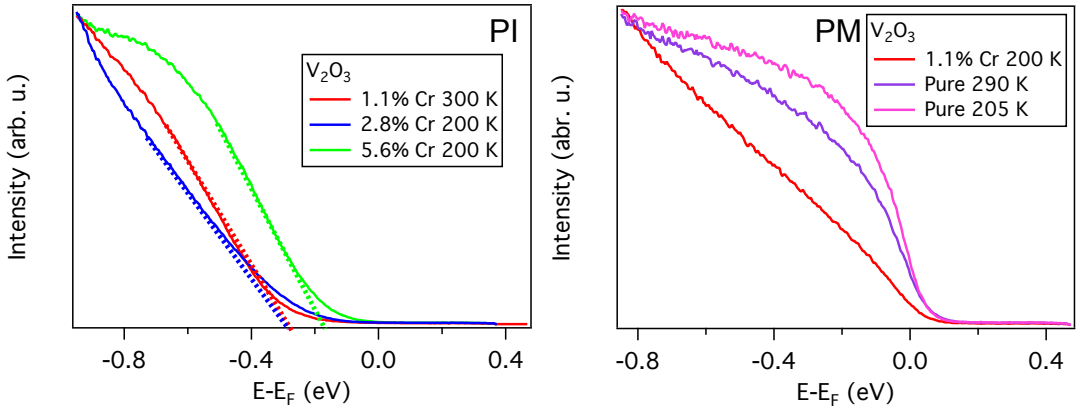

Fig. 5.6: Photoemission spectra for different dopings in the PI and PM phase. The dashed lines represent en estimation of the gap. PI phase spectra have clear gaps whereas the PM spectra have some weight near the Fermi level.

et al. [128]. The temperature spectra differences will be used to compare with the photoinduced effects.

Fig.5.8 shows the photoemission spectra for different delays in the PI phase and PM phase at a fluence of 1.8 mJ/cm^2. The differences are very small therefore the differences between negative and positive delays are shown hereafter. A negative delay was taken after each delay step to assure the correct normalization.

The differences in the PI phase can be seen in Fig.5.9. The vertical cut between -0.2 eV and 0 eV under the Fermi level shows a first peak that lasts less than 200 fs. The peak is asymmetric towards the positive delays suggesting that the time resolution barely enables to resolve the electron relaxation. The system reaches a plateau after 300 fs. The first excitation is also seen in optical reflectivity and THz spectroscopy, which is attributed to a pure electronic excitation and it's briefness demonstrates an extremely strong electron-phonon coupling. The phonon energies in the material are as high as 75 meV [188]. Since the electron-phonon coupling depends on the frequency of the phonon squared [2], materials with high energy phonons are more prone to very fast relaxation rates. The quasi steady state that is reached after 300 fs is therefore a thermalized state where the lattice and the electrons have the same temperature. In order to understand the nature of the two characteristic time scales we compare the horizontal cut at 50 fs and 400 fs with the temperature difference.

The 50 fs delay spectrum has weight under and above the Fermi level, which are in-gap states. In band insulator, in-gap states are impossible without a complete collapse of the band gap. This seems to be very different in narrow band Mott insulators. The upper part of the spectrum is flat supposing a non Fermi liquid like behavior. A Fermi liquid has a tail that decreases exponentially. Therefore

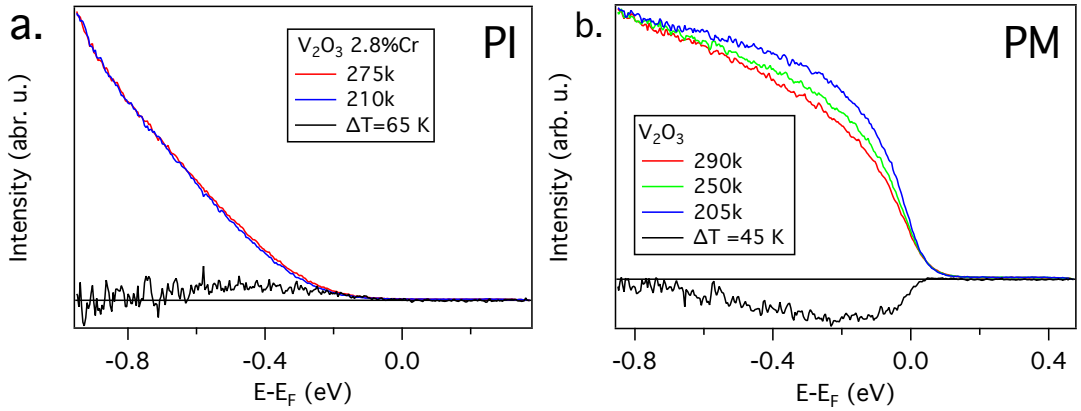

Fig. 5.7: Photoemission spectra for different temperature in the PI and PM phase. The black curve is the difference between the high temperature and the low temperature. In the PI phase, there is a filling of the gap with temperature and in the PM phase the QP increases with lowering temperature.

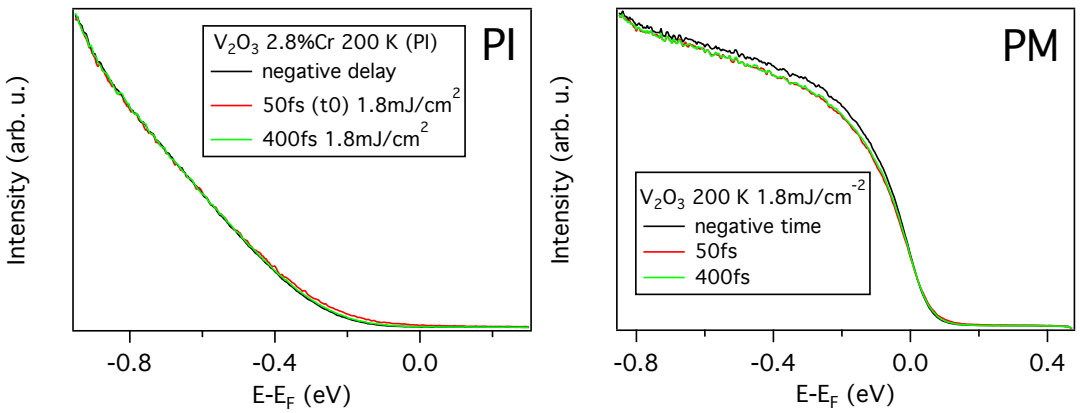

Fig. 5.8: Photoemission spectra for different delays in the PI and PM phase. In the PI phase some spectral weight can be seen in the gap at 50 fs. The QP melts in the PM phase.

at 50 fs the system is in a purely out-of-equilibrium state where an electronic temperature can not be defined. The 400 fs delay spectrum has no weight at the Fermi level which confirms the thermalized hypothesis. In order to quantify the change of the spectrum, the center of mass is calculated for the 50 fs delay, the 400 fs delay, and the temperature difference of 65 K. All three spectra are the difference between a heated or a photoinduced state with the same negative delay spectrum. The center of mass of the 50 fs spectra is -0.265 eV, for the 400 fs it is -0.277 eV, and the temperature -0.344 eV. Therefore the changes seen are different from a simple temperature increase. In order to confirm further more that the 400 fs spectrum is different from an equilibrium temperature increase, the spectra are normalized to have the maximum difference at the same level. Fig.5.10 shows the photoemission spectra differences for the 2.8% Cr and 5.6% Cr doped at 200 K. There is a slight difference near the Fermi energy for both dopings between the equilibrium temperature difference and the 400 fs delay. This difference might be induced by the phonon hardening phenomenon.

The same analysis can be done in the PM phase using the pure sample. Fig.5.11 shows the photoemission spectra differences versus delay. Two vertical cuts can be done, above and under the Fermi level. The time trace above the Fermi level tracks the excited electrons and is very similar to the dynamics seen in the PI phase, with an initial peak that relaxes to a thermalized state. On the other hand the time trace under the Fermi level tracks the QP peak. There is an ultrafast melting of the QP, which partly recovers after 100 fs. Afterwards it vanishes again and reaches a plateau after 300 fs. This clearly indicates two distinct mechanisms of the QP melting. One that arises when the system is in a completely out-of-equilibrium state and another that is slower. The QP is very sensitive to the distance to the Mott transition. Mo et al. showed that at 200 K the spectrum of the pure sample has the highest QP peak compared to a Cr doped or Ti doped samples [129]. The temperature also effects the QP as seen in Fig.5.7. The comparison of the spectra at 50 fs and 400 fs delay with the temperature shows a similar trend as in the PI phase. The 50 fs spectrum has significantly more hot electrons than the temperature difference and these electrons also do not present any exponential decrease in energy. The 400 fs does have an exponential decrease but still has much more weight above the Fermi level than the temperature difference. The main question is whether these are long lived excited QP electrons or a change in the spectral function.

We now compare the spectra inside the same phase. Only the 50 fs and the 400 fs spectra will be compared because all the time traces have the same dynamics and no interesting information can be extracted from them. We have seen that the equilibrium spectra inside the same phase are different. Therefore when comparing the spectra, one has to keep in mind that the gaps and the QP are different. A

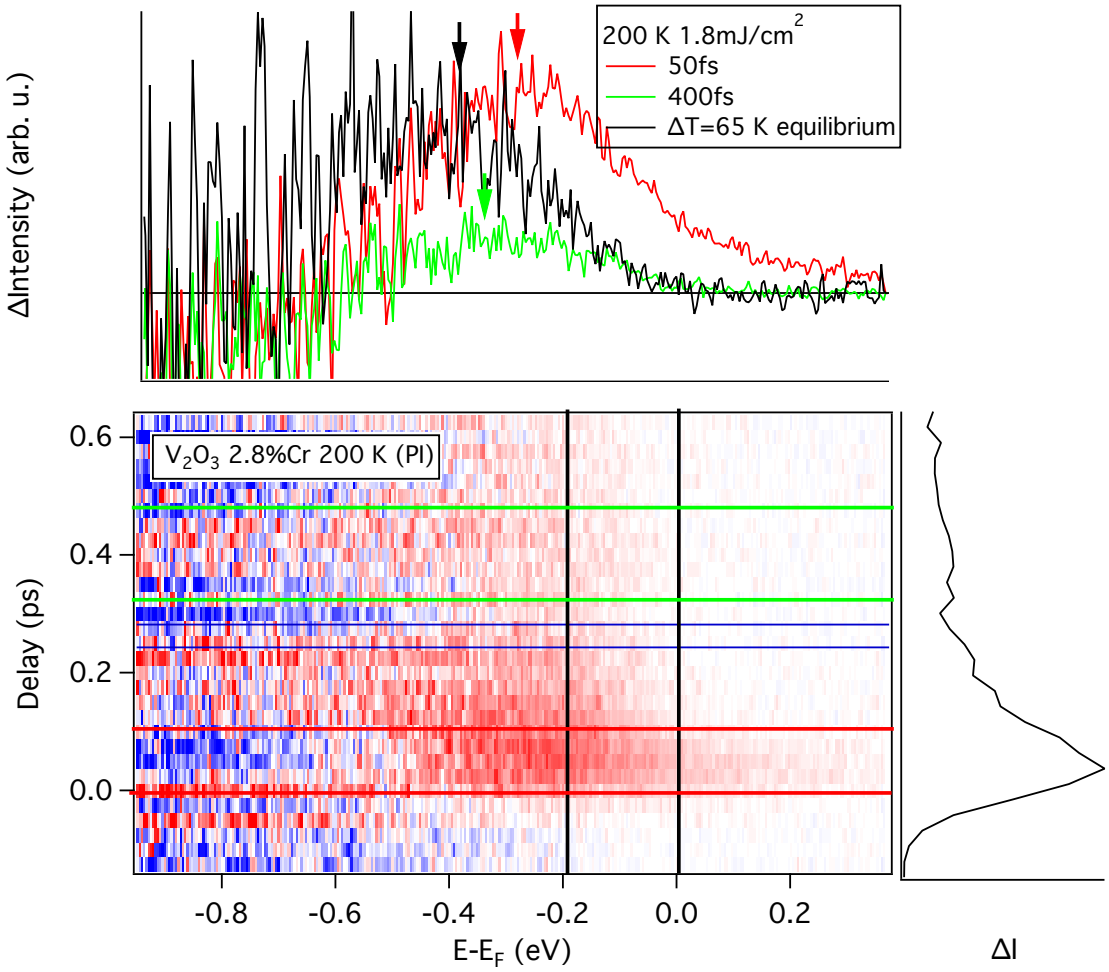

Fig. 5.9: Photoemission spectra differences versus delay in the PI phase. The arrows represent the center of mass of the spectrum. In-gap states appear that are different from an equilibrium temperature increase.

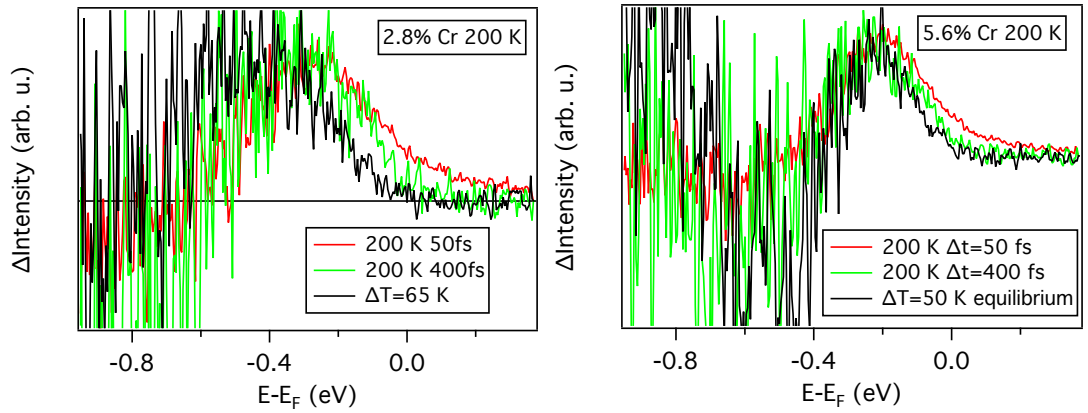

Fig. 5.10: Photoemission spectra differences for 2.8% Cr and 5.6% Cr doped at 200 K. The comparison with an equilibrium heated difference show that for both the 2.8% Cr and the 5.6% Cr non thermal in-gap states appear around -0.1 eV.

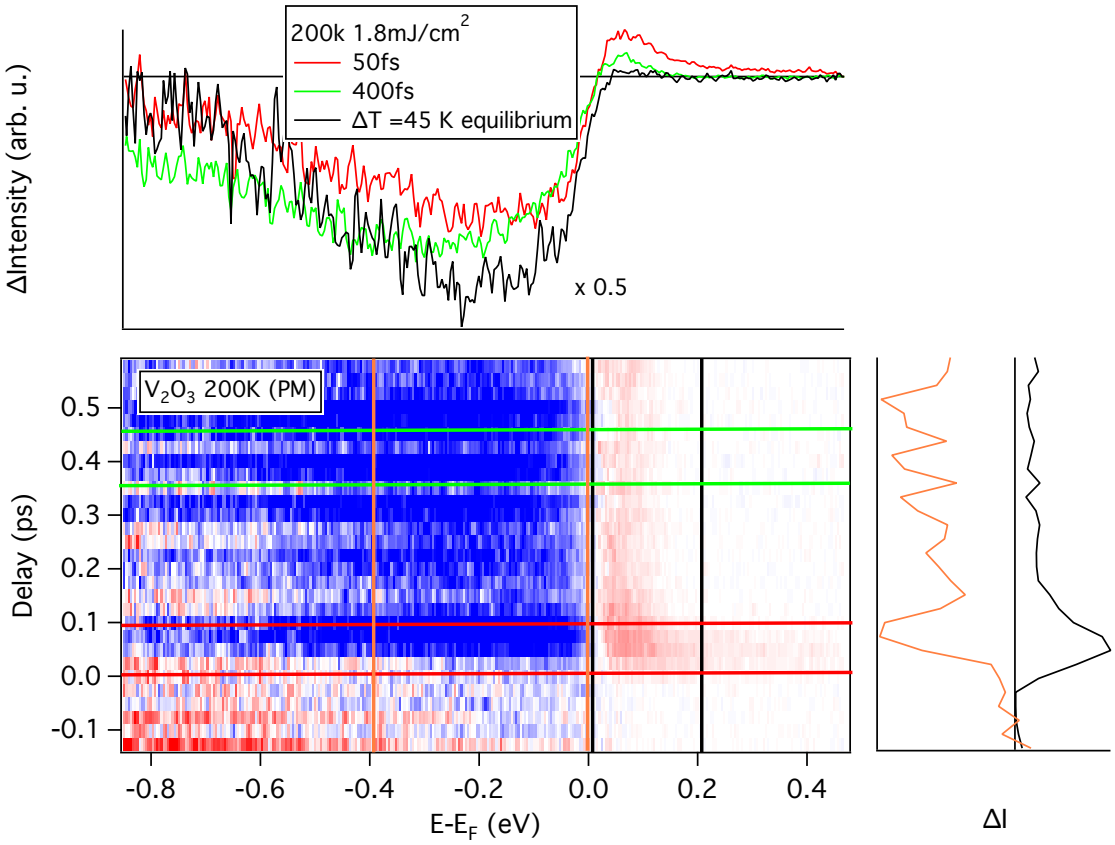

Fig. 5.11: Photoemission spectra differences versus delay in the PM phase. The dynamics are the same as in the PI phase. The QP melts faster than the time resolution. The hot electrons thermalize in 200 fs.

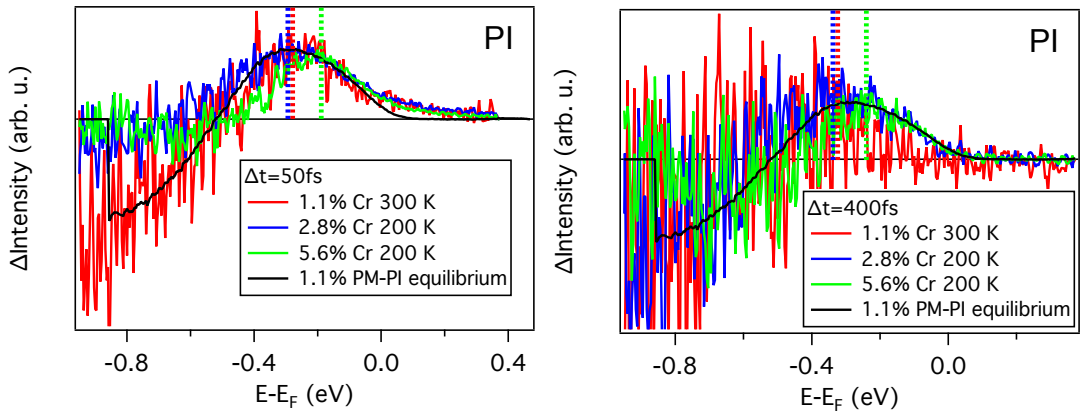

Fig. 5.12: Photoemission spectra differences for different dopings in the PI phase for a delay of 50 fs and 400 fs. The photoinduced difference are very similar to the difference during the phase transition for the 1.1% Cr doping.

comparison between different dopings of the occupied states is difficult for that reason. Fig.5.12 shows the spectra for the 50 fs delay and the 400 fs delay for 1.1% Cr, 2.8% Cr, and 5.6% Cr dopings in the PI phase. The dashed lines show where the equilibrium gaps are. We notice that above the gaps all the spectra have the same behavior suggesting a universal property in the PI phase. The 1.1% Cr doped sample crosses the Mott transition with temperature. The equilibrium difference for the 1.1% Cr doped sample between the PI and the PM phase is plotted above the 50 fs delay spectra. The photoinduced response of 1.1% Cr doped sample and its equilibrium difference are very similar, suggesting that the photoinduced material in the PI phase is more metallic than at equilibrium. Of course the hot electrons quantity does differ between the two spectra because of its out-of-equilibrium distribution.

In the PM phase, the QP varies significantly therefore the loss of spectral weight with the pump pulse differs as seen in Fig.5.13. The 1.1% Cr, the pure compound at 300 K, and at 200 K have more and more QP weight and lose proportionally. At 400 fs delay the lineshape of the pure compound sprectrum at 200 K is different from the 300 K spectrum maybe reflecting the presence of a more pronounce QP. The behavior above the Fermi levels is very similar for the 3 points. The 50 fs delay has a non Fermi liquid like trend and the 400 fs delay is more thermalized.

The fluence dependence was investigated to understand the nature of the changes seen. The lineshape does not change with fluence at 50 fs nor at 400 fs as seen in Fig.5.14. The other samples have similar behavior. To quantify better this change we integrate the spectra differences in the gap in the PI phase and above the Fermi level in the PM phase. The integrated intensity change versus fluence is plotted in Fig.5.15. The fluence range studied is fairly small since we are limited

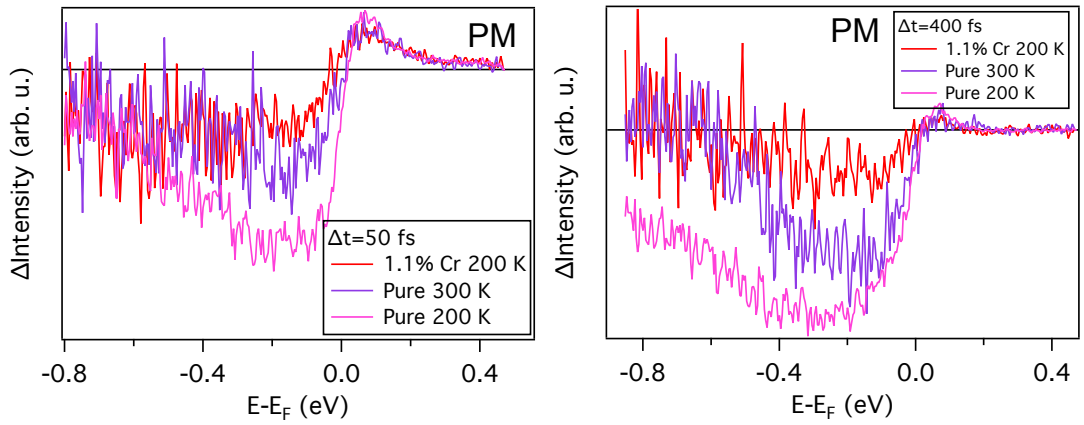

Fig. 5.13: Photoemission spectra differences for different dopings in the PM phase for a delay of 50 fs and 400 fs. The hot electron differences are very similar for all doping and temperature but the loss of QP is different, which can be explained by the fact that the QP is different for all the different temperature and doping.

by the noise level in the low fluences and by the multiphoton effects for higher fluences. However the linear behavior is clearly visible. This indicates that for the fluences used the system is in the linear regime. The fact that the lineshape stays the same for all the fluences for 50 fs and 400 fs supposes a non Fermi liquid like behavior even for the PM phase because an increase of temperature in a Fermi liquid renders different lineshape where the maximum of the difference is shifted to higher energies when the temperature is increased. A linear mechanism could be domain formation that are affected by the pump pulse. Each domain could have different transition threshold that is obtained with different fluences.

We have seen the fluence dependence of the hot electrons. Now we turn to the fluence dependence of the QP loss in the PM phase. Fig.5.16 shows the integrated loss under the Fermi energy for 300 K and 200 K for the pure compound. At 300 K the loss is linear and the 400 fs delay loses less weight than at 50 fs. It is the opposite at 200 K, the 400 fs spectra loses more QP weight than for 50 fs. Moreover the fluence dependence is non linear, which is challenging to interpreted since the QP weight versus temperature is a non linear function as seen in Fig.5.7 or theoretically in [150]. The higher loss of QP weight at 400 fs than at 50 fs is another proof of the two different mechanisms that occur at 50 fs and 400 fs as illustrated in the time trace of Fig.5.11.

The 1.1% Cr doped sample has the same behavior as the other points in the same phases whether it is in the PI phase or in the PM phase. When inside the hysteresis, the sample also switched to insulator when the fluence was increased similar to what was observed with THz spectroscopy with heat accumulation.

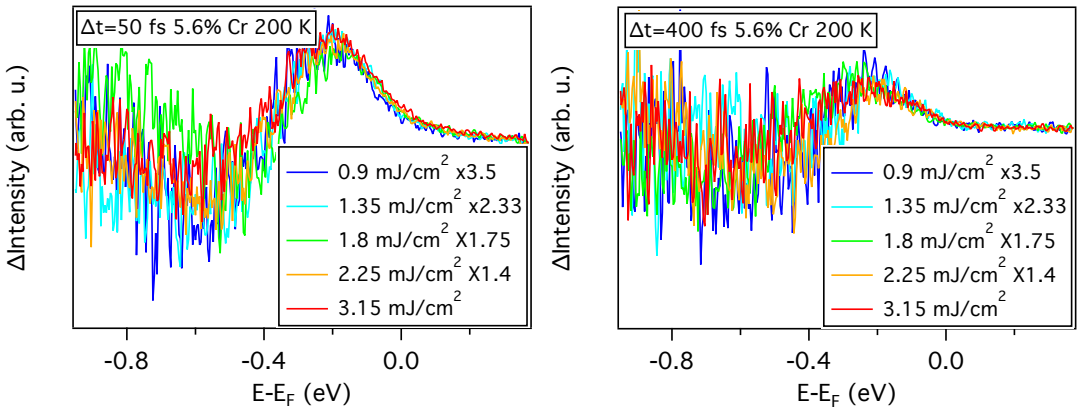

Fig. 5.14: Fluence dependence of the photoemission spectrum difference for 50 fs and 400 fs delay. The differences are perfectly linear with fluence in the PI phase.

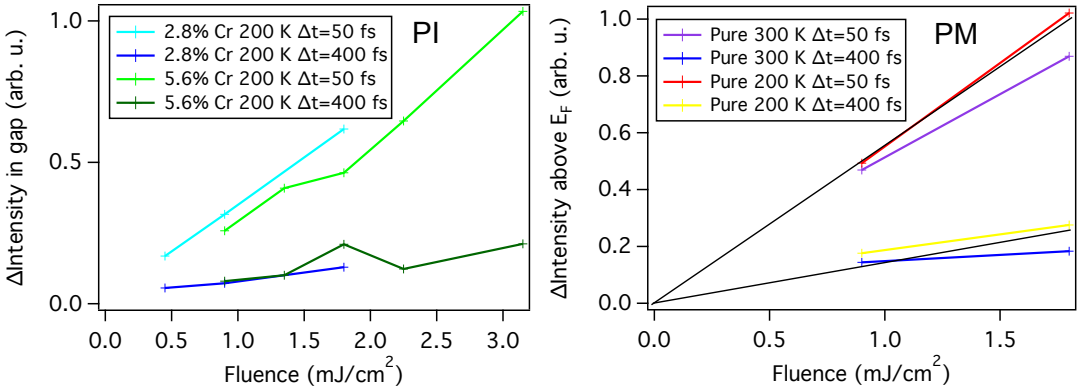

Fig. 5.15: Fluence dependence of the integrated photoemission difference in the PI and PM phase. The intensity was integrated in the estimated gap in the PI phase and above the Fermi level for the PM phase. All the fluence dependences of the hot electrons are linear with fluence.

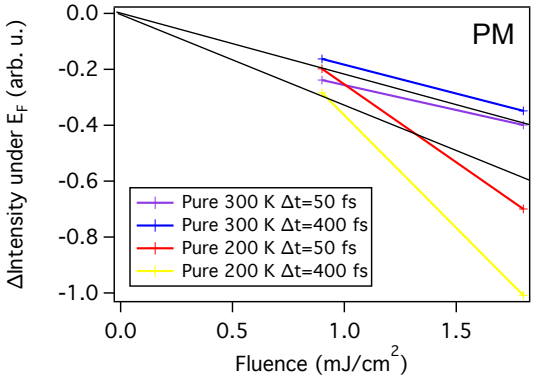

Fig. 5.16: Fluence dependence of the integrated photoemission difference under the Fermi level for the PM phase. The effect on the QP is not linear with fluence at 200 K.

Outside the hysteresis the switching was not observed because the fluence used in tr-ARPES was too low. Nevertheless the time-resolved behavior was similar to the pure compound suggesting that no purely electronic phase transition was seen.

We have proven that at 400 fs the spectra in the PI phase are different from a thermal state. The question is how long does this non thermal state lasts. We performed long time scans to observe the evolution of this state. Fig.5.17 and Fig.5.18 show spectra for longer delays for the 2.8% Cr doped and the 5.6% Cr doped samples. The time scans near -0.1 eV show a relaxation that is completely finished after 2 ps. The spectra shift towards lower energies that are closer to the equilibrium thermal difference. Interestingly the intensity difference does not change after 500 fs but only the position. This supposes that the number of excited electrons is constant. The time scans show two relaxation rates one is around 70 fs, which corresponds to the relaxation of hot electrons while the other is longer. For the 2.8% Cr doped sample the second timescale is 1.7 ps which is longer than the observation of the phonon hardening. For the 5.6 % Cr doped sample the second timescale is 370 fs, much shorter than for the 2.8% Cr doped. This discrepancy might be due to the fact that the gaps are different. The smaller the gap the faster the relaxation. These relaxations towards the equilibrium thermal spectra is surely linked to the end of the phonon hardening effect.

In this chapter we have seen that a photo switching to an insulator is possible from a metallic phase. The mechanism involved is surely due to heat accumulation but could be done using a single high fluence laser pulse. The time-resolved ARPES proved a universal behavior of the material in the whole PI phase. During the first 100 fs, a complete out-of-equilibrium phase exists with in-gap states, which relax to a thermalized state that is different from a temperature increase. The effects are linear in fluence. In the PM phase a similar dynamic exists: the QP presents

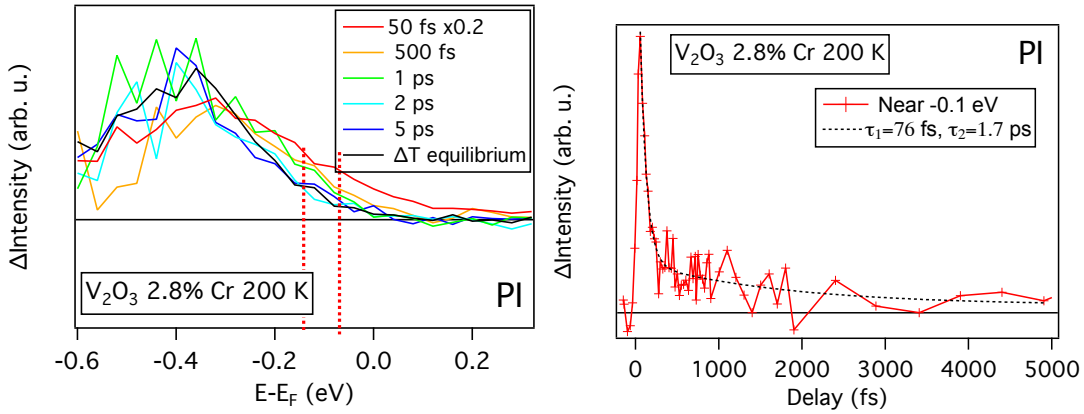

Fig. 5.17: Photoemission spectra differences for different delays for a 2.8% Cr doped sample. Time scan integrated near -0.1 eV. The two relaxation times correspond respectively to the relaxation of the hot electrons and to the relaxation of the non-thermal state.

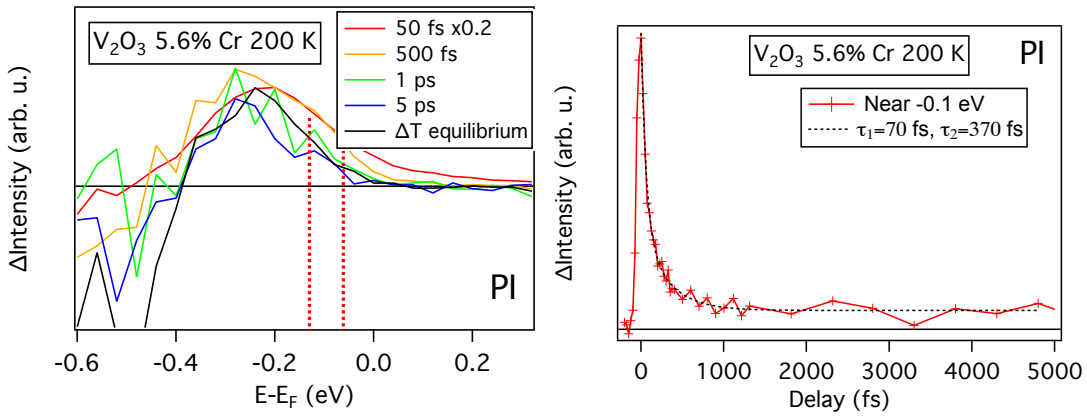

Fig. 5.18: Photoemission spectra differences for different delays for a 5.6% Cr doped sample. Time scan integrated near -0.1 eV. The two relaxation are similar to the 2.8% Cr doped sample

an ultrafast melting that partly recovers and then disappears again. The melting of the QP is non linear at 200 K but linear at 300 K. The hot electrons on the other hand present a perfectly linear behavior. The non-thermal state lasts less than 2 ps in the PI state thus giving a relaxation time for the phonon hardening phenomenon. We will analyze the physical meaning of these observations in the next chapter.

5.3 Time-resolved ARPES study of $BaCo_{1-x}Ni_xS_2$

Time-resolved ARPES was carried out on $BaCo_{1-x}Ni_xS_2$ for x=1 and x=0. The dynamics of the two compounds were compared in order explore the difference between the metal and the Mott insulating phases. This study is really a textbook case, since the metal compound has rather small correlations and the Mott insulator is very correlated. The correlation range investigated for this compound is much larger than the correlation range investigated for V_2O_3. I will first present the metal then the insulator.

Fig.5.19 shows the time-resolved measurements on $BaNiS_2$ using a s polarization. The equilibrium spectrum is taken along the ΓM direction and is very similar to the synchrotron band dispersion seen in Fig.1.13. The reciprocal region seen using 6 eV photons is small. The broadening of the bands comes from the limited energy resolution due to the Fourier limited laser pulse, which is about 60 meV. Near the Γ point, $BaNiS_2$ has two active bands, similar to V_2O_3.

In the time-resolved image, one can define two regions of interest: the valence band V1 and the conduction band C1. These two regions are both d_{xz}/d_{yz} orbital. The time trace of these regions are plotted in Fig.5.20. The two regions have similar dynamics with a time constant of about 600 fs. The time traces have a standard metallic behavior, which is typical of a Fermi liquid that cools down. Compared to the metallic phase of V_2O_3, the dynamics are much slower. We can use the two temperature model framework to understand the dynamic. The Eliashberg coupling constant varies as the square of the phonon energy. Therefore the slower dynamic can be explained by the less energetic phonons in $BaNiS_2$ than in V_2O_3. The phonon in V_2O_3 are as high at 75 meV whereas in $BaNiS_2$ they are as high as 45 meV [207]. Compared to the PM phase of V_2O_3, the hot electrons do not present two time constants and no quasiparticle can be tracked in $BaNiS_2$. These differences really show that $BaNiS_2$ is much closer to a normal metal than V_2O_3.

The Mott insulator $BaCoS_2$ does not present any significant dispersion around the Γ point. Therefore we integrate the spectrum between -0.1 and 0.1 $\mathring{A}^{-1}$. Fig.5.21 shows the comparison between the laser spectra at 300 K and 120 K and the spectrum at 140 K taken with Synchrotron radiation. The laser spectra

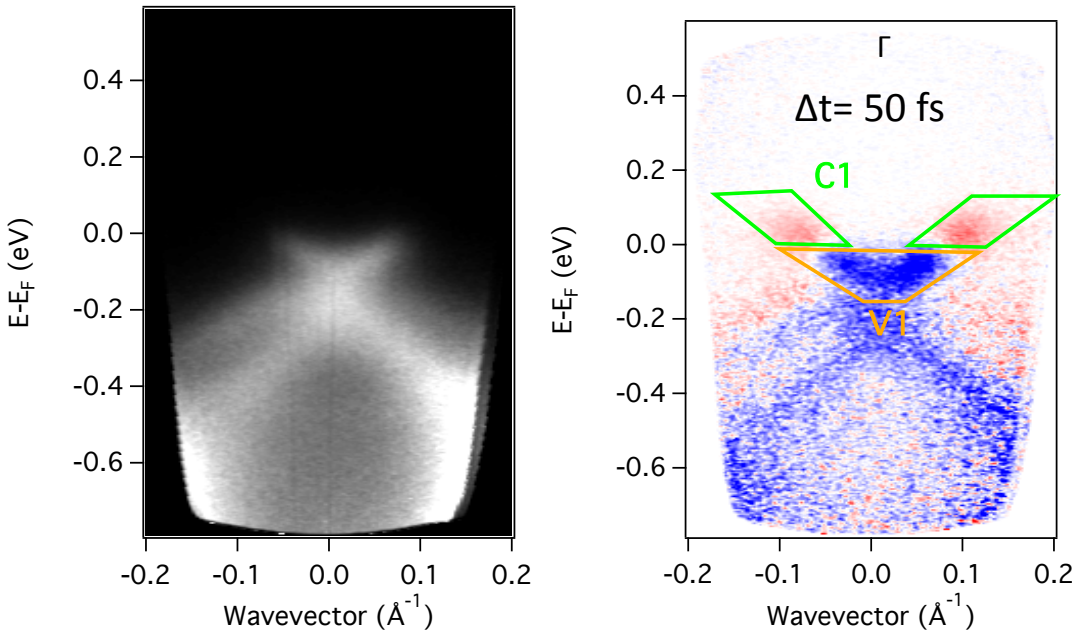

Fig. 5.19: Equilibrium ARPES measurements on $BaNiS_2$ using the 6 eV laser pulse near the Γ point. Time-resolved ARPES measurements, blue meaning less electrons and red more electrons. The regions of interest are taken on either side of the Fermi energy: V1 is the intensity under the Fermi energy and C1 is the one above.

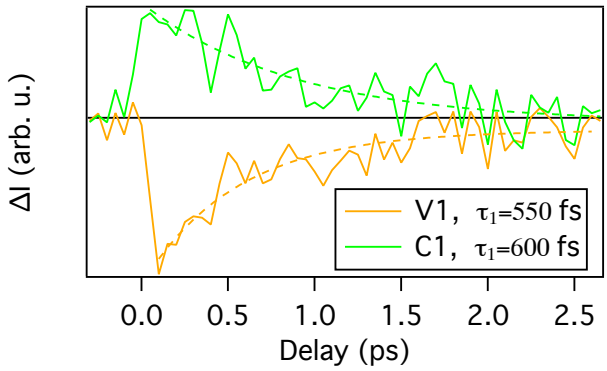

Fig. 5.20: Time evolution for the electrons on either side of the Fermi level. Both dynamics are similar and are typical of a heated metal, first heated and then cooled down.

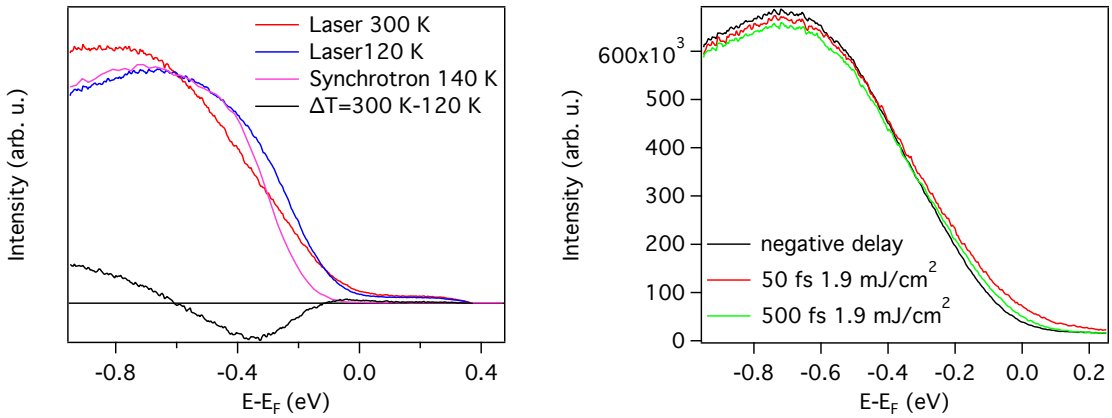

Fig. 5.21: Photoemission spectra near Γ for $BaCoS_2$ using laser and synchrotron. Spectra for different delay times. The laser spectra are similar to the Synchrotron spectra. The photoexcited spectra show in-gap states.

are larger due to the lower energy resolution of the pulsed laser ARPES. The temperature difference shows a spectral weight transfer from -0.4 eV to -0.8 eV and more electrons near the Fermi level when raising the temperature. The spectra at various delays show a spectral weight transfer from -0.8 eV to energies near the Fermi level.

We now look at the differences between the positive time delays and a negative one. Fig.5.22 shows the time-resolved measurements on $BaCoS_2$. The spectrum at 50 fs has many hot electrons above the Fermi level whereas at 500 fs many of those electrons have disappeared. Under -0.4 eV the spectra at 50 fs and 500 fs are very similar. The time-resolved spectra are completely different from the equilibrium temperature difference. Therefore the state created by the laser pulse is a new out-of-equilibrium state that is not attainable at equilibrium. Similar to V_2O_3, states are created in-gap pointing towards a collapse of the gap with photoexcitation.

The time trace of Fig.5.22 at different energies show slower dynamics with lower energies. The fastest dynamics are the hot electrons above 0.2 eV, that relax with a time constant of 60 fs. The electrons between 0 and 0.2 eV have a time constant of 225 fs, which is much faster than for the metallic compound. The two temperature model can not be applied to this material since it is an insulator. However the comparison with the metallic compound can be done in a qualitative view. The phonon energy is the same as for the metallic compound therefore the faster dynamics suggest a stronger electron-phonon coupling. The electrons that are under the Fermi level are much slower and have a time constant of 1.4 ps, which is even slower than the holes in metallic compound $BaNiS_2$. This time constant

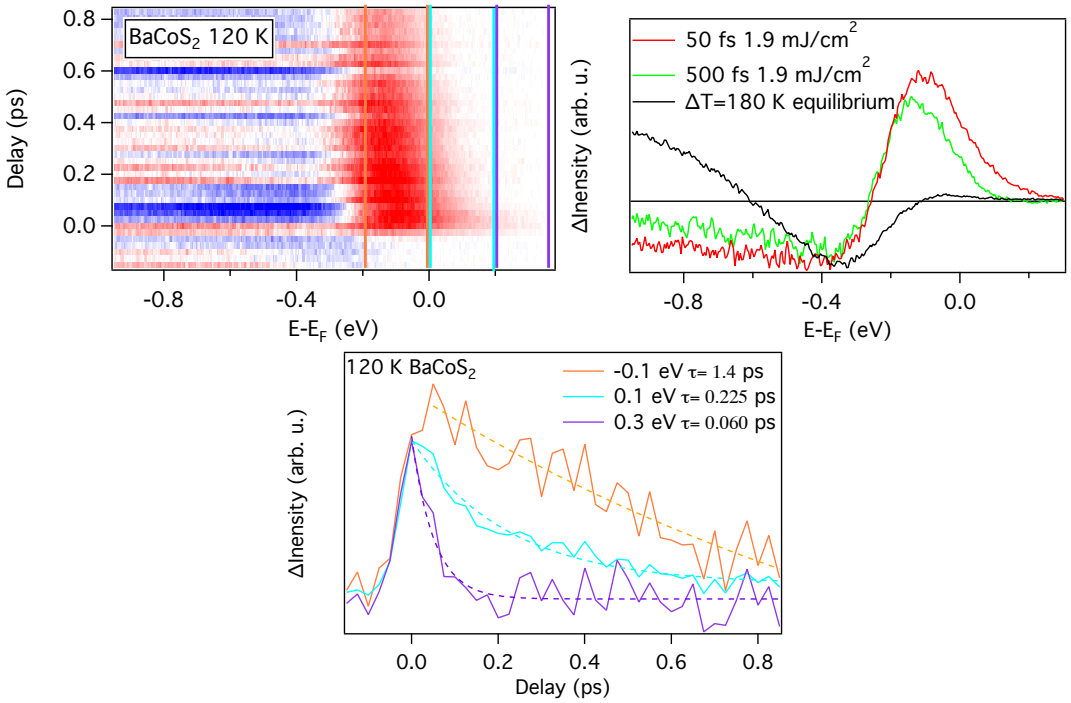

Fig. 5.22: Time-resolved ARPES measurements on $BaCoS_2$. The spectra differences at 50 fs and 500 fs show in-gap states different from an equilibrium temperature increase. The time scans show that the dynamics are fast above the Fermi level and much lower under.

can be compared to the non-thermal state seen in the PI phase of V_2O_3, which is 1.7 ps for the 2.8% Cr doping.

We have shown that $BaNiS_2$ behaves like a normal metal different from the PM phase of V_2O_3. However $BaCoS_2$ has a behavior much closer to the PI phase of V_2O_3: fast relaxation of the electrons above the Fermi energy, and in-gap states are created, which is a non-thermal behavior. The faster dynamics above the Fermi level of $BaCoS_2$ compared to $BaNiS_2$ suggest a stronger electron-phonon coupling in the insulating compound.

The two Mott insulators, V_2O_3 and $BaCoS_2$, point towards some common and general trends of Mott insulators: fast relaxation of electrons above the Fermi level, much slower electron dynamics under the Fermi level, and in-gap states are created in a non-thermal manner. These specific behaviors will be discussed in the next chapter.

Chapter 6

Discussion

Tracking the lattice and the electrons separately provides a fundamental insight on the electron-phonon coupling. How does the lattice affect the electronic structure or vice versa? We have probed the lattice using time-resolved optical reflectivity and time-resolved X-ray diffraction. The electrons were probed using time-resolved THz spectroscopy and time-resolved ARPES. The experimental observations are summarized in Fig.6.1 for V_2O_3.

During the first few hundreds ps a shock wave propagates through the sample. The starting point of this shock wave could not be observed with tr-XRD, due to insufficient time resolution, but it most likely starts with the relaxation of the electrons to the lattice at around 100 fs, which may be the beginning of an acoustic wave related to the c/a deformation. After this shock wave the system reaches a spatially homogeneous thermal state that corresponds to an increase of temperature of 20 K for 5 mJ/cm^2. On shorter time scales, a hardening of the A_{1g} phonon is seen. Its maximum happens when the pump propagation vector is parallel to the c axis. This hardening is associated with the populating by the pump pulse of the a_{1g} orbital that is bonding, and reduces the V_1-V_4 distance. The observation of the phonon only lasts for 1.5 ps because of the strong coherent phonon damping. The X-ray diffraction measurements have a resolution of 100 ps therefore the lifetime of this structural hardening was not clearly identified but it certainly lasts less than 1 ns. Since the electronic structure is very sensitive to the trigonal distortion, the shortening of the V_1-V_4 distance would possibly have an important impact on the electronic density of states.

The excited electrons in the PI phase and the PM phase have the same dynamics. An out-of-equilibrium distribution is present during the first 200 fs and then the electrons thermalize. In the PI phase, this is associated with in-gap states for the first 200 fs and a state different from a purely heated state in the thermalized time window. In the PM phase, the QP melts, partly recovers and remelts in the

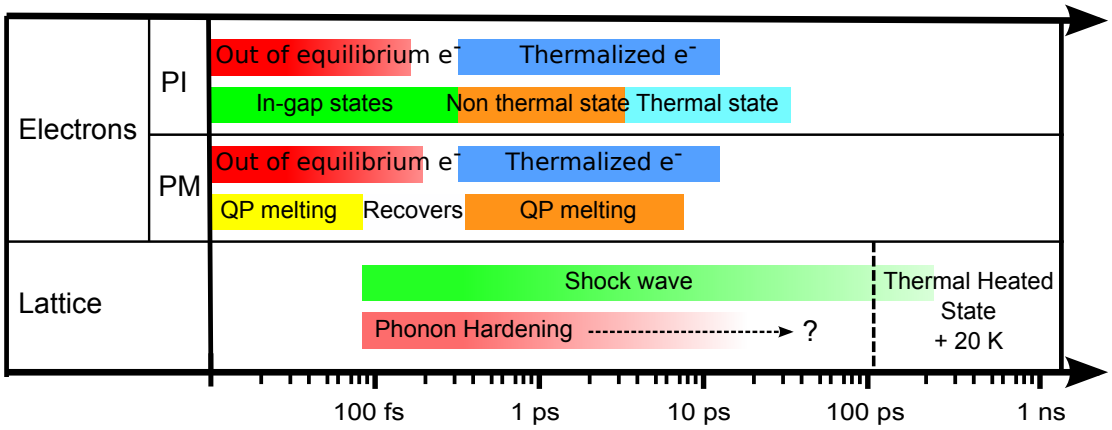

Fig. 6.1: Experimental observations in V_2O_3 using different pump-probe techniques.

thermalized time window. The two meltings are different and are most likely the result of two different mechanisms. The quantity of electrons above the Fermi level is different in the thermalized region than for an equilibrium heated state. The long dynamic of this non-thermal state was observed in the PI phase and suggests a relaxation towards the equilibrium heated state after 2 ps.

When comparing the different experimental observations, a number of questions arises. For the lattice, is the shock wave a consequence, a cause, or completely independent from the phonon hardening? Does the similar dynamics in the PM phase and PI phase correspond to the same physical phenomenon? What is the origin of the first out-of-equilibrium electronic state? Is the phonon hardening responsible for the non-thermal electronic state observed after 200 fs? Does the crystal structure relax the same way as the electronic structure? The last question concerns the linear or nonlinear fluence behavior of the excited states. I will try to answer these questions one by one.

Because of the low time resolution of time-resolved X-ray diffraction, the phonon hardening was not observed directly. However the shock wave has its origins in acoustic phonons that creates a quasishear wave as reported in [110, 114]. These phonons are much slower than the optical A_{1g} phonons. Our tr-Xrd results present anomalous behavior which may be related to the lattice deformation associated with the A_{1g} phonon hardening. The pump laser only excites part of the sample, thus creating a strain gradient that triggers the shock wave. Since the crystal is anisotropic the acoustic phonons propagate differently according to the crystal's directions [114, 115].

The dynamics of the PM phase and PI phase present many similarities and they both can be described using the Hubbard model or the Hubbard-Holstein

model. The origin of the observations are most likely due to the same physical parameter change. Therefore a model has to be able to account for both the PI and the PM phase using the same description. The parameters that can vary are the electronic temperature T_e, the lattice temperature T_L, the Coulomb repulsion with its screening U_{eff}, the bandwidth W, the electron-phonon coupling λ, and the orbital specific filling.

During the first 100 fs the lattice most likely has not moved therefore the bandwidth can not have changed. The photoemission spectra before 100 fs are very different from a heated equilibrium spectra thus indicating that a raise of T_e can not account for these changes. After the photoexcitation the average electron energy has increased. However the energy distribution does not follow a Fermi-Dirac distribution and therefore we can not define an electronic temperature. The fluence independence of the lineshape confirms this. Experimentally in-gap states are seen in the PI phase and a QP melting in the PM phase. In the PI phase there is no dependence on the distance to the Mott transition nor to the crossover region. The photoemission spectra differences are very similar to the phase transition between the PI and PM phase. A change of the Coulomb screening would lead to a new U_{eff} and the changes should be more significant closer to the Mott transition but this is not the case. The behavior is similar for the entire PI phase. Exciting an electron creates a hole in the valence band thus enabling its neighbors to hop to this site creating free carriers. Changing the filling of the valence band moves it away from the half filled Hubbard model which leads to the collapse of the gap in the PI phase and loss of coherence in the PM phase. The new state does not correspond to any equilibrium points in the phase diagram since the phase diagram is for the half filled bands. In V_2O_3, the excited electrons are excited to the a_{1g} orbital therefore there is a real change of the specific orbital filling of the e_g orbitals and the a_{1g} orbital. This effect should be general in all narrow band Mott insulators with two bands, which is generally the case in most Mott insulators. The same in-gap states are seen in VO_2 and in TaS_2 [200, 146]. On the opposite, larger band gap insulators such as UO_2 do not present a collapse of the gap since the gap is much more robust and can be seen more as band insulator. Cuprates present a change of the band filling, that is directly seen by a hole doping [152]. The laser excitation creates holes and therefore the transition is a filling controlled phase transition as seen in Fig.1.3.

As seen in the PM phase the first state relaxes very fast and another state appears after 300 fs. In both the PI phase and the PM phase, the electrons are thermalized. However this thermalized state is different from a heated equilibrium state, in the PI phase the difference is shifted to higher energies and in the PM phase electrons are still present above the Fermi level. The phonon hardening is seen starting 200 fs, the c/a ratio is reduced. A reduction of the V_1-V_4 distance

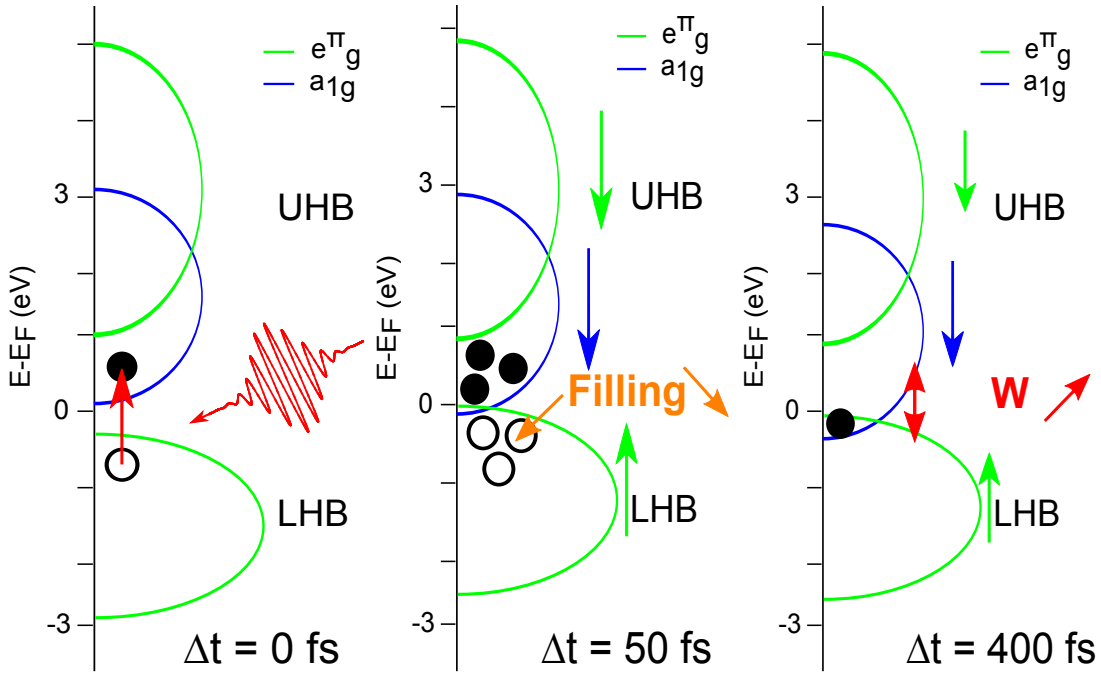

Fig. 6.2: Scheme of the proposed mechanisms happening after a photoexcitation. The pump laser excites electrons from the e_g orbitals to the bonding a_{1g} orbital. At short time delay the filling of the orbitals changes inducing a closure of the gap. On longer timescales, the electrons in the bonding a_{1g} orbital induce a phonon hardening that increases the bandwidth of the system, thus inducing a non-thermal state.

would increase the a_{1g} orbital overlap between the two vanadium atoms thus increasing the bandwidth. An increase of the bandwidth would induce a change of the electronic structure by lowering the a_{1g} and e_g orbitals in energy. The DFT calculations show this effect, see supplementary material of [117]. The change in the spectra seen in the PI phase and PM phase qualitatively agrees. We have proven that populating bonding orbitals changes the lattice structure that induces an electronic structure change. Fig.6.2 shows a scheme of the proposed mechanism. The laser pulse excites electrons to the a_{1g} orbital, which changes the specific filling of the orbitals. My results indicate that the change of the filling makes the gap collapse in the PI phase and induces a loss of coherence in the PM phase. Afterwards the V_1-V_4 distance is reduced because of the populated a_{1g} orbitals, which increases the bandwidth hence changes the density of state, pushing the material towards the PM phase.

The relaxation of the non thermal state seen using tr-ARPES takes about τ=1.7 ps whereas the relaxation time in the time-resolved THz spectroscopy is about

τ=2.7 ps. The main difference between the THz and the tr-ARPES experiment is the thickness probed. The surface might have a different relaxation time than the bulk material: the strain are easier to relax at the surface. However the time constants in both experiments are in the same order of magnitude. The experimental changes seen in the photoemission spectra are very close to what is expected from reducing the V_1-V_4 distance therefore a relaxation of this difference should also be accompanied by a relaxation of the lattice. Although the electronic structure relaxation strongly suggests that the lattice has also relaxed, the experimental observation of this relaxation has not yet been seen.

In the time-resolved ARPES experiments, the lineshape and the intensity differences of the PI phase are linear with fluence. Although the linear intensity behavior is expected, the lineshape linearity is more surprising. During the PI-PM phase transition with temperature, metallic domains are formed inside an insulating matrix [113]. Similarly, the filling can vary spatially and causes electronic domains to form since the photons are absorbed locally. In the PI phase, the number of domains is linear with fluence. In the PM phase, the electrons above the Fermi energy are also linear, while the QP melting is non linear. This non linearity of the melting of the QP is surely linked to the coherence length of the a_{1g} and the e_g orbitals. Further investigation are needed to understand the dynamics of the coherence lengths of the a_{1g} and the e_g orbitals versus temperature and fluence.

The comparison of the PI phase of V_2O_3 and $BaCoS_2$ have pointed out a few general trends of Mott insulators:
- Fast relaxation of electrons above the Fermi level
- In-gap states are created
- Non-thermal states lasting a few picoseconds
- Fluence linearity

$BaCoS_2$ and V_2O_3 have two bands near the Fermi energy, with a gap that is formed between two different orbitals. Therefore the valence and the conduction bands have two different orbital characters. The pump pulse excites electrons from one orbital to another thus changes the orbital specific filling. Since the electron-phonon coupling in these materials is very strong, populating a bonding or an antibonding orbital can change the lattice structure, as seen in V_2O_3. The lattice change stabilizes the new electronic structure by lowering under the Fermi level the energy of the newly occupied orbital. The electrons above the Fermi level relax quickly while the electrons in the newly occupied state take a few picoseconds to relax. The second relaxation time is surely due to the lattice relaxation. The fluence linearity points towards local change of the filling.

A recent theoretical calculation using time-dependent Gutzwiller approximation in a two band Hubbard model has found that populating the higher orbital leads to a gap-collapse [169]. Their model shows that a quasi-stable state arises after

photoexcitation, which is very similar to what we have observed. However the model used does not have any relaxation pathways nor a coupling to the lattice structure, therefore the stabilization of this non-thermal state is not discussed. Nevertheless this model is very promising for future development and agrees well with the experimental observation.

Conclusions and outlook

In this thesis I have used ultrafast time-resolved experiments to investigate the electronic response of Mott materials, V_2O_3 and $BaCo_{1-x}Ni_xS_2$. The whole phase diagram was explored to distinguish the phase specificity from the thermal response. Before the reaction of the lattice, the photoexcitation changes the orbital specific filling creating in-gap states in the PI phase. The hot electrons relax in less than 200 fs because of the strong electron-phonon coupling. However a non-thermal state survives for a few picosecond.

Combining time-resolved optical reflectivity, time-resolved X-ray diffraction, time-resolved Thz spectroscopy, and time-resolved ARPES we were able to disentangle the lattice and the electronic response of the prototype Mott material V_2O_3. The excitation of the electrons in the empty a_{1g} bonding orbital leads to a stiffening of the bonds that results in a phonon hardening. The effect of this hardening is seen on the electronic structure, which has more states near the Fermi level different from a heated state. The non-thermal state relaxes towards a the thermal state in about 2 ps. On longer timescales, a shock wave propagates through the sample and after 300 ps the sample is in an equilibrium heated state. The heated state can be used to photoinduce an insulator from a metal when using the 1.1% Cr doped sample as seen using THz spectroscopy.

Comparing the excited electronic structure of V_2O_3 and $BaCoS_2$, we have been able to identify the key out-of-equilibrium properties of Mott insulators: in-gap states are created that are different from a thermal state, the electrons above the Fermi level relax in less than 200 fs, and the non-thermal states are stable for a few picoseconds. These properties are surely due to the two different orbitals present near the Fermi level. The photoexcitation changes the specific orbital filling thus the material can not be compared to any point on the equilibrium phase diagram, which is constructed for a certain filling of the bands. The non-thermal state is stabilized by the structure in the case of V_2O_3.

In the case of V_2O_3, the rather unusual fact that the empty orbital is bonding

leads to a non-thermal lattice modification that in turn changes the electronic structure. This is the perfect example of the complexity of the electron-phonon interplay in strongly correlated materials. In quasi steady states, the electronic structure can not be modified without a lattice change and vice versa. These findings could be fairly general since most Mott insulators have two bands near the Fermi energy. The higher energy orbital can be populated by photoexcitation, which might lead to a structural distortion if the orbital has a different bonding strength than the lower orbital. Consequently, the structural distortion stabilizes a non-thermal state, evacuating the electrons above the Fermi energy and leaving only in-gap states.

This work has greatly benefited from the technological advances in time-resolved techniques. The advent of stable femtosecond laser systems has enabled more complex measurements to be carried out: such as time-resolved ARPES, X-ray diffraction, and THz spectroscopy. As the domain of time-resolved measurements matures, the techniques become more and more stable and smaller effects can be analyzed. The comprehension of physics of ultrafast phenomena has also evolved: turning away from the two temperature model, developing more microscopic models, and coherently pumping certain optical transition.

The domain of time-resolved femtosecond phenomena is fairly young therefore many studies have still to be performed. The time-resolved lattice and electronic structure should be investigated in other Mott insulators in order to understand whether the in-gap states are accompanied by a lattice distortion. In order to get the complete picture of the electron-lattice interplay in V_2O_3, a high resolution time-resolved X-ray diffraction experiment should be performed for the different crystal directions and phases. The precise c/a ratio variation could then be compared to the theoretical values computed with LDA. The lifetime of this structural change could then be compared to the electronic changes seen. This experiment should be done using a time resolution better than the phonon frequency thus only at a free electron laser could this experiment be conducted. The same should be done for $BaCoS_2$.

Time-resolved ARPES experiments should also be performed using XUV photons to probe the effective Coulomb repulsion by following the lower Hubbard band. Since the filling of the band changes during the first 100 fs, the Coulomb screening should also be affected. The high Harmonic could also be used to pump at higher fluences in order to see the possible non linear responses. A single pump laser shot could also be performed on the 1.1% Cr doped sample to see if a single pulse can trigger the metal to insulator transition as seen with heat accumulation in chapter 5.

Our work shows the importance of selective excitation, where the optical transition changes the filling of specific orbitals and hence their bonding strength. These

selective excitation lead the pathway for ultrafast control of the conductivity of materials. The pump wavelength and polarization can be tuned to populate a specific orbital that can act on the lattice in order to push the material towards a conducting or insulating phase. These wavelength can be either above or under the band gap. The other solution is to act directly on the lattice by exciting specific phonons using THz pulses. These studies will have to be done combining X-rays and ARPES in order to really disentangle the lattice and the electronic behavior.

Bibliography

[1] R. Alfano and S. Shapiro. Optical phonon lifetime measured directly with picosecond pulses. *Physical Review Letters*, 26(20):1247, 1971. URL: http://journals.aps.org/prl/abstract/10.1103/PhysRevLett.26.1247.

[2] P. B. Allen. Theory of Thermal Relaxation of Electrons in Metals. *Physical review letters*, 59(13):1460–12463, 1987.

[3] A. Amaricci, C. Weber, M. Capone, and G. Kotliar. Approach to a stationary state in a driven Hubbard model coupled to a thermostat. *Physical Review B*, 86(8):085110, Aug. 2012. URL: http://link.aps.org/doi/10.1103/PhysRevB.86.085110, doi:10.1103/PhysRevB.86.085110.

[4] P. André, M. Schiro, and M. Fabrizio. Lattice and surface effects in the out-of-equilibrium dynamics of the Hubbard model. *Physical Review B*, 85(20):205118, 2012. URL: http://prb.aps.org/abstract/PRB/v85/i20/e205118, arXiv:arXiv:1202.4684v1.

[5] P. André, M. Schiró, and M. Fabrizio. Lattice and surface effects in the out-of-equilibrium dynamics of the Hubbard model. *Physical Review B*, 85(20):205118, May 2012. URL: http://link.aps.org/doi/10.1103/PhysRevB.85.205118.

[6] V. Andreev, F. Chudnovskii, A. Petrov, and E. Terukov. Thermal conductivity of VO_2, V_3O_5, and V_2O_3. *physica status solidi (a)*, 48(2):K153—-K156, 1978. URL: http://dx.doi.org/10.1002/pssa.2210480257, doi:10.1002/pssa.2210480257.

[7] S. Anisimov, B. Kapeliovich, and T. Perel'Man. Electron emission from metal surfaces exposed to ultrashort laser pulses. *Zh. Eksp. Teor. Fiz*, 66(2):375–377, 1974. URL: http://www.jetp.ac.ru/cgi-bin/dn/e_039_02_0375.pdf.

[8] H. Aoki, N. Tsuji, M. Eckstein, M. Kollar, T. Oka, and P. Werner. Nonequilibrium dynamical mean-field theory and its applications. *Reviews of Modern Physics*, 86(2):779–837, June 2014. URL: http://link.aps.org/doi/10.1103/RevModPhys.86.779, doi:10.1103/RevModPhys.86.779.

[9] M. I. Aroyo, J. M. Perez-Mato, C. Capillas, E. Kroumova, S. Ivantchev, G. Madariaga, A. Kirov, and H. Wondratschek. Bilbao Crystallographic Server: I. Databases and crystallographic computing programs. *Zeitschrift für Kristallographie*, 221(1):15–27, Jan. 2006. URL: http://www.degruyter.com/view/j/zkri.2006.221.issue-1_2006/zkri.2006.221.1.15/zkri.2006.221.1.15.xml, doi:10.1524/zkri.2006.221.1.15.

[10] V. Axt and T. Kuhn. Femtosecond spectroscopy in semiconductors: a key to coherences, correlations and quantum kinetics. *Reports on Progress in Physics*, 67(4):433–512, 2004. URL: http://iopscience.iop.org/0034-4885/67/4/R01, doi:10.1088/0034-4885/67/4/R01.

[11] L. Baldassarre, A. Perucchi, D. Nicoletti, A. Toschi, G. Sangiovanni, K. Held, M. Capone, M. Ortolani, L. Malavasi, M. Marsi, P. Metcalf, P. Postorino, and S. Lupi. Quasiparticle evolution and pseudogap formation in V_2O_3: An infrared spectroscopy study. *Physical Review B*, 77(11):1–4, Mar. 2008. URL: http://link.aps.org/doi/10.1103/PhysRevB.77.113107, doi:10.1103/PhysRevB.77.113107.

[12] J. Bardeen, L. Cooper, and J. Schrieffer. Theory of superconductivity. *Physical Review*, 108(5):1175, 1957. URL: http://journals.aps.org/pr/abstract/10.1103/PhysRev.108.1175.

[13] D. N. Basov, R. D. Averitt, D. van der Marel, M. Dressel, and K. Haule. Electrodynamics of correlated electron materials. *Rev. Mod. Phys.*, 83(2):471–541, 2011. URL: http://link.aps.org/doi/10.1103/RevModPhys.83.471, doi:10.1103/RevModPhys.83.471.

[14] P. Baum, D.-S. Yang, and A. H. Zewail. 4D visualization of transitional structures in phase transformations by electron diffraction. *Science (New York, N.Y.)*, 318(5851):788–92, Nov. 2007. URL: http://www.ncbi.nlm.nih.gov/pubmed/17975063, doi:10.1126/science.1147724.

[15] M. C. Beard, G. M. Turner, and C. A. Schmuttenmaer. Terahertz spectroscopy. *The Journal of Physical Chemestry B*, 106:7146–7159, 2002. URL: http://pubs.acs.org/doi/abs/10.1021/jp020579i.

[16] E. Beaurepaire, J. Merle, A. Daunois, and J. Bigot. Ultrafast spin dynamics in ferromagnetic nickel. *Physical review letters*, 76(22):4250–4253, May 1996. URL: http://www.ncbi.nlm.nih.gov/pubmed/10061239.

[17] M. Behrmann, M. Fabrizio, and F. Lechermann. Extended dynamic Mott transition in the two-band Hubbard model out of equilibrium. *Physical Review B*, 88(3):035116, 2013. URL: http://journals.aps.org/prb/abstract/10.1103/PhysRevB.88.035116, arXiv:arXiv:1304.6013v1.

[18] N. Bergeard, M. G. Silly, D. Krizmancic, C. Chauvet, M. Guzzo, J. P. Ricaud, M. Izquierdo, L. Stebel, P. Pittana, R. Sergo, G. Cautero, G. Dufour, F. Rochet, and F. Sirotti. Time-resolved photoelectron spectroscopy using synchrotron radiation time structure. *Journal of synchrotron radiation*, 18(2):245–50, Mar. 2011. URL: http://www.ncbi.nlm.nih.gov/pubmed/21335912, doi:10.1107/S0909049510052301.

[19] F. Bloch. Über die Quantenmechanik der Elektronen in Kristallgittern. *Zeitschrift für Physik*, 52(7-8):555–600, 1929. URL: http://dx.doi.org/10.1007/BF01339455, doi:10.1007/BF01339455.

[20] I. Bloch and W. Zwerger. Many-body physics with ultracold gases. *Reviews of Modern Physics*, 80(3):885–964, July 2008. URL: http://link.aps.org/doi/10.1103/RevModPhys.80.885, doi:10.1103/RevModPhys.80.885.

[21] G. Borghi, M. Fabrizio, and E. Tosatti. Surface Dead Layer for Quasiparticles Near a Mott Transition. *Physical Review Letters*, 102(6):066806, Feb. 2009. URL: http://link.aps.org/doi/10.1103/PhysRevLett.102.066806, doi:10.1103/PhysRevLett.102.066806.

[22] P. Borri, W. Langbein, S. Schneider, U. Woggon, R. Sellin, D. Ouyang, and D. Bimberg. Ultralong Dephasing Time in InGaAs Quantum Dots. *Physical Review Letters*, 87(15):157401, Sept. 2001. URL: http://link.aps.org/doi/10.1103/PhysRevLett.87.157401, doi:10.1103/PhysRevLett.87.157401.

[23] D. Boschetto. HDR: Etudes résolues en temps de phonons optiques cohérents et processus ultrarapides dans les semimétaux et les matériaux fortement corrélés, 2012.

[24] D. Boschetto, E. Gamaly, A. Rode, B. Luther-Davies, D. Glijer, T. Garl, O. Albert, A. Rousse, and J. Etchepare. Small Atomic Displacements Recorded in Bismuth by the Optical Reflectivity of Femtosecond Laser-Pulse Excitations. *Physical Review Letters*, 100(2):7–10, Jan. 2008. URL:

http://link.aps.org/doi/10.1103/PhysRevLett.100.027404, doi:10.1103/PhysRevLett.100.027404.

[25] D. Boschetto, L. Malard, C. H. Lui, K. F. Mak, Z. Li, H. Yan, and T. F. Heinz. Real-Time Observation of Interlayer Vibrations in Bilayer and Few-Layer Graphene. *Nano letters*, 13(10):4620–4623, Sept. 2013. URL: http://www.ncbi.nlm.nih.gov/pubmed/24047242, doi:10.1021/nl401713h.

[26] D. Boschetto and A. Rousse. Coherent Optical Phonons in Bismuth Crystal, Coherence and Ultrashort Pulse Laser Emission. In D. F. J. Duarte, editor, *Coherence and Ultrashort Pulse Laser Emission*, chapter 5. InTech, first edition, 2010.

[27] U. Bovensiepen. Magnetism in step with light. *Nature Physics*, 5(7):461–463, 2009.

[28] W. Bragg. The Diffraction of Short Electromagnetic Waves by a Crystal. *Proceedings of the Cambridge Philosophical Society*, 17:43–57, 1913.

[29] W. Bragg. The diffraction of X-rays by crystals. In *Nobel Lecture*, 1922.

[30] W. Brinkman and T. Rice. Application of Gutzwiller's variational method to the metal-insulator transition. *Physical Review B*, 2(10):4302–43–04, 1970. URL: http://journals.aps.org/prb/abstract/10.1103/PhysRevB.2.4302.

[31] J. S. Brockman, L. Gao, B. Hughes, C. T. Rettner, M. G. Samant, K. P. Roche, and S. S. P. Parkin. Subnanosecond incubation times for electric-field-induced metallization of a correlated electron oxide. *Nature Nanotechnology*, 9(6):453–458, Apr. 2014. URL: http://www.nature.com/doifinder/10.1038/nnano.2014.71, doi:10.1038/nnano.2014.71.

[32] W. Brückner, H. Oppermann, W. Reichelt, J. I. Wolf, A. F. Terukow, and E. Tschudnowski. Vanadiumoxide Darstellung, Eigenschaften, Anwendung (Akademie, Berlin). *Crystal Research and Technology*, 19(3):392, 1984. URL: http://dx.doi.org/10.1002/crat.2170190316, doi:10.1002/crat.2170190316.

[33] W. R. Busing and H. A. Levy. Angle calculations for 3- and 4-circle X-ray and neutron diffractometers. *Acta Crystallographica*, 22(4):457–464, Apr. 1967. URL: http://scripts.iucr.org/cgi-bin/paper?S0365110X67000970, doi:10.1107/S0365110X67000970.

[34] J. Callan, A. Kim, L. Huang, and E. Mazur. Ultrafast electron and lattice dynamics in semiconductors at high excited carrier densities. *Chemical Physics*, 251(1-3):167–179, 2000. URL: http://www.sciencedirect.com/science/article/pii/S0301010499003018.

[35] C. Castellani, C. Natoli, and J. Ranninger. Insulating phase of V_2O_3: An attempt at a realistic calculation. *Physical Review B*, 18(9):4967–5000, 1978. URL: http://journals.aps.org/prb/abstract/10.1103/PhysRevB.18.4967.

[36] C. Castellani, C. Natoli, and J. Ranninger. Magnetic structure of V_2O_3 in the insulating phase. *Physical Review B*, 18(9):4945, 1978. URL: http://journals.aps.org/prb/abstract/10.1103/PhysRevB.18.4945.

[37] C. Castellani, C. Natoli, and J. Ranninger. Metal-insulator transition in pure and Cr-doped V_2O_3. *Physical Review B*, 18(9):5001, 1978.

[38] A. L. Cavalieri, N. Müller, T. Uphues, V. S. Yakovlev, A. Baltuska, B. Horvath, B. Schmidt, L. Blümel, R. Holzwarth, S. Hendel, M. Drescher, U. Kleineberg, P. M. Echenique, R. Kienberger, F. Krausz, and U. Heinzmann. Attosecond spectroscopy in condensed matter. *Nature*, 449(7165):1029–32, Oct. 2007. URL: http://www.ncbi.nlm.nih.gov/pubmed/17960239, doi:10.1038/nature06229.

[39] A. Cavalleri, T. Dekorsy, H. Chong, J. Kieffer, and R. Schoenlein. Evidence for a structurally-driven insulator-to-metal transition in VO_2: A view from the ultrafast timescale. *Physical Review B*, 70(16):3–6, Oct. 2004. URL: http://link.aps.org/doi/10.1103/PhysRevB.70.161102, doi:10.1103/PhysRevB.70.161102.

[40] A. Cavalleri, C. Tóth, C. Siders, J. Squier, F. Ráksi, P. Forget, and J. Kieffer. Femtosecond Structural Dynamics in VO_2 during an Ultrafast Solid-Solid Phase Transition. *Physical Review Letters*, 87(23):237401, Nov. 2001. URL: http://link.aps.org/doi/10.1103/PhysRevLett.87.237401, doi:10.1103/PhysRevLett.87.237401.

[41] D. S. Chemla and J. Shah. Many-body and correlation effects in semiconductors. *Nature*, 411(6837):549–57, May 2001. URL: http://www.ncbi.nlm.nih.gov/pubmed/11385562, doi:10.1038/35079000.

[42] S. Chen, J. E. Hahn, C. E. Rice, and W. R. Robinson. The effects of titanium or chromium doping on the crystal structure of V_2O_3. *Journal of Solid State chemistry*, 44(2):192–200, 1982. URL: http://www.sciencedirect.com/science/article/pii/0022459682903656.

[43] F. Cilento, S. Dal Conte, G. Coslovich, S. Peli, N. Nembrini, S. Mor, F. Banfi, G. Ferrini, H. Eisaki, M. Chan, C. Dorow, M. Veit, M. Greven, D. van der Marel, R. Comin, A. Damascelli, L. Rettig, U. Bovensiepen, M. Capone, C. Giannetti, and F. Parmigiani. Photo-enhanced antinodal conductivity in the pseudogap state of high T_c cuprates. *arXiv preprint arXiv: ...*, 2014. URL: http://arxiv.org/abs/1405.5462.

[44] C. Cohen-Tannoudji, B. Diu, and F. Laloë. *Mecanique quantique*. Hermann, Paris, 1973.

[45] R. Cortés, L. Rettig, Y. Yoshida, H. Eisaki, M. Wolf, and U. Bovensiepen. Momentum-Resolved Ultrafast Electron Dynamics in Superconducting $Bi_2Sr_2CaCu_2O_{8+\delta}$. *Physical Review Letters*, 107(9):1–4, Aug. 2011. URL: http://link.aps.org/doi/10.1103/PhysRevLett.107.097002, doi:10.1103/PhysRevLett.107.097002.

[46] A. Damascelli. Probing the Electronic Structure of Complex Systems by ARPES. *Physica Scripta*, T109:61, 2004. URL: http://www.physica.org/xml/article.asp?article=t109a00061.xml, doi:10.1238/Physica.Topical.109a00061.

[47] A. Damascelli, Z. Hussain, and Z. Shen. Angle-resolved photoemission studies of the cuprate superconductors. *Reviews of Modern Physics*, 75(2):473–541, 2003. URL: http://rmp.aps.org/abstract/RMP/v75/i2/p473_1http://journals.aps.org/rmp/abstract/10.1103/RevModPhys.75.473.

[48] J. H. De Boer and J. W. Verwey. Semi-conductors with partially and with completely filled 3d-lattice bands. *Proceedings of the Physical Society*, 49:59, 1937.

[49] G. De Filippis, V. Cataudella, E. A. Nowadnick, T. P. Devereaux, A. S. Mishchenko, and N. Nagaosa. Quantum Dynamics of the Hubbard-Holstein Model in Equilibrium and Nonequilibrium: Application to Pump-Probe Phenomena. *Physical Review Letters*, 109(17):176402, Oct. 2012. URL: http://link.aps.org/doi/10.1103/PhysRevLett.109.176402, doi:10.1103/PhysRevLett.109.176402.

[50] W. V. der Linden, E. Berger, and P. Valášek. The Hubbard-Holstein model. *Journal of low temperature ...*, 99(3):517–525, 1995. URL: http://link.springer.com/article/10.1007/BF00752333.

[51] P. Dernier and M. Marezio. Crystal Structure of the Low-Temperature Antiferromagnetic Phase of V_2O_3. *Physical Review B*, 2(9):3771, 1970. URL: http://prb.aps.org/abstract/PRB/v2/i9/p3771_1.

[52] V. Dubost, T. Cren, C. Vaju, and L. Cario. Resistive switching at the nanoscale in the Mott Insulator compound $GaTa_4Se_8$. *Nano letters*, 13(8):3648–3653, 2013. URL: http://pubs.acs.org/doi/abs/10.1021/nl401510p.

[53] M. Eckstein, M. Kollar, and P. Werner. Thermalization after an Interaction Quench in the Hubbard Model. *Physical Review Letters*, 103(5):056403, July 2009. URL: http://link.aps.org/doi/10.1103/PhysRevLett.103.056403, doi:10.1103/PhysRevLett.103.056403.

[54] M. Eckstein and P. Werner. Thermalization of a pump-excited Mott insulator. *Physical Review B*, 84(3):035122, July 2011. URL: http://link.aps.org/doi/10.1103/PhysRevB.84.035122, doi:10.1103/PhysRevB.84.035122.

[55] M. Eckstein and P. Werner. Nonequilibrium dynamical mean-field simulation of inhomogeneous systems. *Physical Review B*, 88(7):075135, 2013. URL: http://journals.aps.org/prb/abstract/10.1103/PhysRevB.88.075135, arXiv:arXiv:1303.4618v1.

[56] A. Einstein. On a heuristic point of view about the creation and conversion of light. *Annalen der Physik*, 322(6):132–148, 1905. URL: http://www.pitt.edu/$\sim$jdnorton/lectures/Rotman_Summer_School_2013/Einstein_1905_docs/Einstein_Light_Quantum_WikiSource.pdf.

[57] F. Elder, A. Gurewitsch, R. Langmuir, and H. Pollock. Radiation from electrons in a synchrotron. *Physical Review*, 71(11):829–830, 1947. URL: http://link.aps.org/doi/10.1103/PhysRev.71.829.5.

[58] G. M. Eliashberg. Interactions between electrons and lattice vibrations in a superconductor. *Sov. Phys.-JETP (Engl. Transl.)*, 11(3), 1960.

[59] H. Elsayed-Ali, T. Norris, M. Pessot, and G. Mourou. Time-resolved observation of electron-phonon relaxation in copper. *Physical Review Letters*, 58(12):1212–1215, 1987. URL: http://journals.aps.org/prl/abstract/10.1103/PhysRevLett.58.1212.

[60] R. Ernstorfer, M. Harb, C. T. Hebeisen, G. Sciaini, T. Dartigalongue, and R. J. D. Miller. The formation of warm dense matter: experimental evidence for electronic bond hardening in gold. *Science (New York,*

N. Y.), 323(5917):1033–7, Feb. 2009. URL: http://www.ncbi.nlm.nih.gov/pubmed/19164708, doi:10.1126/science.1162697.

[61] P. Ewald. Introduction to the dynamical theory of X-ray diffraction. *Acta Crystallographica Section A*, 25:103–108, 1969. doi:10.1107/S0567739469000155.

[62] J. Faure, J. Mauchain, E. Papalazarou, M. Marsi, D. Boschetto, I. Timrov, N. Vast, Y. Ohtsubo, B. Arnaud, and L. Perfetti. Direct observation of electron thermalization and electron-phonon coupling in photoexcited bismuth. *Physical Review B*, 88(7):075120, Aug. 2013. URL: http://link.aps.org/doi/10.1103/PhysRevB.88.075120, doi:10.1103/PhysRevB.88.075120.

[63] J. Faure, J. Mauchain, E. Papalazarou, W. Yan, J. Pinon, M. Marsi, and L. Perfetti. Full characterization and optimization of a femtosecond ultraviolet laser source for time and angle-resolved photoemission on solid surfaces. *The Review of scientific instruments*, 83(4):043109, May 2012. URL: http://www.ncbi.nlm.nih.gov/pubmed/22559517, doi:10.1063/1.3700190.

[64] D. Fausti, R. I. Tobey, N. Dean, S. Kaiser, A. Dienst, M. C. Hoffmann, S. Pyon, T. Takayama, H. Takagi, and A. Cavalleri. Light-induced superconductivity in a stripe-ordered cuprate. *Science (New York, N. Y.)*, 331(6014):189–91, Jan. 2011. URL: http://www.ncbi.nlm.nih.gov/pubmed/21233381, doi:10.1126/science.1197294.

[65] M. Fiebig, K. Miyano, Y. Tomioka, and Y. Tokura. Visualization of the Local Insulator-Metal Transition in $Pr_{0.7}Ca_{0.3}MnO_3$. *Science*, 280(5371):1925–1928, June 1998. URL: http://www.sciencemag.org/cgi/doi/10.1126/science.280.5371.1925, doi:10.1126/science.280.5371.1925.

[66] E. Fradkin, S. Kivelson, and J. Tranquada. Theory of Intertwined Orders in High Temperature Superconductors. *arXiv preprint arXiv:1407.4480*, pages 1–28, 2014. URL: http://arxiv.org/abs/1407.4480, arXiv:arXiv:1407.4480v1.

[67] A. Fujimori, K. Mamiya, T. Mizokawa, T. Miyadai, T. Sekiguchi, H. Takahashi, N. Môri, and S. Suga. Resonant photoemission study of pyrite-type NiS2, CoS2 and FeS2. *Physical review. B, Condensed matter*, 54(23):16329–16332, Dec. 1996. URL: http://www.ncbi.nlm.nih.gov/pubmed/9985736.

[68] J. Fujimoto, J. Liu, E. Ippen, and N. Bloembergen. Femtosecond laser interaction with metallic tungsten and nonequilibrium electron and lattice temperatures. *Physical Review Letters*, 53(19):1837–1840, 1984. URL: http://journals.aps.org/prl/abstract/10.1103/PhysRevLett.53.1837.

[69] H. Fujiwara, A. Sekiyama, S.-K. Mo, J. W. Allen, J. Yamaguchi, G. Funabashi, S. Imada, P. Metcalf, A. Higashiya, M. Yabashi, K. Tamasaku, T. Ishikawa, and S. Suga. Evidence for the constancy of U in the Mott transition of V_2O_3. *Physical Review B*, 84(7):075117, Aug. 2011. URL: http://link.aps.org/doi/10.1103/PhysRevB.84.075117, doi:10.1103/PhysRevB.84.075117.

[70] A. Georges and G. Kotliar. Hubbard model in infinite dimensions. *Physical Review B*, 45(12):6479, 1992. URL: http://journals.aps.org/prb/abstract/10.1103/PhysRevB.45.6479.

[71] A. Georges, G. Kotliar, W. Krauth, and M. Rozenberg. Dynamical mean-field theory of strongly correlated fermion systems and the limit of infinite dimensions. *Reviews of Modern Physics*, 68(1):13, 1996. URL: http://rmp.aps.org/abstract/RMP/v68/i1/p13_1http://journals.aps.org/rmp/abstract/10.1103/RevModPhys.68.13.

[72] S. M. Gilbertson, T. Durakiewicz, G. L. Dakovski, Y. Li, J.-X. Zhu, S. D. Conradson, S. A. Trugman, and G. Rodriguez. Ultrafast Photoemission Spectroscopy of the Uranium Dioxide UO_2 Mott Insulator: Evidence for a Robust Energy Gap Structure. *Physical Review Letters*, 112(8):087402, Feb. 2014. URL: http://link.aps.org/doi/10.1103/PhysRevLett.112.087402, doi:10.1103/PhysRevLett.112.087402.

[73] J. B. Goodenough. The two components of the crystallographic transition in VO_2. *Journal of Solid State Chemistry*, 3(4):490–500, Nov. 1971. URL: http://linkinghub.elsevier.com/retrieve/pii/0022459671900910, doi:10.1016/0022-4596(71)90091-0.

[74] J. Graf, C. Jozwiak, C. L. Smallwood, H. Eisaki, R. A. Kaindl, D.-H. Lee, and A. Lanzara. Nodal quasiparticle meltdown in ultrahigh-resolution pump-probe angle-resolved photoemission. *Nature Physics*, 7(10):805–809, July 2011. URL: http://www.nature.com/doifinder/10.1038/nphys2027, doi:10.1038/nphys2027.

[75] R. Groeneveld, R. Sprik, and A. Lagendijk. Femtosecond spectroscopy of electron-electron and electron-phonon energy relaxation in Ag and Au. *Physical review. B*, 51(17):11433–11445, May 1995. URL: http://www.ncbi.nlm.nih.gov/pubmed/9977873.

[76] V. Guiot, L. Cario, E. Janod, B. Corraze, V. Ta Phuoc, M. Rozenberg, P. Stoliar, T. Cren, and D. Roditchev. Avalanche breakdown in $GaTa_4Se_{8-x}Te_x$ narrow-gap Mott insulators. *Nature communications*, 4:1722, Apr. 2013.

URL: http://www.ncbi.nlm.nih.gov/pubmed/23591889, doi:10.1038/ncomms2735.

[77] M. C. Gutzwiller. Effect of correlation on the ferromagnetism of transition metals. *Physical review letters*, 10(5):159, 1963.

[78] M. C. Gutzwiller. Correlation of electrons in a Narrow s Band. *Physical Review*, 137(6A):A 1726, 1965.

[79] M. Hajlaoui, E. Papalazarou, J. Mauchain, G. Lantz, N. Moisan, D. Boschetto, Z. Jiang, I. Miotkowski, Y. P. Chen, A. Taleb-Ibrahimi, L. Perfetti, and M. Marsi. Ultrafast Surface Carrier Dynamics in the Topological Insulator Bi_2Te_3. *Nano Letters*, 12(7):3532–3536, 2012. URL: http://pubs.acs.org/doi/abs/10.1021/nl301035x, doi:10.1021/nl301035x.

[80] S. Han, Z. Vardeny, K. Wong, O. Symko, and G. Koren. Femtosecond Optical Detection of Quasiparticle Dynamics in High-T_c, $YBa_2Cu_30_{7-\delta}$ Superconducting Thin Films. *Physical review letters*, 65(21):2708–2711, 1990. URL: http://journals.aps.org/prl/abstract/10.1103/PhysRevLett.65.2708.

[81] P. Hansmann, A. Toschi, G. Sangiovanni, S. Lupi, M. Marsi, and K. Held. Mott-Hubbard transition in V_2O_3 revisited. *physica status solidi (b)*, 250(7):1251–1264, 2013. arXiv:arXiv:1303.2050v1.

[82] I. Hase, N. Shirakawa, and Y. Nishihara. Electronic Structures of $BaNiS_2$ and $BaCoS_2$. *J. Phys. Soc. Jpn.*, 64(7):2533–2540, 1995. URL: http://jpsj.ipap.jp/link?JPSJ/64/2533/.

[83] K. Held, G. Keller, V. Eyert, D. Vollhardt, and V. Anisimov. Mott-Hubbard Metal-Insulator Transition in Paramagnetic V_2O_3: An LDA+DMFT(QMC) Study. *Physical Review Letters*, 86(23):5345–5348, June 2001. URL: http://link.aps.org/doi/10.1103/PhysRevLett.86.5345, doi:10.1103/PhysRevLett.86.5345.

[84] S. Hellmann, T. Rohwer, M. Kalläne, K. Hanff, C. Sohrt, A. Stange, A. Carr, M. M. Murnane, H. C. Kapteyn, L. Kipp, M. Bauer, and K. Rossnagel. Time-domain classification of charge-density-wave insulators. *Nature communications*, 3:1069, Jan. 2012. URL: http://www.ncbi.nlm.nih.gov/pubmed/22990865, doi:10.1038/ncomms2078.

[85] H. Hertz. Ueber einen Einfluss des ultravioletten Lichtes auf die electrische Entladung. *Annalen der Physik*, 267(8):983–1000, 1887.

[86] T. Holstein. Studies of polaron motion: Part I. The molecular-crystal model. *Annals of Physics*, 8:325–342, 1959. URL: http://www.sciencedirect.com/science/article/pii/0003491659900028.

[87] W. Hu, S. Kaiser, D. Nicoletti, C. R. Hunt, I. Gierz, M. C. Ho, M. L. Tacon, T. Loew, B. Keimer, and A. Cavalleri. Optically enhanced coherent transport in $YBa_2Cu_3O_{6.5}$ by ultrafast redistribution of interlayer coupling. *Nature materials*, 13(7):705–711, 2014. doi:10.1038/NMAT3963.

[88] J. Hubbard. Electron Correlations in Narrow Energy Bands. *Proceedings of the Royal Society of London. Series A. Mathematical and Physical Sciences*, 276(1365):238–257, 1963. URL: http://rspa.royalsocietypublishing.org/content/276/1365/238.abstract, doi:10.1098/rspa.1963.0204.

[89] R. Huber, F. Tauser, A. Brodschelm, M. Bichler, G. Abstreiter, and A. Leitenstorfer. How many-particle interactions develop after ultrafast excitation of an electron-hole plasma. *Nature*, 414(6861):286–9, Nov. 2001. URL: http://www.ncbi.nlm.nih.gov/pubmed/11713523, doi:10.1038/35104522.

[90] M. Imada, A. Fujimori, and Y. Tokura. Metal-insulator transitions. *Reviews of Modern Physics*, 70(4):1039–1263, Oct. 1998. URL: http://link.aps.org/doi/10.1103/RevModPhys.70.1039, doi:10.1103/RevModPhys.70.1039.

[91] S. Iwai, M. Ono, A. Maeda, H. Matsuzaki, H. Kishida, H. Okamoto, and Y. Tokura. Ultrafast Optical Switching to a Metallic State by Photoinduced Mott Transition in a Halogen-Bridged Nickel-Chain Compound. *Physical Review Letters*, 91(5):3–6, July 2003. URL: http://link.aps.org/doi/10.1103/PhysRevLett.91.057401, doi:10.1103/PhysRevLett.91.057401.

[92] D. Iwanenko and I. Pomeranchuk. On the Maximal Energy Attainable in a Batatron. *Physical Review*, 65(11):343, 1944.

[93] J. C. Johannsen, S. r. Ulstrup, F. Cilento, A. Crepaldi, M. Zacchigna, C. Cacho, I. C. E. Turcu, E. Springate, F. Fromm, C. Raidel, T. Seyller, F. Parmigiani, M. Grioni, and P. Hofmann. Direct View of Hot Carrier Dynamics in Graphene. *Physical Review Letters*, 111(2):027403, July 2013. URL: http://link.aps.org/doi/10.1103/PhysRevLett.111.027403, doi:10.1103/PhysRevLett.111.027403.

[94] S. Johnson, P. Beaud, C. Milne, F. Krasniqi, E. Zijlstra, M. Garcia, M. Kaiser, D. Grolimund, R. Abela, and G. Ingold. Nanoscale Depth-Resolved Coherent Femtosecond Motion in Laser-Excited Bismuth. *Physical Review Letters*, 100(15):1–4, Apr. 2008. URL: http:

//link.aps.org/doi/10.1103/PhysRevLett.100.155501, doi:10.1103/PhysRevLett.100.155501.

[95] S. Johnson, P. Beaud, E. Vorobeva, C. Milne, E. Murray, S. Fahy, and G. Ingold. Directly Observing Squeezed Phonon States with Femtosecond X-Ray Diffraction. *Physical Review Letters*, 102(17):175503, Apr. 2009. URL: http://link.aps.org/doi/10.1103/PhysRevLett.102.175503, doi:10.1103/PhysRevLett.102.175503.

[96] V. Kabanov and A. Alexandrov. Electron relaxation in metals: Theory and exact analytical solutions. *Physical Review B*, 78(17):174514, 2008. URL: http://journals.aps.org/prb/abstract/10.1103/PhysRevB.78.174514, arXiv:arXiv:0809.0818v4.

[97] M. I. Kaganov, I. M. Lifshitz, and L. V. Tanatarov. Relaxation between electrons and the crystalline lattice. *Sov. Phys. JETP*, 4(2):173, 1957.

[98] R. A. Kaindl, M. Woerner, T. Elsaesser, D. C. Smith, J. F. Ryan, G. A. Farnan, M. P. McCurry, and D. G. Walmsley. Ultrafast Mid-Infrared Response of $YBa_2Cu_3O_{7-\delta}$. *Science*, 287(5452):470–473, Jan. 2000. URL: http://www.sciencemag.org/cgi/doi/10.1126/science.287.5452.470, doi:10.1126/science.287.5452.470.

[99] H. Keer, D. Dickerson, H. Kuwamoto, H. Barros, and J. Honig. Heat capacity of pure and doped V_2O_3 single crystals. *Journal of Solid State Chemistry*, 19(1):95–102, 1976. URL: http://www.sciencedirect.com/science/article/pii/0022459676901559.

[100] G. Keller, K. Held, V. Eyert, D. Vollhardt, and V. Anisimov. Electronic structure of paramagnetic V_2O_3: Strongly correlated metallic and Mott insulating phase. *Physical Review B*, 70(20):205116, Nov. 2004. URL: http://link.aps.org/doi/10.1103/PhysRevB.70.205116, doi:10.1103/PhysRevB.70.205116.

[101] A. Kirilyuk, A. V. Kimel, and T. Rasing. Ultrafast optical manipulation of magnetic order. *Reviews of Modern Physics*, 82(3):2731–2784, Sept. 2010. URL: http://link.aps.org/doi/10.1103/RevModPhys.82.2731, doi:10.1103/RevModPhys.82.2731.

[102] C. Kittel. *Introduction to Solid State Physics*. Wiley, New York, seventh edition, 1996.

[103] P. Kner, S. Bar-Ad, and M. Marquezini. Magnetically enhanced exciton-exciton correlations in semiconductors. *Physical review letters*, 78(7):1319–1322, 1997. URL: http://journals.aps.org/prl/abstract/10.1103/PhysRevLett.78.1319.

[104] J. Koralek, J. Douglas, N. Plumb, Z. Sun, A. Fedorov, M. Murnane, H. Kapteyn, S. Cundiff, Y. Aiura, K. Oka, H. Eisaki, and D. Dessau. Laser Based Angle-Resolved Photoemission, the Sudden Approximation, and Quasiparticle-Like Spectral Peaks in $Bi_2Sr_2CaCu_2O_{8+\delta}$. *Physical Review Letters*, 96(1):017005, Jan. 2006. URL: http://link.aps.org/doi/10.1103/PhysRevLett.96.017005, doi:10.1103/PhysRevLett.96.017005.

[105] G. Kotliar and D. Vollhardt. Strongly correlated materials: Insights from dynamical mean-field theory. *Physics Today*, (March):53–59, 2004. URL: http://www.physics.rutgers.edu/$\sim$kotliar/papers/PT-Kotliar_57_53.pdf.

[106] C. Lamsal and N. M. Ravindra. Optical properties of vanadium oxides-an analysis. *Journal of Materials Science*, 48(18):6341, May 2013. URL: http://link.springer.com/10.1007/s10853-013-7433-3, doi:10.1007/s10853-013-7433-3.

[107] B. Larson, C. White, T. Noggle, and D. Mills. Synchrotron x-ray diffraction study of silicon during pulsed-laser annealing. *Physical review letters*, 48(5):337–340, 1982. URL: http://journals.aps.org/prl/abstract/10.1103/PhysRevLett.48.337.

[108] P. Limelette, A. Georges, D. Jérome, P. Wzietek, P. Metcalf, and J. M. Honig. Universality and critical behavior at the Mott transition. *Science (New York, N.Y.)*, 302(5642):89–92, Oct. 2003. URL: http://www.ncbi.nlm.nih.gov/pubmed/14526075, doi:10.1126/science.1088386.

[109] M. Lisowski, P. Loukakos, A. Melnikov, I. Radu, L. Ungureanu, M. Wolf, and U. Bovensiepen. Femtosecond Electron and Spin Dynamics in Gd(0001) Studied by Time-Resolved Photoemission and Magneto-optics. *Physical Review Letters*, 95(13):137402, Sept. 2005. URL: http://link.aps.org/doi/10.1103/PhysRevLett.95.137402, doi:10.1103/PhysRevLett.95.137402.

[110] M. Liu, B. Pardo, J. Zhang, M. Qazilbash, S. Yun, Z. Fei, J.-H. Shin, H.-T. Kim, D. Basov, and R. Averitt. Photoinduced Phase Transitions by Time-Resolved Far-Infrared Spectroscopy in V_2O_3. *Physical Review Letters*, 107(6):2–6, Aug. 2011. URL: http://link.aps.org/doi/10.1103/PhysRevLett.107.066403, doi:10.1103/PhysRevLett.107.066403.

[111] C. H. Lui, K. F. Mak, J. Shan, and T. F. Heinz. Ultrafast Photoluminescence from Graphene. *Physical Review Letters*, 105(12):127404, Sept. 2010. URL: http://link.aps.org/doi/10.1103/PhysRevLett.105.127404, doi:10.1103/PhysRevLett.105.127404.

[112] S. Lupi, L. Baldassarre, B. Mansart, A. Perucchi, A. Barinov, P. Dudin, E. Papalazarou, F. Rodolakis, J.-P. Rueff, J.-P. Itié, S. Ravy, D. Nicoletti, P. Postorino, P. Hansmann, N. Parragh, A. Toschi, T. Saha-Dasgupta, O. Andersen, G. Sangiovanni, K. Held, and M. Marsi. A microscopic view on the Mott transition in chromium-doped V_2O_3. *Nature communications*, 1(8):105, Jan. 2010. URL: http://www.ncbi.nlm.nih.gov/pubmed/21045823, doi:10.1038/ncomms1109.

[113] B. Mansart, A. Barinov, P. Dudin, L. Baldassarre, A. Perucchi, E. Papalazarou, P. Metcalf, S. Lupi, and M. Marsi. Photoemission microscopy study of the two metal-insulator transitions in Cr-doped V_2O_3. *Applied Physics Letters*, 100(1):014108, 2012. URL: http://link.aip.org/link/APPLAB/v100/i1/p014108/s1&Agg=doi, doi:10.1063/1.3675445.

[114] B. Mansart, D. Boschetto, A. Sambri, R. Malaquias, F. Miletto Granozio, U. Scotti di Uccio, P. Metcalf, and M. Marsi. Ultrafast dynamical response of strongly correlated oxides: role of coherent optical and acoustic oscillations. *Journal of Modern Optics*, 57(11):959–966, June 2010. URL: http://www.tandfonline.com/doi/abs/10.1080/09500340903541072, doi:10.1080/09500340903541072.

[115] B. Mansart, D. Boschetto, S. Sauvage, A. Rousse, and M. Marsi. Mott transition in Cr-doped V_2O_3 studied by ultrafast reflectivity: Electron correlation effects on the transient response. *Europhysics Letters*, 92(3):37007, Nov. 2010. URL: http://stacks.iop.org/0295-5075/92/i=3/a=37007?key=crossref.fd9e56268e838f3d14b21c567ea7ce05, doi:10.1209/0295-5075/92/37007.

[116] B. Mansart, D. Boschetto, A. Savoia, F. Rullier-Albenque, A. Forget, D. Colson, A. Rousse, and M. Marsi. Observation of a coherent optical phonon in the iron pnictide superconductor $Ba(Fe_{1-x}Co_x)_2As_2$ (x=0.06 and 0.08). *Physical Review B*, 80(17):1–4, Nov. 2009. URL: http://link.aps.org/doi/10.1103/PhysRevB.80.172504, doi:10.1103/PhysRevB.80.172504.

[117] B. Mansart, D. Grieger, G. Lantz, V. Balédent, N. Moisan, E. Papalazarou, A. Savoia, D. Boschetto, M. Fabrizio, and M. Marsi. Ultrafast photo-induced non-thermal phonon hardening in the Mott compound V_2O_3. *(unpublished)*, 2014.

[118] L. Martinson, J. Schweitzer, and N. Baenziger. Properties of the layered $BaCo_{1-x}Ni_xS_2$ alloy system. *Physical Review B*, 54(16):265–270, 1996. URL: http://journals.aps.org/prb/abstract/10.1103/PhysRevB.54.11265.

[119] L. Matheiss. Electronic structure of quasi-two-dimensional $BaNiS_2$. *Solid State Communications*, 93(11):879–883, 1995. URL: http://www.sciencedirect.com/science/article/pii/0038109894009007.

[120] D. B. McWhan, A. Menth, J. P. Remeika, W. F. Brinkman, and T. M. Rice. Metal-Insulator Transitions in Pure and Doped V_2O_3. *Physical Review B*, 7(5):1920, 1973. URL: http://prb.aps.org/abstract/PRB/v7/i5/p1920_1.

[121] D. B. McWhan and J. P. Remeika. Metal-Insulator Transition in $(V_{1x}Cr_x)_2O_3$. *Physical Review B*, 2(9):3734, 1970. URL: http://prb.aps.org/abstract/PRB/v2/i9/p3734_1.

[122] D. B. McWhan, T. M. Rice, and J. P. Remeika. Mott Transition in Cr-Doped V_2O_3. *Physical Review Letters*, 23(24):1384, 1969. URL: http://link.aps.org/doi/10.1103/PhysRevLett.23.1384.

[123] R. Merlin. Generating coherent THz phonons with light pulses. *Solid state communications*, 102(2-3):207–220, 1997. URL: http://www.sciencedirect.com/science/article/pii/S0038109896007211.

[124] W. Metzner and D. Vollhardt. Correlated Lattice Fermions in d=infity Dimensions. *Physical review letters*, 62(3):324–327, 1989.

[125] O. Misochko, M. Tani, K. Sakai, K. Kisoda, S. Nakashima, V. Andreev, and F. Chudnovsky. Optical study of the Mott transition in V_2O_3: Comparison of time- and frequency-domain results. *Physical Review B*, 58(19):12789–12794, Nov. 1998. URL: http://link.aps.org/doi/10.1103/PhysRevB.58.12789, doi:10.1103/PhysRevB.58.12789.

[126] M. Mitrano, G. Cotugno, S. R. Clark, R. Singla, S. Kaiser, J. Stähler, R. Beyer, M. Dressel, L. Baldassarre, D. Nicoletti, A. Perucchi, T. Hasegawa, H. Okamoto, D. Jaksch, and A. Cavalleri. Pressure-Dependent Relaxation in the Photoexcited Mott Insulator ETF_2TCNQ: Influence of Hopping and Correlations on Quasiparticle Recombination Rates. *Physical Review Letters*, 112(11):117801, Mar. 2014. URL: http://link.aps.org/doi/10.1103/PhysRevLett.112.117801, doi:10.1103/PhysRevLett.112.117801.

[127] S.-K. Mo, J. Denlinger, H.-D. Kim, J.-H. Park, J. Allen, A. Sekiyama, A. Yamasaki, K. Kadono, S. Suga, Y. Saitoh, T. Muro, P. Metcalf, G. Keller,

K. Held, V. Eyert, V. Anisimov, and D. Vollhardt. Prominent Quasiparticle Peak in the Photoemission Spectrum of the Metallic Phase of V_2O_3. *Physical Review Letters*, 90(18):3–6, May 2003. URL: http://link.aps.org/doi/10.1103/PhysRevLett.90.186403, doi:10.1103/PhysRevLett.90.186403.

[128] S.-K. Mo, H.-D. Kim, J. Allen, G.-H. Gweon, J. Denlinger, J.-H. Park, A. Sekiyama, A. Yamasaki, S. Suga, P. Metcalf, and K. Held. Filling of the Mott-Hubbard Gap in the High Temperature Photoemission Spectrum of $(V_{0.972}Cr_{0.028})_2O_3$. *Physical Review Letters*, 93(7):076404, Aug. 2004. URL: http://link.aps.org/doi/10.1103/PhysRevLett.93.076404, doi:10.1103/PhysRevLett.93.076404.

[129] S.-K. Mo, H.-D. Kim, J. Denlinger, J. Allen, J.-H. Park, A. Sekiyama, A. Yamasaki, S. Suga, Y. Saitoh, T. Muro, and P. Metcalf. Photoemission study of $(V_{1-x}M_x)_2O_3$ (M=Cr,Ti). *Physical Review B*, 74(16):165101, Oct. 2006. URL: http://link.aps.org/doi/10.1103/PhysRevB.74.165101, doi:10.1103/PhysRevB.74.165101.

[130] F. J. Morin. Oxides wich show a metal-to-insulator transition at the Neel temperature. *Physical review letters*, 3(1):34–36, 1959.

[131] V. R. Morrison, R. P. Chatelain, K. L. Tiwari, A. Hendaoui, A. Bruhacs, M. Chaker, and B. J. Siwick. A photoinduced metallic phase of monoclinic vanadium dioxide. *Arxiv preprint arXiv:*, page 19, July 2014. URL: http://arxiv.org/abs/1407.1304, arXiv:1407.1304.

[132] N. Mott. The basis of the electron theory of metals, with special reference to the transition metals. *Proceedings of the Physical Society. Section A*, 62(7):416, 1949. URL: http://iopscience.iop.org/0370-1298/62/7/303.

[133] N. Mott. Metal-Insulator transition. *Reviews of Modern Physics*, 40(4):677, 1968.

[134] N. Mott. *Metal-Insulator Transitions*. Taylor Francis, 1990. URL: http://books.google.fr/books?id=Q0mJQgAACAAJ.

[135] N. Mott and R. Peierls. Discussion of the paper by de Boer and Verwey. In *Proceedings of the Physical Society*, volume 72, 1937. URL: http://iopscience.iop.org/0959-5309/49/4S/308.

[136] B. Y. Mueller and B. Rethfeld. Relaxation dynamics in laser-excited metals under nonequilibrium conditions. *Physical Review B*, 87(3):035139, Jan.

2013. URL: http://link.aps.org/doi/10.1103/PhysRevB.87.035139, doi:10.1103/PhysRevB.87.035139.

[137] C. Nordling, E. Sokolowski, and K. Siegbahn. Precision method for obtaining absolute values of atomic binding energies. *Physical Review*, 105(5):1676, 1957. URL: http://journals.aps.org/pr/abstract/10.1103/PhysRev.105.1676.

[138] F. Novelli, G. De Filippis, V. Cataudella, M. Esposito, I. Vergara Kausel, F. Cilento, E. Sindici, A. Amaricci, C. Giannetti, D. Prabhakaran, S. Wall, A. Perucchi, S. Dal Conte, G. Cerullo, M. Capone, A. Mishchenko, M. Grüninger, N. Nagaosa, F. Parmigiani, and D. Fausti. Witnessing the formation and relaxation of massive quasi-particles in a strongly correlated electron system. *arXiv preprint arXiv: ...*, pages 1–17, 2014. URL: http://arxiv.org/abs/1403.1704.

[139] F. Novelli, D. Fausti, F. Giusti, F. Parmigiani, and M. Hoffmann. Mixed regime of light-matter interaction revealed by phase sensitive measurements of the dynamical Franz-Keldysh effect. *Scientific reports*, 3(2):1227, Jan. 2013. URL: http://www.pubmedcentral.nih.gov/articlerender.fcgi?artid=3565173&tool=pmcentrez&rendertype=abstract, doi:10.1038/srep01227.

[140] F. Novelli, D. Fausti, J. Reul, F. Cilento, P. H. M. van Loosdrecht, A. A. Nugroho, T. T. M. Palstra, M. Grüninger, and F. Parmigiani. Ultrafast optical spectroscopy of the lowest energy excitations in the Mott insulator compound YVO_3: Evidence for Hubbard-type excitons. *Physical Review B*, 86(16):165135, Oct. 2012. URL: http://link.aps.org/doi/10.1103/PhysRevB.86.165135, doi:10.1103/PhysRevB.86.165135.

[141] K. Okazaki, Y. Ito, Y. Ota, Y. Kotani, T. Shimojima, T. Kiss, S. Watanabe, C.-T. Chen, S. Niitaka, T. Hanaguri, H. Takagi, A. Chainani, and S. Shin. Superconductivity in an electron band just above the Fermi level: possible route to BCS-BEC superconductivity. *Scientific reports*, 4:4109, Jan. 2014. URL: http://www.pubmedcentral.nih.gov/articlerender.fcgi?artid=3937798&tool=pmcentrez&rendertype=abstract, doi:10.1038/srep04109.

[142] K. Okazaki, Y. Ota, Y. Kotani, W. Malaeb, Y. Ishida, T. Shimojima, T. Kiss, S. Watanabe, C.-T. Chen, K. Kihou, C. H. Lee, A. Iyo, H. Eisaki, T. Saito, H. Fukazawa, Y. Kohori, K. Hashimoto, T. Shibauchi, Y. Matsuda, H. Ikeda, H. Miyahara, R. Arita, A. Chainani, and S. Shin. Octet-line node structure of superconducting order parameter in KFe_2As_2. *Science (New York,*

N.Y.), 337(6100):1314–7, Sept. 2012. URL: http://www.ncbi.nlm.nih.gov/pubmed/22984065, doi:10.1126/science.1222793.

[143] J. Orenstein. Ultrafast spectroscopy of quantum materials. *Physics Today*, 65(9):44, 2012. URL: http://link.aip.org/link/PHTOAD/v65/i9/p44/s1&Agg=doi, doi:10.1063/PT.3.1717.

[144] E. Papalazarou, M. Gatti, M. Marsi, V. Brouet, F. Iori, L. Reining, E. Annese, I. Vobornik, F. Offi, A. Fondacaro, S. Huotari, P. Lacovig, O. Tjernberg, N. Brookes, M. Sacchi, P. Metcalf, and G. Panaccione. Valence-band electronic structure of V_2O_3: Identification of V and O bands. *Physical Review B*, 80(15):155115, Oct. 2009. URL: http://link.aps.org/doi/10.1103/PhysRevB.80.155115, doi:10.1103/PhysRevB.80.155115.

[145] J. Park, L. Tjeng, A. Tanaka, J. Allen, C. T. Chen, P. Metcalf, J. Honig, F. M. F. de Groot, and G. A. Sawatzky. Spin and orbital occupation and phase transitions in V_2O_3. *Physical Review B*, 61(17):11506, 2000. URL: http://prb.aps.org/abstract/PRB/v61/i17/p11506_1.

[146] L. Perfetti, P. Loukakos, M. Lisowski, U. Bovensiepen, H. Berger, S. Biermann, P. Cornaglia, A. Georges, and M. Wolf. Time Evolution of the Electronic Structure of 1T-TaS_2 through the Insulator-Metal Transition. *Physical Review Letters*, 97(6):1–4, Aug. 2006. URL: http://link.aps.org/doi/10.1103/PhysRevLett.97.067402, doi:10.1103/PhysRevLett.97.067402.

[147] L. Perfetti, P. A. Loukakos, M. Lisowski, U. Bovensiepen, H. Eisaki, and M. Wolf. Ultrafast Electron Relaxation in Superconducting $Bi_2Sr_2CaCu_2O_{8+\delta}$ by Time-Resolved Photoelectron Spectroscopy. *Physical Review Letters*, 99(19):197001, Nov. 2007. URL: http://link.aps.org/doi/10.1103/PhysRevLett.99.197001, doi:10.1103/PhysRevLett.99.197001.

[148] L. Piazza, D. Masiel, T. LaGrange, B. Reed, B. Barwick, and F. Carbone. Design and implementation of a fs-resolved transmission electron microscope based on thermionic gun technology. *Chemical Physics*, 423:79–84, Sept. 2013. URL: http://linkinghub.elsevier.com/retrieve/pii/S0301010413002826, doi:10.1016/j.chemphys.2013.06.026.

[149] A. Polkovnikov, K. Sengupta, A. Silva, and M. Vengalattore. Colloquium: Nonequilibrium dynamics of closed interacting quantum systems. *Reviews of Modern Physics*, 83(3):863–883, Aug. 2011. URL: http://link.aps.org/doi/10.1103/RevModPhys.83.863, doi:10.1103/RevModPhys.83.863.

[150] A. Poteryaev, J. Tomczak, S. Biermann, A. Georges, A. Lichtenstein, A. Rubtsov, T. Saha-Dasgupta, and O. Andersen. Enhanced crystal-field splitting and orbital-selective coherence induced by strong correlations in V_2O_3. *Physical Review B*, 76(8):085127, Aug. 2007. URL: http://link.aps.org/doi/10.1103/PhysRevB.76.085127, doi:10.1103/PhysRevB.76.085127.

[151] M. Qazilbash, M. Brehm, B.-G. Chae, P.-C. Ho, G. Andreev, B.-J. Kim, S. J. Yun, A. Balatsky, M. Maple, F. Keilmann, H.-T. Kim, and D. Basov. Mott transition in VO_2 revealed by infrared spectroscopy and nano-imaging. *Science (New York, N.Y.)*, 318(5857):1750–3, Dec. 2007. URL: http://www.ncbi.nlm.nih.gov/pubmed/18079396, doi:10.1126/science.1150124.

[152] J. D. Rameau, S. Freutel, L. Rettig, I. Avigo, M. Ligges, Y. Yoshida, H. Eisaki, J. Schneeloch, R. D. Zhong, Z. J. Xu, G. D. Gu, P. D. Johnson, and U. Bovensiepen. Photoinduced changes in the cuprate electronic structure revealed by femtosecond time- and angle-resolved photoemission. *Phys. Rev. B*, 89(11):115115, Mar. 2014. URL: http://link.aps.org/doi/10.1103/PhysRevB.89.115115, doi:10.1103/PhysRevB.89.115115.

[153] S. Ravy. *Structure de la matiére condensée*. Ed. U-psud, Orsay, 2011.

[154] M. Rini, R. Tobey, N. Dean, J. Itatani, Y. Tomioka, Y. Tokura, R. W. Schoenlein, and A. Cavalleri. Control of the electronic phase of a manganite by mode-selective vibrational excitation. *Nature*, 449(7158):72–4, Sept. 2007. URL: http://www.ncbi.nlm.nih.gov/pubmed/17805291, doi:10.1038/nature06119.

[155] W. R. ROBINSON. High-temperature crystal chemistry of V_2O_3 and 1% Chromium-doped V_2O_3. *Acta Crystallographica Section B*, 31:1153, 1975.

[156] F. Rodolakis, P. Hansmann, J.-P. Rueff, A. Toschi, M. W. Haverkort, G. Sangiovanni, A. Tanaka, T. Saha-Dasgupta, O. K. Andersen, K. Held, M. Sikora, I. Alliot, J.-P. Itié, F. Baudelet, P. Wzietek, P. Metcalf, and M. Marsi. Inequivalent Routes across the Mott Transition in V_2O_3 Explored by X-Ray Absorption. *Physical Review Letters*, 104(4):26–29, Jan. 2010. URL: http://link.aps.org/doi/10.1103/PhysRevLett.104.047401, doi:10.1103/PhysRevLett.104.047401.

[157] F. Rodolakis, B. Mansart, E. Papalazarou, S. Gorovikov, P. Vilmercati, L. Petaccia, A. Goldoni, J. Rueff, S. Lupi, P. Metcalf, and M. Marsi. Quasiparticles at the Mott Transition in V_2O_3: Wave Vector Dependence and Surface Attenuation. *Physical Review Letters*, 102(6):066805, Feb. 2009. URL:

http://link.aps.org/doi/10.1103/PhysRevLett.102.066805, doi:10.1103/PhysRevLett.102.066805.

[158] F. Rodolakis, J.-P. Rueff, M. Sikora, I. Alliot, J.-P. Itié, F. Baudelet, S. Ravy, P. Wzietek, P. Hansmann, A. Toschi, M. Haverkort, G. Sangiovanni, K. Held, P. Metcalf, and M. Marsi. Evolution of the electronic structure of a Mott system across its phase diagram: X-ray absorption spectroscopy study of $(V_{1-x}Cr_x)_2O_3$. *Physical Review B*, 84(24):1–10, Dec. 2011. URL: http://link.aps.org/doi/10.1103/PhysRevB.84.245113, doi:10.1103/PhysRevB.84.245113.

[159] T. Rohwer, S. Hellmann, M. Wiesenmayer, C. Sohrt, A. Stange, B. Slomski, A. Carr, Y. Liu, L. M. Avila, M. Kalläne, S. Mathias, L. Kipp, K. Rossnagel, and M. Bauer. Collapse of long-range charge order tracked by time-resolved photoemission at high momenta. *Nature*, 471(7339):490–3, Mar. 2011. URL: http://www.ncbi.nlm.nih.gov/pubmed/21389987, doi:10.1038/nature09829.

[160] A. Rousse, P. Audebert, J. P. Geindre, F. Fallies, J. C. Gauthier, A. Mysyrowicz, G. Grillon, and A. Antonetti. Efficient Kα x-ray source from femtosecond laser-produced plasmas. *Physical Review E*, 50(3):2200–2207, 1994. URL: http://journals.aps.org/pre/abstract/10.1103/PhysRevE.50.2200.

[161] A. Rousse, C. Rischel, and J.-c. Gauthier. Colloquium : Femtosecond x-ray crystallography. *Reviews of Modern Physics*, 73(1):17–31, 2001.

[162] E. Rowe and F. Mills. Tantalus I: a dedicated storage ring synchrotron radiation source. *Part. Accel.*, 4:211–227, 1973. URL: http://cds.cern.ch/record/1107919.

[163] M. Rozenberg, G. Kotliar, and H. Kajueter. Transfer of spectral weight in spectroscopies of correlated electron systems. *Physical review. B, Condensed matter*, 54(12):8452–8468, Sept. 1996. URL: http://www.ncbi.nlm.nih.gov/pubmed/9984518.

[164] M. Rozenberg, G. Kotliar, H. Kajueter, G. A. Thomas, J. Honig, and P. Metcalf. Optical conductivity in Mott-Hubbard systems. *Physical Review Letters*, 75(1):105–108, 1995. URL: http://link.aps.org/doi/10.1103/PhysRevLett.75.105http://journals.aps.org/prl/abstract/10.1103/PhysRevLett.75.105.

[165] M. Rozenberg, G. Kotliar, and X. Zhang. Mott-Hubbard transition in infinite dimensions. II. *Physical Review B*, 49(15):10181, 1994. URL: http://journals.aps.org/prb/abstract/10.1103/PhysRevB.49.10181.

[166] M. Rozenberg, X. Zhang, and G. Kotliar. Mott-Hubbard transition in infinite dimensions. *Physical review letters*, 69(8):1236–1239, 1992. URL: http://journals.aps.org/prl/abstract/10.1103/PhysRevLett.69.1236.

[167] T. Saha-Dasgupta, O. K. Andersen, J. Nuss, A. I. Poteryaev, A. Georges, and A. I. Lichtenstein. Electronic structure of V_2O_3: Wannier orbitals from LDA- NMTO calculations. *arXiv preprint arXiv: ...*, pages 1–22, 2009. URL: http://arxiv.org/abs/0907.2841, arXiv:arXiv:0907.2841v1.

[168] M. Sandri, M. Capone, and M. Fabrizio. Finite-temperature Gutzwiller approximation and the phase diagram of a toy model for V_2O_3. *Physical Review B*, 87(20):205108, 2013. URL: http://prb.aps.org/abstract/PRB/v87/i20/e205108, arXiv:arXiv:1302.4927v1.

[169] M. Sandri and M. Fabrizio. Non-equilibrium gap-collapse near a first-order Mott transition. *Arxiv preprint arXiv:*, pages 1–12, Oct. 2014. URL: http://arxiv.org/abs/1410.4442v1, arXiv:1410.4442.

[170] D. Santos-Cottin, G. Lantz, E. Papalazarou, M. Marsi, M. Casula, Y. Klein, and A. Gauzzi. ARPES study of the electronic structure of the correlated quasi-2D metal $BaNiS_2$. *(unpublished)*, 2014.

[171] H. Sasaki, H. Harashina, K. Kodama, M. Sato, S.-i. Shamoto, M. Nishi, and K. Kakurai. Neutron Scattering Study on Metal-Insulator Transitions of BaCoS 2 Induced by External Pressure and by Ni-Doping. *Journal of the Physical Society of Japan*, 67(12):4235–4242, 1998. URL: http://journals.jps.jp/doi/abs/10.1143/JPSJ.67.4235.

[172] T. Sato, H. Kumigashira, D. Ionel, T. Takahashi, I. Hase, H. Ding, J. Campuzano, and S. Shamoto. Evolution of metallic states from the Hubbard band in the two-dimensional Mott system $BaCo_{1-x}Ni_xS_2$. *Physical Review B*, 64(7):075103, July 2001. URL: http://link.aps.org/doi/10.1103/PhysRevB.64.075103, doi:10.1103/PhysRevB.64.075103.

[173] M. Schiró and M. Fabrizio. Time-Dependent Mean Field Theory for Quench Dynamics in Correlated Electron Systems. *Physical Review Letters*, 105(7):1–4, Aug. 2010. URL: http://link.aps.org/doi/10.1103/PhysRevLett.105.076401, doi:10.1103/PhysRevLett.105.076401.

[174] R. Schoenlein, W. Lin, J. Fujimoto, and G. Eesley. Femtosecond studies of nonequilibrium electronic processes in metals. *Physical Review Letters*, 58(16):1680–1683, 1987. URL: http://journals.aps.org/prl/abstract/10.1103/PhysRevLett.58.1680.

[175] R. W. Schoenlein, S. Chattopadhyay, H. H. W. Chong, T. E. Glover, P. A. Heimann, C. V. Shank, A. A. Zholents, and M. S. Zolotorev. Generation of Femtosecond Pulses of Synchrotron Radiation. *Science*, 287(5461):2237–2240, Mar. 2000. URL: http://www.sciencemag.org/cgi/doi/10.1126/science.287.5461.2237, doi:10.1126/science.287.5461.2237.

[176] R. W. Schoenlein, W. P. Leemans, A. H. Chin, P. Volfbeyn, T. E. Glover, P. Balling, M. Zolotorev, K.-J. Kim, S. Chattopadhyay, and C. V. Shank. Femtosecond X-ray Pulses at 0.4 $\mathring{A}$ Generated by 90° Thomson Scattering: A Tool for Probing the Structural Dynamics of Materials. *Science*, 274(5285):236–238, 1996. URL: http://www.sciencemag.org/content/274/5285/236.abstract, doi:10.1126/science.274.5285.236.

[177] M. Seah and W. Dench. quantitative electron spectroscopy of surfaces: a standard data base for electron inelastic mean free paths in solids. *Surface and Interface analysis*, 1(1):2–11, 1979. URL: http://onlinelibrary.wiley.com/doi/10.1002/sia.740010103/abstract.

[178] S. Shamoto, S. Tanaka, E. Ueda, and M. Sato. Single crystal growth of $BaNiS_2$. *Journal of crystal growth*, 154:197–201, 1995. URL: http://www.sciencedirect.com/science/article/pii/0022024895002251.

[179] C. L. Smallwood, J. P. Hinton, C. Jozwiak, W. Zhang, J. D. Koralek, H. Eisaki, D.-H. Lee, J. Orenstein, and a. Lanzara. Tracking Cooper Pairs in a Cuprate Superconductor by Ultrafast Angle-Resolved Photoemission. *Science*, 336(6085):1137–1139, May 2012. URL: http://www.sciencemag.org/cgi/doi/10.1126/science.1217423, doi:10.1126/science.1217423.

[180] E. Smith and V. E. Henrich. Photoemission study of composition- and temperature-induced metal-insulator transitions in Cr-doped V_2O_3. *Physical Review B*, 50(3):1382–1390, 1994.

[181] K. Smith and V. Henrich. Bulk band dispersion in Ti_2O_3 and V_2O_3. *Physical Review B*, 38(9):5965–5975, 1988. URL: http://journals.aps.org/prb/abstract/10.1103/PhysRevB.38.5965.

[182] P. Sondhauss and J. S. Wark. research papers Extension of the time-dependent dynamical diffraction theory to 'optical phonon '-type distortions

: application to diffraction from coherent acoustic and optical phonons research papers. *Acta Crystallographica Section A*, 59:7–13, 2003.

[183] L. Stojchevska, I. Vaskivskyi, T. Mertelj, P. Kusar, D. Svetin, S. Brazovskii, and D. Mihailovic. Ultrafast switching to a stable hidden quantum state in an electronic crystal. *Science (New York, N.Y.)*, 344(6180):177–80, Apr. 2014. URL: http://www.ncbi.nlm.nih.gov/pubmed/24723607, doi:10.1126/science.1241591.

[184] P. Stoliar, L. Cario, E. Janod, B. Corraze, C. Guillot-Deudon, S. Salmon-Bourmand, V. Guiot, J. Tranchant, and M. Rozenberg. Universal Electric-Field-Driven Resistive Transition in Narrow-Gap Mott Insulators. *Advanced materials*, 25(23):3222–3226, May 2013. URL: http://www.ncbi.nlm.nih.gov/pubmed/23649904, doi:10.1002/adma.201301113.

[185] P. Stoliar, M. Rozenberg, E. Janod, B. Corraze, J. Tranchant, and L. Cario. Nonthermal and purely electronic resistive switching in a Mott memory. *Physical Review B*, 90(4):045146, July 2014. URL: http://link.aps.org/doi/10.1103/PhysRevB.90.045146, doi:10.1103/PhysRevB.90.045146.

[186] C. Sun, F. Vallée, L. Acioli, E. Ippen, and J. Fujimoto. Femtosecond-tunable measurement of electron thermalization in gold. *Physical Review B*, 50(20):15337, 1994. URL: http://journals.aps.org/prb/abstract/10.1103/PhysRevB.50.15337.

[187] C. K. Sun, F. Vallee, L. Acioli, E. P. Ippen, and J. Fujimoto. Femtosecond investigation of electron thermalization in gold. *Physical Review B*, 48(16):12365–12368, 1993. URL: http://journals.aps.org/prb/abstract/10.1103/PhysRevB.48.12365.

[188] C. Tatsuyama and H. Fan. Raman scattering and phase transitions in V_2O_3 and $(V_{1-x}Cr_x)_2O_3$. *Physical Review B*, 21(7):2977, 1980. URL: http://prb.aps.org/abstract/PRB/v21/i7/p2977_1.

[189] J. M. Tomczak and S. Biermann. Multi-orbital effects in optical properties of vanadium sesquioxide. *Journal of physics. Condensed matter : an Institute of Physics journal*, 21(6):064209, Mar. 2009. URL: http://www.ncbi.nlm.nih.gov/pubmed/21715912, doi:10.1088/0953-8984/21/6/064209.

[190] J. M. Tomczak, M. Casula, T. Miyake, F. Aryasetiawan, and S. Biermann. Combined GW and dynamical mean-field theory: Dynamical screening effects in transition metal oxides. *EPL (Europhysics Letters)*, 100(6):67001, Dec. 2012. URL: http://stacks.iop.org/0295-5075/100/

i=6/a=67001?key=crossref.6924fb4a403bf2fbd800c92cb62524db, doi:10.1209/0295-5075/100/67001.

[191] M. Tordeux, J. Barros, A. Bence, P. Brunelle, N. Hubert, M. Labat, A. Nadji, L. Nadolski, and J. Pollina. Low alpha Operation for the Soleil Storage ring. In *Proceedings of IPAC2012*, pages 1608–1610, 2012.

[192] D. W. Turner and M. I. A. Jobory. Determination of Ionization Potentials by Photoelectron Energy Measurement. *The Journal of Chemical Physics*, 37(12), 1962.

[193] D. Vollhardt. Normal ^{3}He: an almost localized Fermi liquid. *Reviews of Modern Physics*, 56(1):99–120, 1984. URL: http://journals.aps.org/rmp/abstract/10.1103/RevModPhys.56.99.

[194] D. von der Linde, A. Laubereau, and W. Kaiser. Molecular vibration in liquids: Direct Measurement of the Molecular Daphasing Time; Determination of the Shape of Picosecond Light Pulses. *Physical review letters*, 26(16):954, 1971.

[195] S. Wall, D. Brida, S. R. Clark, H. P. Ehrke, D. Jaksch, A. Ardavan, S. Bonora, H. Uemura, Y. Takahashi, T. Hasegawa, H. Okamoto, G. Cerullo, and A. Cavalleri. Quantum interference between charge excitation paths in a solid-state Mott insulator. *Nature Physics*, 7(2):114–118, Dec. 2010. URL: http://www.nature.com/doifinder/10.1038/nphys1831, doi:10.1038/nphys1831.

[196] S. Wall, L. Foglia, D. Wegkamp, K. Appavoo, J. Nag, R. F. Haglund, J. Stähler, and M. Wolf. Tracking the evolution of electronic and structural properties of VO_2 during the ultrafast photoinduced insulator-metal transition. *Physical Review B*, 87(11):115126, Mar. 2013. URL: http://link.aps.org/doi/10.1103/PhysRevB.87.115126, doi:10.1103/PhysRevB.87.115126.

[197] S. Wall, D. Wegkamp, L. Foglia, K. Appavoo, J. Nag, R. F. Haglund, J. Stähler, and M. Wolf. Ultrafast changes in lattice symmetry probed by coherent phonons. *Nature communications*, 3:721, Jan. 2012. URL: http://www.ncbi.nlm.nih.gov/pubmed/22395612, doi:10.1038/ncomms1719.

[198] W.-S. Wang, X.-M. He, D. Wang, Q.-H. Wang, Z. D. Wang, and F. C. Zhang. Finite-temperature Gutzwiller projection for strongly correlated electron systems. *Physical Review B*, 82(12):125105, Sept. 2010. URL: http://link.aps.org/doi/10.1103/PhysRevB.82.125105, doi:10.1103/PhysRevB.82.125105.

[199] B. E. Warren. *X-ray diffraction*. Dover Publications, New York, 1990.

[200] D. Wegkamp, M. Herzog, L. Xian, M. Gatti, P. Cudazzo, C. L. McGahan, R. E. Marvel, R. F. Haglund, A. Rubio, M. Wolf, and J. Stähler. Instantaneous band gap collapse in photoexcited monoclinic VO_2 due to photocarrier doping. *Arxiv preprint arXiv:*, Aug. 2014. URL: http://arxiv.org/abs/1408.3209, arXiv:1408.3209.

[201] P. Werner, M. Casula, T. Miyake, F. Aryasetiawan, A. J. Millis, and S. Biermann. Satellites and large doping and temperature dependence of electronic properties in hole-doped $BaFe_2As_2$. *Nature Physics*, 8(4):331–337, Mar. 2012. URL: http://www.nature.com/doifinder/10.1038/nphys2250, doi:10.1038/nphys2250.

[202] P. Werner and M. Eckstein. Field-induced polaron formation in the Holstein-Hubbard model. *Arxiv preprint arXiv:*, pages 1–7, 2014. arXiv:arXiv:1403.7376v1.

[203] F. Wooten. *Optical properties of solids*. Academic Press, Inc., London, 1972. URL: http://scholar.google.com/scholar?hl=en&btnG=Search&q=intitle:Optical+properties+of+solids#0.

[204] A. Wu, X. Xu, and R. Venkatasubramanian. Ultrafast dynamics of photoexcited coherent phonon in Bi_2Te_3 thin films. *Applied Physics Letters*, 92(1):011108, 2008. URL: http://ieeexplore.ieee.org/xpls/abs_all.jsp?arnumber=4831429, doi:10.1063/1.2829604.

[205] H. Yan, D. Song, K. F. Mak, I. Chatzakis, J. Maultzsch, and T. F. Heinz. Time-resolved Raman spectroscopy of optical phonons in graphite: Phonon anharmonic coupling and anomalous stiffening. *Physical Review B*, 80(12):121403, Sept. 2009. URL: http://link.aps.org/doi/10.1103/PhysRevB.80.121403, doi:10.1103/PhysRevB.80.121403.

[206] Y. Yan, E. B. Gamble, and K. A. Nelson. Impulsive stimulated scattering: General importance in femtosecond laser pulse interactions with matter, and spectroscopic applications. *The Journal of Chemical Physics*, 83(11), 1985.

[207] Y. Yasui, H. Sasaki, M. Sato, M. Ohashi, Y. Sekine, C. Murayama, and N. Mori. Studies of Pressure-Induced Mott Metal-Insulator Transition of $BaCoS_2$. *Journal of the Physical Society of Japan*, 68(4):1313–1320, 1999. URL: http://journals.jps.jp/doi/abs/10.1143/JPSJ.68.1313.

[208] R. Yen, J. M. Liu, N. Bloembergen, T. K. Yee, J. G. Fujimoto, and M. M. Salour. Picosecond laser interaction with metallic zirconium. *Applied Physics Letters*, 40(2), 1982.

[209] M. Yethiraj, S. Werner, W. Yelon, and J. Honig. Phonon anomalies and the magnetic transition in pure and Cr-doped V_2O_3. *Physical Review B*, 36(16):8675, 1987. URL: http://prb.aps.org/abstract/PRB/v36/i16/p8675_1.

[210] Z. P. Yin, A. Kutepov, and G. Kotliar. Correlation-Enhanced Electron-Phonon Coupling: Applications of GW and Screened Hybrid Functional to Bismuthates, Chloronitrides, and Other High-T_c Superconductors. *Physical Review X*, 3(2):021011, May 2013. URL: http://link.aps.org/doi/10.1103/PhysRevX.3.021011, doi:10.1103/PhysRevX.3.021011.

[211] R. Yoshida, T. Yamamoto, Y. Ishida, H. Nagao, T. Otsuka, K. Saeki, Y. Muraoka, R. Eguchi, K. Ishizaka, T. Kiss, S. Watanabe, T. Kanai, J. Itatani, and S. Shin. Ultrafast photoinduced transition of an insulating VO_2 thin film into a nonrutile metallic state. *Physical Review B*, 89(20):205114, May 2014. URL: http://link.aps.org/doi/10.1103/PhysRevB.89.205114, doi:10.1103/PhysRevB.89.205114.

[212] J. Zaanen, G. Sawatzky, and J. Allen. Band gaps and electronic structure of transition-metal compounds. *Physical Review Letters*, 55(4):418, 1985. URL: http://journals.aps.org/prl/abstract/10.1103/PhysRevLett.55.418.

[213] V. M. Zainullina, N. A. Skorikov, and M. A. Korotin. Description of the pressure-induced insulator-metal transition in $BaCoS_2$ within the LDA + DMFT approach. *Physics of the Solid State*, 54(9):1864–1869, Sept. 2012. URL: http://link.springer.com/10.1134/S1063783412090314, doi:10.1134/S1063783412090314.

[214] H. Zeiger, J. Vidal, T. Cheng, and E. Ippen. Theory for displacive excitation of coherent phonons. *Physical Review B*, 45(2):768, 1992. URL: http://journals.aps.org/prb/abstract/10.1103/PhysRevB.45.768.

[215] A. Zenesini, H. Lignier, D. Ciampini, O. Morsch, and E. Arimondo. Coherent Control of Dressed Matter Waves. *Physical Review Letters*, 102(10):100403, Mar. 2009. URL: http://link.aps.org/doi/10.1103/PhysRevLett.102.100403, doi:10.1103/PhysRevLett.102.100403.

[216] W. Zhang, C. L. Smallwood, C. Jozwiak, T. L. Miller, Y. Yoshida, H. Eisaki, D.-H. Lee, and A. Lanzara. Signatures of superconductivity and pseudogap formation in nonequilibrium nodal quasiparticles revealed by ultrafast angle-resolved photoemission. *Physical Review B*, 88(24):245132, Dec. 2013. URL: http://link.aps.org/doi/10.1103/PhysRevB.88.245132, doi:10.1103/PhysRevB.88.245132.